UNIVERSIDADE DE LISBOA
FACULDADE DE CIÊNCIAS
DEPARTAMENTO DE FÍSICA

Development of an image processing pipeline for the study of cortical lesions in multiple sclerosis patients using ultra-high field MRI

Marta Filipa Mateus Marques

Mestrado Integrado em Engenharia Biomédica e Biofísica

Perfil em Biofísica Médica e Fisiologia de Sistemas

Dissertação orientada por:

Prof. Dr. Alexandre Andrade

Prof. Dr. Hartwig Siebner

2019

We have not succeeded in answering all our problems. Indeed, we sometimes feel we have not completely answered any of them. The answers we have found only serve to raise a whole set of new questions. In some ways we feel we are as confused as ever, but we believe we are confused on a higher level and about more important things.

Earl C. Kelley
The Workshop Way of Learning (1951)

Acknowledgements

There is only so much gratitude that can be put into words. Sometimes language is not enough. Still, here is my attempt at expressing my gratitude towards all of you who impacted, in one way or another, the outcome of this project and this piece of work.

To Hartwig, thank you for your prompt response and willingness to receive me in the respectable institution that is the Danish Research Centre for Magnetic Resonance (DRCMR) from the first exchange of emails. It was the one push I needed to realize that Copenhagen could only be a good option. Thank you for the support throughout my internship.

To Mads, thank you for welcoming me into your project with open arms and for treating me as an equal since the very beginning. For seeing the value in my work and trusting my decisions. It has been a pleasure to be a part of the CLiMS project and I could not be more excited for the possibility to continue making research with you.

To Henrik, the guidance and support you were able to provide me with during the entirety of my project was the reason why I did not get stuck indefinitely in dead ends and always managed to find other routes and possibilities to explore. Thank you.

To the students at DRCMR with whom I got to share the "Beverly Hills" office with: Felix, Julie, Albert, Maud, Laura and Shahab, thank you for the conversations over lunch, for the table soccer games and for all the good moments and laughs. Mostly, thank you for your friendship and silliness.

To Julie, even if our relationship started at DRCMR I am happy to say that it has grown beyond it. You have become a friend and a mentor. Thank you for welcoming me into your life and for bringing such positivity into mine with your kindness and quirky nature.

To Louis, for sharing the same language of music, fascination for the brain and interest in well written and spoken communication. I found in you someone intelligent yet humble, eager to learn yet patient and whose ability to listen and curiosity to ask questions and wonder still dazzles me today. Thank you for your involvement in this project. And mostly, thank you for your time.

To Mariana, I am so glad we reconnected, years later, in the city of Vikings. It has been a pleasure to share this chapter of my life with you. Thank you for your friendship and loyalty and for giving me a reason to keep practicing Portuguese while teaching me bits of Danish along the way.

I would also like to express my gratitude towards the Erasmus+ institution, as well as the group at DRCMR, for the support throughout my stay in Copenhagen.

A dissertation reflects not only the work carried out during the course of the internship and the experiences that surround it, but the sum of all moments, battles and lessons lived by those who devote themselves to the art of learning. That being said, a thank you is also in order to those elements that have been pivotal in the past five years, if not eighteen, of my student journey.

To my teacher Alexandre Andrade, thank you for showing immediate interest in supporting this project and for guiding me throughout it from afar. But most importantly, thank you for helping me see the value in the work of a biomedical engineer by comparing its role to that of someone who works on the backstage of a play, not as exposed, but just as important to its overall success. This beautiful analogy

delivered during one of my first lectures at the Faculty of Sciences of the University of Lisbon (FCUL) has followed me ever since, guiding me in periods of confusion and uncertainty.

To the academical group at FCUL and at the Institute of Biomedical Engineering and Biophysics (IBEB), thank you for the sharing of knowledge during these past five years. Moreover, thank you for teaching me the importance of hard work and resilience, not only in class, but in life.

To Catarina and André, I still remember the first day I met you on that corridor of Pavilion C8 as though it was only yesterday. It was a pleasure sharing all those study sessions, project presentations, lab hours and leisure moments in Lisbon and London with you. You became, without a doubt, my favorite part about FCUL. I look forward to continuing sharing my time with you now outside of it.

To Mónica, my buddy. Every moment and exchange of words with you is worth any period of absence. You make every moment better and continue to inspire me with your vulnerable strength and unapologetic grace.

To Teresa, the one friend who always keeps me grounded. I am so grateful you found me on that little corner of the internet a decade ago and that we got to grow up side by side ever since then.

To Pedro, the best guitar teacher I know, and to Sara and Mafalda, my guitar peers, playing with you all at the end of every week was the best way to escape my mind and leave behind all my worries. I still cannot fathom a better Friday evening plan than to play music with friends. Nothing seems to compare.

To my grandmother, the person who gets me far beyond words but who will not get this if it is not written in her mother tongue. O universo por desvendar não se compara ao carinho, respeito e admiração que tenho por ti. Obrigado por me teres ensinado a amar, a acreditar e a ser. O meu mundo é mais colorido por tu fazeres parte dele.

Finally, to my parents and brother, thank you for accepting me and loving me no matter what. For supporting my dreams and for giving me the time and space to learn and grow, even if away from home. I am so lucky.

Resumo

A esclerose múltipla é uma doença crónica e inflamatória do sistema nervoso central de alta prevalência nos dias de hoje. Durante anos, o foco da doença foi a patologia visível na matéria branca. Apesar dos primeiros estudos de patologia cortical em esclerose múltipla apontarem para a década de 60, foi apenas no início do novo século que o córtex passou a ser estudado como parte integral da doença. Desde então, estudos têm vindo a demonstrar que o comprometimento do córtex parece estar relacionado com danos cognitivos e físicos, frequentemente associados à doença. A necessidade de melhor compreender o impacto das lesões corticais no desenvolvimento da doença e na vida diária destes pacientes tem motivado o seu estudo, sendo a Ressonância Magnética (RM), em particular *scanners* de campo ultra-alto, a melhor ferramenta para as detetar e estudar.

A melhoria da razão sinal-ruído e da resolução espacial dos *scanners* de RM de campo ultra-alto tem permitido o aumento da deteção de lesões corticais. Ainda assim, a sua sensibilidade continua a não ser ideal e a estar fortemente dependente do tipo de lesão cortical, do contraste de RM usado na sua deteção e da existência de ferramentas robustas que permitam a sua deteção de modo automático, mais eficiente e com menor espaço para erro. A falta de marcadores de imagem para a remielinização ou desmielinização parcial, tal como a ausência de diretrizes para a deteção destas lesões com campos de 7 (T)esla parece explicar a dificuldade em distinguir e identificar falsos positivos e as diferenças encontradas nas deteções realizadas por diferentes avaliadores.

Uma desvantagem dos *scanners* de campo ultra-alto é o maior efeito de *bias* que, caso não seja removido aquando da aquisição de imagens, terá de ser removido na fase de processamento por *softwares* e algoritmos que não estão originalmente construídos para trabalhar com imagens de maior resolução e cuja prestação não está ainda bem explorada nestas condições. Estes desafios comprometem o potencial dos *scanners* de RM de campo ultra-alto para o estudo das lesões corticais na esclerose múltipla.

Este projeto procura desenvolver uma *pipeline* semiautomática para o pré-processamento e processamento de imagens de RM de cariz estrutural de doentes com esclerose múltipla obtidas num *scanner* de campo ultra-alto. A *pipeline* é criada de modo gradual, recorrendo a análises visuais, ou de outro tipo, para confirmar a qualidade de cada passo antes de avançar para o seguinte, no pressuposto de que a qualidade dos *softwares* de imagem comercialmente disponíveis será menor ao utilizar imagens de maior resolução. A ocorrência de lesões corticais no córtex sensório-motor (SM1) é igualmente determinada e usada para validar a qualidade da *pipeline*.

Doze doentes com esclerose múltipla na sua forma recidivante-remitente ou secundariamente progressiva e seis controlos foram incluídos neste projeto. Todas as permissões necessárias do comité local de ética, proteção de dados e da *Danish Medicines Agency* foram previamente obtidas. Os doentes foram estudados num *scanner* de RM de corpo inteiro da Philips, *Achieva* 7,0 T, dedicado a investigação. Os participantes foram observados usando quatro tipos distintos de contraste: *magnetization prepared rapid acquisition by gradient echo* (MPRAGE) a três dimensões (3D) com 0,65-mm de resolução isotrópica, 3D *fluid attenuated inversion recovery* (FLAIR) com 0,7-mm de resolução isotrópica, 3D T1-*weighted* (T1w) de resolução 0,85x0,85x1,0 mm^3 e 3D T2-*weighted Turbo Spin Echo* (T2w-TSE) de 0,4-mm de resolução isotrópica.

A vertente de pré-processamento da *pipeline* incluiu uma correção de *bias* e o co-registo de imagens. Para a correção de *bias*, o *software* SPM foi testado utilizando os parâmetros habituais e uma alteração dos parâmetros relativos à *smoothness* e regularização, como sugerido na literatura. O processo de co-registo seguiu o procedimento utilizado no processamento de imagens de doentes com esclerose múltipla de 3 T no Danish Research Centre for Magnetic Resonance (DRCMR), com alterações posteriormente adicionadas para melhorar a qualidade do alinhamento das imagens de cada indivíduo a 7 T. Após o pré-processamento, uma deteção de lesões corticais, seguida da sua segmentação, foi realizada manualmente utilizando as ferramentas do *software* FSL. A vertente de processamento da *pipeline* incluiu uma segmentação do cérebro, um registo das imagens dos doentes e a criação de superfícies corticais. A segmentação foi testada utilizando três diferentes ferramentas: o *software* SPM, uma *toolbox* do SPM, CAT, e a ferramenta de segmentação do FSL, FAST. A *toolbox* do SPM, DARTEL, foi usada no registo de imagens e o *software* FreeSurfer permitiu a criação de superfícies individuais e de grupo no último passo da *pipeline*. As máscaras com as lesões criadas após a segmentação manual de lesões seguiram um caminho semelhante de processamento de modo a permitir a sua correta sobreposição no respetivo volume, e, posteriormente, superfície, e a possibilidade de fazer análises individuais ou de grupo.

Os resultados obtidos mostraram que os *softwares* para processamento de imagens de RM disponíveis apresentam, em geral, uma boa prestação e fornecem resultados de confiança. Ainda assim, a sua prestação pode ser otimizada incluindo procedimentos adicionais em cada passo ou por alteração das configurações originais dos *softwares*. A diminuição do parâmetro de largura à meia altura com um aumento do parâmetro de regularização na correção de *bias* com o SPM permitiu a criação de campos de *bias* mais fieis às imagens originais, consequentemente melhorando a sua correção e a diferenciação da matéria branca e matéria cinzenta nas imagens resultantes. A criação adicional de máscaras contendo apenas o cérebro e a utilização exclusiva de transformações de corpo rígido no co-registo de imagens permitiu a utilização de vários contrastes na tarefa de deteção de lesões, sem interferir com a sua localização ou morfologia. Na segmentação, a *toolbox* do SPM, CAT, mostrou melhorias na capacidade de separar as diferentes classes de tecidos com maior confiança e qualidade, particularmente nas regiões de contacto entre a matéria branca e cinzenta. Consequentemente, a qualidade do alinhamento das imagens dos diferentes doentes e a posterior criação de uma imagem média a partir de imagens individuais foi melhorada. O sucesso da *pipeline* permitiu a sobreposição das lesões corticais manualmente segmentadas nas superfícies individuais e/ou comuns criadas, onde foi descoberto que a maioria das lesões ocorreu no hemisfério direito, com sobreposições de lesões respetivas a diferentes doentes a ocorrer maioritariamente nos sulcos corticais, comparativamente aos giros. Porém, a segmentação de lesões demonstrou ser dispendiosa, dependente do avaliador e altamente influenciada por fatores inerentes ao avaliador, tal como o cansaço, nível de concentração ou de aborrecimento, e fatores externos, no qual se destacam a luminosidade do computador ou a luminosidade da sala onde a deteção foi feita. A *feature* do FreeSurfer para imagens de maior resolução não se mostrou fiável no tratamento dos dados de resolução isotrópica de 0,5-mm deste projeto, uma possível razão pela qual ainda se encontra em desenvolvimento.

Apesar dos bons resultados obtidos, investigação adicional será necessária para melhor compreender a prestação destes e de outros *softwares* para imagem médica no processamento de imagens de RM de maior resolução, tal como a melhor maneira de tirar partido dos mesmos em estudos clínicos a 7 T. A extensão da *pipeline* a outros doentes com esclerose múltipla irá aumentar a amostra em estudo e permitir um estudo mais extensivo da patologia cortical e a compreensão do impacto de uma ou mais lesões localizadas na região SM1 na conectividade e integridade funcional da região cortical afetada.

Palavras-chave: RM de campo ultra-alto, esclerose múltipla, lesões corticais, processamento de imagem, *pipeline* semiautomática.

Abstract

The importance of grey matter pathology to the understanding of multiple sclerosis has been acknowledged. However, the sensitivity to cortical lesions is limited when using conventional magnetic resonance imaging (MRI) systems. Ultra-high field (UHF) MRI systems have improved detection sensitivity but impose the additional challenge of a higher effect of bias to account for. Currently, image processing tools are not designed for higher resolution data and the performance of common software packages under these conditions has not been properly explored. These challenges have impaired the potential of UHF-MRI to study cortical lesions in multiple sclerosis.

This project aims at developing a semi-automated pipeline for the pre-processing and processing of structural UHF-MRI data of multiple sclerosis patients. The pipeline is built in a step-by-step fashion, making use of visual assessments and other analyses to confirm the quality of each step before advancing to the next, under the assumption that the performance of common imaging software packages will be poorer when using higher resolution data. The occurrence of cortical lesions within the primary sensory-motor cortex (SM1) is also determined and used to validate the quality of the pipeline.

Twelve patients with relapsing-remitting multiple sclerosis or secondary progressive multiple sclerosis and six healthy age-matched controls were included in this project. All relevant permissions from the local ethics committee and data protection had been obtained beforehand. All participants were studied with whole-brain ultra-high field MRI at 7 Tesla (T), using a research-only 7 T Achieva MR system. The participants were scanned using four different MRI modalities, namely 3-dimensional (3D) magnetization prepared rapid acquisition by gradient echo (MPRAGE) at 0.65-mm isotropic resolution, 3D fluid attenuated inversion recovery (FLAIR) at 0.7-mm isotropic resolution, 3D T1-weighted (T1w) of 0.85x0.85x1.0 mm^3 reconstructed resolution and 3D T2-weighted Turbo Spin Echo (T2w-TSE) at 0.4-mm isotropic reconstructed resolution.

The pre-processing pipeline included a bias correction and a coregistration step. For the bias correction, SPM was tested using its default parameters and an alternative configuration that altered the smoothness and regularization parameters. The coregistration followed an approach used in the processing of multiple sclerosis data at 3 T, with changes added to improve the quality of the within-subject alignment at 7 T. After the data pre-processing, manual detection and segmentation of cortical lesions was performed using FSLeyes. The processing pipeline included brain segmentation, subject registration and cortical surface creation. Brain segmentation was tested with SPM, with SPM's toolbox, CAT, and with FSL's segmentation tool, FAST. SPM's DARTEL tool was used for subject registration and FreeSurfer allowed the creation of individual and an average cortical surface. The lesion masks created after the manual segmentation task followed a similar processing route to allow their overlay on the respective brain volumes and, posteriorly, surfaces, and the possibility of individual and group analyses.

Results showed that the currently available MRI image processing tools present overall good performance and reliability in the processing of higher resolution data of multiple sclerosis patients. Still, the quality of the outcomes can be optimized by including additional steps or changes to the original software configurations. Modifying SPM's smoothness and regularization parameters for the estimation of bias minimized its effect in the data, allowing a better differentiation between grey matter

and white matter. Removing the skull whilst keeping the coregistration to rigid body transformations allowed the use of several contrasts in the lesion detection task without interfering with the lesions' morphology and topography. Brain segmentation using CAT showed more stability across the dataset, improving the quality of the subsequent subject registration and consequently of the average brain created. The success of the pipeline led to the possibility of overlaying the manually segmented lesions on the individual and group surfaces where it was found that the majority of lesions occurred on the right hemisphere and that lesion overlaps were more common in cortical sulci.

Despite the results obtained, further research is needed to understand the performance of other software packages in the processing of higher resolution MRI data and how to fully exploit these tools in the study of clinical data at 7 T.

Keywords: ultra-high field MRI, multiple sclerosis, cortical lesions, image processing, semi-automated pipeline.

Table of Contents

List of Figures

List of Tables

List of Abbreviations

BET	Brain Extraction Tool
CAT	Computational Anatomy Toolbox
CLIMS	Cortical Lesions in Multiple Sclerosis
CNR	Contrast-to-Noise Ratio
CNS	Central Nervous System
CSF	Cerebrospinal Fluid
CV	Coefficient of Variation
DARTEL	Diffeomorphic Anatomical Registration Through Exponentiated Lie Algebra
DIS	Dissemination in Space
DIT	Dissemination in Time
DRCMR	Danish Research Centre for Magnetic Resonance
EDSS	Expanded Disability Status Scale
FAST	FMRIB's Automated Segmentation Tool
FID	Free Induction Decay
FLAIR	Fluid Attenuated Inversion Recovery
fMRI	Functional Magnetic Resonance Imaging
FSL	FMRIB Software Library
FWHM	Full Width at Half Maximum
GM	Grey Matter
GRE	Gradient Echo
GUI	Graphical User Interface
IR	Inversion Recovery
MATLAB	Matrix Laboratory
MNI	Montreal Neurological Institute
MPRAGE	Magnetization Prepared Rapid Acquisition by Gradient Echo
MP2RAGE	Magnetization Prepared 2 Rapid Acquisition Gradient Echoes
MRI	Magnetic Resonance Imaging
MS	Multiple Sclerosis
PPMS	Primary Progressive Multiple Sclerosis
RF	Radio Frequency
RRMS	Relapsing–Remitting Multiple Sclerosis
SE	Spin Echo
SM1	Primary Sensory-Motor Cortex
SNS	Signal-to-Noise Ratio
SPM	Statistical Parametric Mapping
SPMS	Secondary Progressive Multiple Sclerosis
T	Tesla
TE	Time of Echo
TI	Time of Inversion
TR	Time of Repetition
TSE	Turbo Spin Echo
T1w	T1-weighted
T2w	T2-weighted
UHF	Ultra-High Field
WM	White Matter
3D	Three-Dimensional

1 Introduction

The brain remains one of the biggest puzzles to solve of our time. The knowledge that we currently possess of the healthy brain enables us to better understand what goes wrong in case of disease. Likewise, a focus on brain-related diseases can ultimately serve as a way to validate our knowledge of the brain and help disentangle some of our preconceived ideas about this organ.

Multiple sclerosis (MS) is an autoimmune, demyelinating disease of the central nervous system of high prevalence today. For years, white matter pathology was the hallmark of the disease [1]. Despite the initial research on cortical pathology dating from the 1960s, it was only decades later, with advances in imaging techniques, animal model studies and immunohistochemical analysis, that the study of the disease expanded into the cortex [2]. Since then, studies have demonstrated that cortical grey matter involvement can contribute to cognitive and physical disability, motivating the need to understand the impact of cortical lesions in the disease and everyday life of the patients [3]. The biggest advance towards improving the detection and visualization of cortical lesions has been to shift towards ultra-high field magnetic resonance imaging (UHF-MRI) systems [4].

As a result of the better signal-to-noise ratio and improved spatial resolution of UHF scanners, it is now possible to detect a higher number of cortical lesions as well as to better distinguish the different types of lesions present in this pathology [4], [5]. Even then, the sensitivity to cortical pathology remains nonideal. Some of the factors that seem to influence cortical lesion sensitivity include lesion type and the MRI modality used for the study of these lesions [6]. Lack of imaging markers for remyelination and partial demyelination and lack of cortical lesion detection guidelines at 7 T could explain interrater reliability and the difficulty in identifying false positives [6],[7],[8]. The development of robust automatic tools for cortical lesion detection should decrease the likelihood of human error in the detection of these lesions and significantly optimize the time-efficiency of this process.

Dealing with UHF scanners imposes extra challenges. For instance, there is a higher effect of bias in the acquired images. If not properly corrected, that bias could lessen the accuracy of certain imaging processing methods, particularly the brain segmentation [5]. Another challenge is related to the common image processing tools available which, albeit crucial for the processing of the original data acquired in the scanner, are not designed to work with higher-resolution UHF data [9]. These challenges have impaired the potential of UHF-MRI to study cortical lesions in multiple sclerosis.

The impact of single cortical lesions on the connectivity and functional integrity of the affected cortical area is yet to be understood. To account for this, a PhD project was designed at the Danish Research Centre for Magnetic Resonance (DRCMR) to explore the occurrence of cortical lesions within the primary sensory-motor cortex (SM1) and to clarify their impact on the sensorimotor network with regards to local and remote effects on brain function. Making use of the increased sensitivity of UHF MRI to detect cortical lesions, the PhD project, referred to as Cortical Lesions in Multiple Sclerosis (CLiMS), aims to assess the number, size and regional distribution of cortical lesions in SM1 with 7 T MRI and to relate regional lesion load in SM1 to MRI-based, electrophysiological, and behavioral correlates of hand function along with multimodal MRI-based metrics of structural and functional connectivity within the sensorimotor network. In order to fulfill the objectives of the overall PhD, this Master's project was set.

This project aims at developing a semi-automated pipeline for the pre-processing and processing of structural UHF-MRI data of multiple sclerosis patients. To accomplish its aim, the pipeline structure is initially thought-out and afterwards built in a step-by-step fashion, considering the outcomes of the current step to confirm its quality before advancing to the next. This is done under the assumption that the performance of common imaging software packages will be poorer when using higher resolution data.

Bias correction and coregistration are the first steps envisioned and incorporated into the pipeline and correspond to the pre-processing part of the pipeline. Afterwards, a brain segmentation, a subject registration and a surface creation step are incorporated as the processing part of the pipeline. Cortical lesions are identified and manually segmented as a supplementary task inherent to this project. Visual analyses are performed at each pipeline step and used as the main form of assessment of the results. Analyses of qualitative and/or quantitative nature are additionally performed to help confirm or discard the outcomes of the current step before advancing to the next. The occurrence of cortical lesions within the SM1 region is also determined and used to validate the quality of the pipeline.

The image processing pipeline should lead to the acquisition of an average and individual brain surfaces from the patients' data where the cortical lesions manually segmented can then be overlaid. A successful surface should allow a proper visualization of the distribution of cortical lesions in the SM1 area for this project's dataset and the possibility of extending the pipeline to the remaining subjects of the CLiMS project, contributing to its progress. The approach adopted for each step and the analyses made are influenced by the time available and by the accessible knowledge from literature or from advice from other researchers at the DRCMR.

The research described in this dissertation was carried out at DRCMR between October 2018 and July 2019. Besides the processing of structural MRI data and the development of an image processing pipeline for its study, the two main points extensively described in this dissertation, there was involvement in the acquisition of all structural data analyzed. Assistance in the acquisition of electrophysiological data using Electroencephalography and Transcranial Magnetic Stimulation for the PhD project was also provided during the entirety of this project. These additional tasks enabled a closer contact with multiple sclerosis patients, central to experience at first hand the manifestation of the disease and the different ways it can be expressed. The work developed was supervised by Head of Research Hartwig R. Siebner (DRCMR) and Assistant Professor Alexandre Andrade (FCUL) and co-supervised by Senior Researcher Henrik Lundell (DRCMR) and PhD Student Mads Madsen (DRCMR).

This dissertation is divided in six chapters. **Chapter 1** contains a brief overview of the work developed at DRCMR over the course of ten months and states the aims and general approach of this project. **Chapter 2** describes in detail the current knowledge of MS, particularly of cortical pathology, the principles of MRI, as well as an overview of UHF-MRI, image contrast in MRI and MRI image processing. Lastly, a section is created to highlight the significance of MRI in the study of MS, specifically of cortical lesions, over the years. **Chapter 3** corresponds to the project methodology and outlines the different steps of the pipeline and the approach followed in their design. **Chapter 4** displays the results of this project which are further analyzed and discussed in **Chapter 5**. **Chapter 6** contains some final remarks, the outcomes of this Master's project and a note on future work.

2 Background

In this chapter, the theoretical framework of this dissertation is provided. Firstly, in **Section 2.1**, the current knowledge of multiple sclerosis, particularly of cortical pathology, is given. Then, in **Section 2.2**, the principles of Magnetic Resonance Imaging (MRI), as well as an overview of ultra-high field MRI, image contrast in MRI and MRI image processing, are described. Lastly, **Section 2.3** highlights the significance of MRI in the study and diagnosis of multiple sclerosis, as well as its role in the assessment of cortical lesions.

2.1 Multiple Sclerosis

2.1.1 Overview of Multiple Sclerosis

Multiple sclerosis (MS) is considered the most prevalent chronic inflammatory disease of the central nervous system (CNS), affecting more than 2 million people around the world. It predominately affects individuals in their early adult life and is more common amongst females [10],[11].

It remains unknown whether MS has a single, or various, causes. Still, multiple genetic and environmental risk factors have been appointed as prompters of the disease. Amongst the environmental risk factors are a deficiency in vitamin D, diet and obesity in early life and cigarette smoking. Infectious agents can also play a role in the disease. The evidence of genetics in the development of MS is related to the HLA region of chromosome 6, implicated in the development of several autoimmune diseases. Carriers of the HLA DRB1*15:01 allele appear three times more likely to develop MS than non-carriers [12],[13].

The immune system plays a key role in the disease, particularly the adaptive immune system. Inflammation, which only occurs in the CNS, seems to be initiated by either a primary activation by extrinsic antigens, where pathogens are processed in peripheral tissues by dendritic cells, or by a primary activation by intrinsic antigens, where a release of antigens occurs in the CNS due to oligodendrocyte death. In summary, one event would be caused by an adaptive immune response, whilst the other would be a result of an intrinsic disturbance in the homeostasis of the CNS that also triggers an adaptive immune response. These responses give rise to an immune reaction in the lymphoid tissue and to a consequent invasion of lymphocytes, which include T cells and B cells, into the CNS. This results in lesions that appear throughout the CNS [14].

Multiple sclerosis lesions correspond to areas of demyelination, astrocytic gliosis and axonal or neuronal loss, often referred to as neurodegeneration. Similar to the disease that expresses heterogeneity in its clinical course and response to therapy, the neuroradiological appearance of white matter (WM) lesions across subjects is also known to be heterogeneous, evolving over the course of months and suggesting a single immune-effector mechanism that dominates in each individual. Due to this heterogeneity, the identification of noninvasive biomarkers associated with lesion patterns will aid in the design of personalized therapies [11],[15].

Demyelination is also present in grey matter (GM) with half of the lesions found to be of perivascular nature. When the inflamed vessel is located near the leukocortical junction, the

demyelination also affects the juxtacortical WM. Lesions can also project radially from microvessels. The remaining cortical lesions arise intracortically from the pial surface, often affecting several adjacent gyri [11],[16],[17].

The spinal cord and optic nerve can also be targeted in MS. In the spinal cord, atrophy is a result of focal inflammatory demyelination and neuroaxonal degeneration. Retinal damage found in the optic nerve is expressed by substantial thinning of the retinal nerve-fiber and ganglion-cell layers. This thinning is a consequence of tissue atrophy as well as neuronal and axonal loss. These neuropathological events can be studied in vivo using conventional and advanced imaging techniques [11],[18],[19].

MS lesions tend to result in symptoms of motor, sensory, cognitive or neuropsychiatric nature. The three most common and disabling motor symptoms in MS include spasticity, tremor, and gait impairment [20]. Changes in motor neuron excitability, presynaptic blocks, or a reduction in voluntary effort, may explain muscle weakness as well as the frequent sense of fatigue showed by these patients [21]. Sensory symptoms are often associated with numbness, paresthesias or changes in response to pain or temperature [22].

Cognitive impairment is also common in MS and has high prevalence rates at both early and late stages of the disease. The most commonly affected cognitive functions are attention, information processing efficiency and speed, as well as long-term memory [23]. Neuropsychiatric symptoms can also manifest in the disease and include personality changes, depression or bipolar disorder, affective disturbances, euphoria and suicidal ideation. Such symptoms are most commonly found in patients in advanced stages of the disease [21].

Even though the course of the disease can be unpredictable, individual cases have frequently been characterized as either chronic-progressive or relapsing/remitting. In the first, a gradual and steady deterioration is expected, while the second follows a stepwise degenerative path of exacerbations interspersed with periods of stability or even slight improvements [21].

About 85% of patients start by showing a recurrent and reversible course of the disease. This phase is termed relapsing–remitting multiple sclerosis (RRMS) and is associated with focal areas of inflammatory demyelination in which myelin, myelin-forming cells and axons are destroyed. The resolution of the inflammation and edema, as well as remyelination, contribute to the recovery or remission of these patients. This can also be achieved with corticosteroids, yet, the efficacy of corticosteroids in speeding up recovery after relapses will decrease over time. This stage of the disease can last for years or decades, with relapse rates varying from patient to patient [24],[25]. **Figure 2.1a** schematically depicts the relapsing–remitting course of the disease.

The majority of patients presenting RRMS are expected to enter a second phase associated with continuous, irreversible neurological changes unrelated to relapses. We denominate this stage secondary progressive multiple sclerosis (SPMS). **Figure 2.1b** schematically depicts the secondary progressive course of the disease.

Finally, the remaining 15% of MS patients tend to show a chronic-progressive course of the disease. We term this stage primary progressive multiple sclerosis (PPMS), in which relapses are rare or nonexistent and the clinical disease onset tends to occur later in life [24]. **Figure 2.1c** schematically depicts the primary progressive course of the disease.

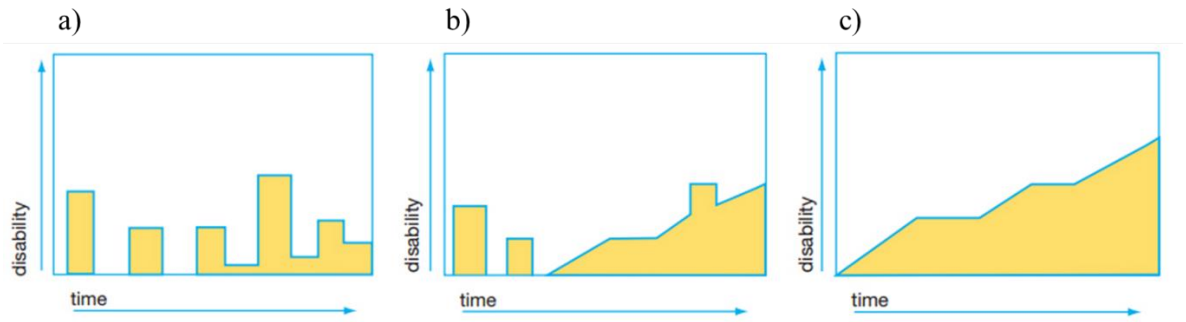

Figure 2.1: Schematic representation of the three types of multiple sclerosis: relapsing–remitting (a), secondary progressive (b) and primary progressive (c) [26].

The diagnostic criteria for MS follows a set of guidelines, often referred to as the McDonald criteria, which include a combination of criteria both of clinical as well as paraclinical nature to demonstrate the dissemination of lesions in space (DIS) and in time (DIT) and to exclude alternative diagnoses [27].

Even though the diagnosis of MS could be made on clinical grounds alone, magnetic resonance imaging (MRI) of the CNS has proved to be a useful tool supporting, supplementing and replacing some clinical criteria. Blood tests and cerebrospinal fluid (CSF) analysis can also be used for the diagnosis of MS, with the presence of two or more oligoclonal bands or a high immunoglobulin index adding as evidence of MS. Lastly, visual evoked potentials may provide additional support, especially in situations in which MRI abnormalities are few or have lesser specificity [27],[28].

As of December 2017, the Food and Drug Administration (FDA) has approved 15 medications for altering the course of multiple sclerosis. These medications are mostly approved for RRMS and aim at reducing the likelihood of the growth of new lesions, clinical relapses, and stepwise accumulation of disability. The major therapeutic goal of MS research is the prevention of SPMS. However, due to the unpredictability of this condition, optimal treatment and disease management remains a challenge, leading to a focus on the improvement of the quality of the everyday life of these patients [11],[24].

2.1.2 Cortical Lesions in Multiple Sclerosis

Around the 1960s, there was still little research on grey matter pathology from post-mortem studies. In a study from 1962, in a series of 22 cases it was found that 26% of all lesions were located in the cortex [29]. In 1970, another study with 60 cases found that the cortex was involved in 93% of the cases [30]. It was only decades later, with advances in imaging techniques, animal model studies and immunohistochemical analysis, that the fine cellular pathology associated with grey matter demyelination started to be unraveled [2].

A first categorization of cortical lesions into different classes was only proposed in 1999. At the time, cortical lesions were divided into seven different classes where the majority were associated with lesions found around the principal cortical veins. The remaining arose within the territory of smaller, superficial veins [2]. A simplification was made two years later reducing the number of cortical lesion types to three [31]. The currently accepted cortical lesion classification divides lesions into four types: type I or leukocortical lesions, lesions extending through both white and grey matter; type II lesions also called intracortical lesions, usually small and perivascular lesions found deep within the cortex that do not make contact with the brain surface of subcortical WM; and type III and IV, both subpial lesions but the former extends partly through the cortical width whereas the latter extends fully throughout the

cortical width, sometimes extending over several gyri or entire lobes [17],[32]. **Figure 2.2** depicts the different types of cortical lesions as assessed by histology.

Grey matter damage is thought to be either caused by inflammatory or non-inflammatory mechanisms. Inflammatory mechanisms are assumed to be a result of adaptive or innate immune responses. In the case of adaptive immunity, microglia activation and oligodendrocyte injury is caused by the release of cytotoxic molecules by infiltrates, such as infectious agents, in the meningeal space and/or in the adjacent perivascular spaces [33]. Some candidates for infectious agents are the Epstein–Barr virus or the Torque Teno virus [34],[35]. It could also be a result of cell contact-dependent mechanisms associated with T-cell mediated damage [36]. This response leads to neuronal cell death which results in morphological alterations in the cerebral cortex. Innate inflammatory mechanisms can also lead to microglial activation. Chronic inflammation of the subarachnoid or perivascular spaces, susceptibility to environmental factors like toxins, or neuronal loss can have a triggering effect, resulting in chronic and abnormal microglial response which leads to further grey matter damage [37],[38],[39].

In contrast, non-inflammatory mechanisms are thought to result from primary neurodegeneration and retrograde degeneration. The first is a result of metabolic compromise, particularly mitochondrial damage caused by reactive oxygen species produced by activated microglia and macrophages [40]. Retrograde degeneration would be caused by white matter damage, propagating backwards in cortical neurons whose axons have been damaged in white matter lesions or along white matter tracts, for instance, the corticospinal tract [33].

The relationship between white matter and grey matter damage and the causes of grey matter pathology remain to be fully understood today. Some studies suggest that white matter damage could lead to cortical damage, with white matter damage resulting in retrograde injury to frontal, temporal and motor cortical areas [41]. Moreover, cross-sectional MRI studies have shown significant correlations between the total volumes of grey matter and white matter in T1- and T2-weighted lesions [42].

Other studies suggest that white matter pathology cannot fully explain grey matter damage. For instance, cortical demyelination has been shown to exceed white matter demyelination [18] and most times cortical demyelination is found in regions where white matter is unaffected, with no correlation found between the two tissues [43]. Therefore, even though the involvement of axonal damage in retrograde loss of neurons has been established, this mechanism does not entirely explain the spectrum of grey matter pathology in multiple sclerosis. These studies highlight the importance of the independent study of grey matter pathology to assess its relevance in multiple sclerosis.

Grey matter pathology seems to be an early and frequent phenomenon in the disease [3]. A study found that cortical lesions were detected by MRI in the majority of patients with RRMS and SPMS [44]. Furthermore, in some patients, cortical damage would be denoted even before the appearance of lesions in white matter [45]. This emphasizes the semi-independent relationship that seems to exist between GM and WM but also the apparent early damage to the cortex in MS.

With regards to lesion location, post-mortem studies revealed that the representation of cortical damage is uneven. Demyelination was found to be more predominant in the cingulate gyrus, temporal and frontal lobes, in comparison with the occipital and paracentral lobe or the primary motor cortex [17], [18],[43]. Evidence of extensive demyelination was also found in the hippocampus [46].

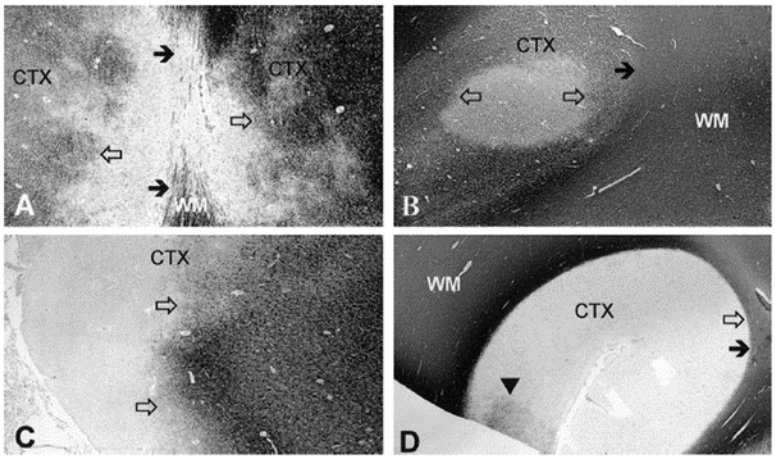

Figure 2.2: The different types of cortical lesions as detected histologically [17]. The cerebral cortex/white matter borders are delineated by closed arrows. The lesion borders are delineated by open arrows. Images A, B, C and D, depict lesion types I, II, III and IV, respectively. Abbreviations: WM = white matter; CTX = cerebral cortex.

Cortical lesions have been shown to correlate with physical disability and cognitive dysfunction [3]. One way to assess this is through the Expanded Disability Status Scale (EDSS) score, a method used in clinical practice as a means of quantifying and monitoring disability in MS patients. In a study which looks at the association between cortical lesion load and disability progression in MS, it was found that the EDSS score correlated with the number and volume of cortical lesions. In this regard, higher volumes or number of cortical lesions led to higher EDSS scores [47]. When looking at cognitively impaired RRMS patients, they presented a significantly higher number and volume of cortical lesions compared to those patients without cognitive deficits [45].

It has also been stated that the extent of cortical damage significantly influences the risk of entering a progressive phase. When investigating the relationship between cortical damage, the number of early relapses and the long-term course of MS, in the group with focal cortical damage at clinical onset, the probability of converting to SPMS increased proportionally with the number of cortical lesions [48].

These studies demonstrate the clinical relevance of cortical pathology in multiple sclerosis but highlight the present limited knowledge of cortical lesions and their impact in the disease and everyday life of the patients. MRI has enabled a better understanding of cortical pathology, but the biggest advance towards improving the detection and visualization of cortical lesions, thus giving insight into cortical damage, has come from ultra-high field (UHF) magnetic resonance imaging (MRI) systems. A more comprehensive analysis of the potential of UHF-MRI in MS will be given in **Section 2.3** of this dissertation.

2.2 Magnetic Resonance Imaging

2.2.1 Principles of Magnetic Resonance

Magnetic Resonance (MR) was first mentioned experimentally by Felix Bloch and Edward Purcell, awarded in 1952 with the Nobel Prize for Physics for their developments of new methods for nuclear magnetic precision measurements [49],[50]. However, it was not until Raymond Damadian's in vitro studies of rat tumors that its medical value was finally understood [51]. The formation of images stems from work from Paul Lauterbur in 1973 [52], while the production of images came a year later

from the work of Sir Peter Mansfield's group [53], awarding both with the Nobel Prize in Physiology or Medicine in 2003. Since then, many other researchers have contributed to the development of MR [54].

Magnetic Resonance Imaging (MRI) is an imaging modality that makes use of the magnetic properties of tissues in order to produce an image. It makes use of the hydrogen nuclei, abundant in the human body and found in water molecules as well as in fat. The hydrogen atom is a singly positively charged proton. For that reason, it will spin around its own axis, creating a magnetic moment that can interact with magnetic fields. When placed in a strong external magnetic field, the proton experiences a turning force, or torque, which tries to align its moment with the main field, similar to the way a compass needle aligns itself to the earth's magnetic field. As the proton cannot fully align with the external field, it will continue to experience a torque, resulting in a precession movement around the direction of the field. The frequency of precession is proportional to the external magnetic field and given by the Larmor equation:

$$\omega_0 = \gamma B_0 \qquad \text{(Equation 2.1)}$$

where γ is the gyromagnetic ratio constant, ω_0 the angular frequency and B_0 the external magnetic field. This equation entails that under the same magnetic field, all protons will precess with the same Larmor frequency. This is known as the *resonance condition* [55].

It is hard to measure the magnetization of the body in an equilibrium situation, when it is parallel to B_0. By tipping it into the *xy* plane (the transverse plane) by means of a 90-degree pulse, the average of the spins in the body, also known as the *net magnetization*, M_0, will generate a significant signal which can be measured. This is done by means of a radiofrequency (RF) pulse [55].

As soon as the RF pulse ends, the protons begin to relax back to their initial state. This leads to a dephasing of the spins and a realignment along the *z* axis. The signal measured starts to decay exponentially to zero due to the dephasing of the protons. This signal is called Free Induction Decay (FID) and is caused mainly by the inhomogeneity in the main static field. It is, additionally, a result of the interaction between spins, the *spin-spin relaxation*, which gives rise to the relaxation time *T2*. The loss of transverse magnetization is governed by the following equation [56]:

$$M_{xy} = M_0 e^{-t/T2} \qquad \text{(Equation 2.2)}$$

When protons interact with surrounding tissues, the *lattice*, energy is absorbed and lost. With the loss of extra energy, the protons start to return to the equilibrium state, bringing the magnetization along the *z* axis, M_z, back to M_0. This is the *spin-lattice relaxation*, described by the relaxation time *T1*. The recovery of longitudinal magnetization is described by the equation:

$$M_Z = M_0(1 - e^{-t/T1}) \qquad \text{(Equation 2.3)}$$

T1, unlike *T2*, is dependent on the field strength and increases with the increase in field strength. Moreover, the value of *T1* depends on the surrounding tissues, as the transfer of energy will be more efficient if the frequency of the excited protons corresponds to that of the neighboring molecules [56].

The FID signal is never measured directly. This is caused by the difficulty in measuring the MR signal immediately after the 90-degree pulse, as well as by the inhomogeneities in the magnetic field which produce variations in the frequency of precession of the sample volume indistinguishable from the *T2* signal decay. Therefore, the magnitude reduction of the FID signal is a result of the dephasing caused by spin-spin interactions, accounted for in the time constant *T2*, as well as from the dephasing

caused by the magnetic field inhomogeneities, accounted for in constant *T2**. The dephasing accounted for in *T2** is a result of the MR equipment, with stronger magnets associated with higher inhomogeneity effects. This effect can be reduced by means of a *rephasing pulse*, common in spin-echo sequences [57].

Instead of measuring the FID directly, two types of echo are measured: the gradient (GRE) and spin (SE) echoes. In the case of the former, a negative gradient is applied shortly after the excitation, which causes a rapid dephasing of the transverse magnetization. This is followed by a positive gradient which reverses the magnetic field gradient which will alter the frequency of precession and change the phasing of the spins. The height of the echo (S_{GE}) is defined by the FID decay curve:

$$S_{GE} = S_0 \, exp\left(-\frac{TE}{T_2*}\right) \qquad \text{(Equation 2.4)}$$

which depends on the relaxation time *T2**. In the case of the spin-echo sequence, the spins dephase naturally after the 90-degree pulse. Then, a 180-degree pulse is applied which flips the spins about the *y* axis. This pulse does not impact the spins' frequency of precession, but it reverses the phase angles. Over time, the spins return to the positive side of the *y* axis and create an echo. The spin signal is dependent on *T2* [55]:

$$S_{SE} = S_0 \, exp\left(-\frac{TE}{T_2}\right) \qquad \text{(Equation 2.5)}$$

Amongst the sequence parameters we find the time or repetition (*TR*) and the time of echo (*TE*). The *TR* is the time between a series of consecutive points. The *TE* is the time difference between the pulse of the RF-pulse and the peak measurement of the echo. It is the choice of pulse sequences and parameters that allows the acquisition of images with different contrasts.

Another important sequence is denominated Inversion Recovery (IR). This sequence resembles the SE sequence but is preceded by a 180-degree pulse which reverses the longitudinal magnetization. After that, the tissues undergo T1 relaxation in search for a recovery of magnetization along the positive direction. Upon the 90-degree pulse, the initial longitudinal magnetizations of different tissues are separated based on their different T1 relaxation times and a selection of a proper time of inversion (*TI*) value can lead to the suppression of certain tissues from the final image. This sequence contains a third time parameter, the inversion time, which corresponds to the distance between the 180-degree pulse and the 90-degree pulse [55].

MRI involves three types of magnetic field: the main magnetic field (B_0), the oscillating magnetic field of the RF pulses (B_1) and gradients. The latter is the element responsible for the localization of MR signals within the body and the basis of magnetic resonance imaging. The MR signals are encoded by means of spatial frequencies using phase encoding and frequency-encoding gradients. Every spatial frequency is sampled before a Fourier transform is used to alter this data and produce the MR image. The several echoes acquired in each TR are stored in a matrix often referred to as the *k-space* and it is the application of the Fourier transform to the k-space that enables the reconstruction of the MR image from all spatial frequencies. This is done under the assumption that any function can de decomposed into a set of periodic signals. The center of k-space corresponds to the low spatial frequencies, which ensure the structure of the image, while its edges contain the high spatial frequency, responsible for the details of the image [55].

2.2.2 Ultra-high Field MRI

Since the first developments in MR in the 1950s, a race for stronger magnetic fields had begun to overcome the inherently low sensitivity of this promising method [58]. Although until recently the highest available field used in clinical practice was 3 Tesla (T), since the 1990s it has become possible to use systems up to 9.4 T for neuroscientific and clinical research [59]. Some of the imaging techniques initially developed at 1.5 T but already applicable at 7 T include high-resolution anatomical MRI, functional MRI (fMRI), functional MR-Angiography, and susceptibility weighted imaging [60].

The most significant positive change with increasingly higher fields is the signal-to-noise ratio (SNR), the ratio of signal intensity in the image to level of noise. Early work demonstrated that the SNR parameter increases linearly with the external magnetic field, B_0 in the case of sample-dominated noise, most common in human imaging. This increase in SNR can be invested into higher spatial resolution or into higher temporal resolution in the case of dynamic processes [59].

A second parameter that increases with higher fields is the contrast-to-noise ratio (CNR), relevant in diagnostic imaging, particularly with regards to the ability to distinguish areas of interest, such as lesions, from normal tissue. The *CNR* parameter is given by the equation:

$$CNR = \frac{S2-S1}{noise} \qquad \text{(Equation 2.6)}$$

where *S2* is the signal in the area of interest, *S1* is the signal in the surrounding normal tissue and *noise* is the noise of the acquisition. As there are various imaging parameters that are dependent on field strength, it is no surprise that several MRI applications should profit from an increase in magnetic field strength. A prime example is fMRI, which provides mapping of areas of cortical activation during cognitive or motor tasks from blood-oxygen-level-dependent (BOLD) contrast [59].

The possibility of imaging with higher spatial resolutions is one of the advantages of ultra-high field (UHF) MRI. However, even with increased SNR at UHF, imaging times for high resolutions are long, which results in high motion sensitivity rates. This motion is a result of the long acquisition times as well as of higher motion sensitivities when measuring in smaller voxels. Due to hardware imperfections of the MRI systems, this motion will result not only in a shift and rotation of the images but also in geometric distortions due to gradient non-linearity and magnetic field variations, also called field inhomogeneities [59].

In the field of neuroimaging, ultra-high magnetic fields, such as 7 T, have allowed the visualization of the brain with unprecedented detail. In structural imaging, the increase in SNR and in image resolution allowed MR imaging to display finer anatomic detail. This is particularly relevant in neurological disorders, leading to an increase in lesion conspicuity, and a more accurate detection and characterization of brain abnormalities. This improvement in brain visualization can also be extended to other fields of MRI, including vascular and functional imaging, MR spectroscopy, diffusion MRI and multinuclear imaging [61].

2.2.3 MR Image Contrast

The choice of pulse sequences and the variation in acquisition parameters allows the creation of images with different contrasts. In fact, the interest in having a wide variety of MR sequences stems from the possibility to generate different types of contrast, and as a result, to extract different types of information. Every year, new pulse sequences are launched but, essentially, the majority of sequences fall upon one of the two major pulse sequence families: SE or GE. Both families exploit T1 or T2

contrast, but the GE family tends to lead to sequences with shorter acquisition times. The next sub-sections will highlight some of the sequences that are currently used in neuroimaging studies, with relevance for this dissertation [55].

2.2.3.1 T1-weighted

Images with T1-weighting, or T1-weighted (T1w), can be produced from SE or GE sequences. They use short TRs to ensure a difference in the recovery of longitudinal magnetization of the different tissues. A short TE is used to minimize T2 dependency during signal acquisition. Consequently, the tissues with the longest T1s will show the darkest signal, as opposed to those with shorter T1s that will appear brighter. Due to the short TR times, these images are faster to acquire and display great contrast between the tissues. Fat tissue has the shortest T1 and thus generates the strongest signal in the image. In the brain, white and gray matter will display intermediate intensities, with white matter appearing brighter due to the high myelin content, whereas CSF will display the lowest intensity due to its long T1. Due to its capacity to clearly differentiate the boundaries between tissues, T1w sequences are often referred to as *anatomy scans* [55],[56],[62]. **Figure 2.3a** depicts a brain image from a healthy volunteer acquired with T1w contrast at 7 T.

2.2.3.2 T2-weighted

T2-weighted (T2w) images can also be produced by SE or GE sequences. When images are produced by SE sequences, they reflect T2-weighting. When produced by GE sequences, they reflect T2* weighting, as the effects of the field inhomogeneities will not be removed. These images require a long TR, which reduces the effects of T1, and a long TE, which increases the differences due to T2, producing the wanted weighting. When focusing on the SE sequence, inversion of tissue contrast occurs due to the 180-degree pulse which explains why, for example, CSF appears brighter. Fluid tissues like CSF have a long T2 and thus maintain transverse magnetization longer than short-T2 tissues, which results in a higher signal intensity. Due to the sensitivity of these images to fluid collections and the prevalence of tissues with excessive fluid accumulations or high capillary density in pathology scenarios, these images can serve as a tool in medical diagnosis or disease monitoring [55],[56].

The Turbo Spin Echo (TSE) sequence has become the standard sequence for T2w imaging. Not only is it capable of creating great T2 contrast by a combination of a long TR and variable TE, but it offers reduced scan time due to the collection of multiple signal echoes upon each excitation pulse [55]. **Figure 2.3b** depicts a brain image from a healthy volunteer acquired with T2w-TSE contrast at 7 T.

2.2.3.3 FLAIR

Fluid attenuated inversion recovery (FLAIR), or T2-FLAIR is an IR sequence with interest in the field of neuroimaging that through careful selection of a proper TI time, nulls the signal from CSF whilst creating a strong T2-weighting by means of a long TE. Despite the longer imaging times, the reduction in flow artefact from CSF and the high T2 weighting enables better anatomical detail to be seen in the brain stem and allows better contrast in areas close to CSF. This technique has proved useful in revealing lesions, including cortical, periventricular, and meningeal diseases that were difficult to see on conventional images and that can result from a variety of neurological pathologies [55],[63],[64]. **Figure 2.3c** depicts a brain image from a healthy volunteer acquired with FLAIR contrast at 7 T.

2.2.3.4 MPRAGE

Magnetization prepared rapid acquisition by gradient echo (MPRAGE) is a GE sequence that resorts to segmentation of k-space and non-steady-state methods, instead of conventional localization methods, to acquire the MR image. As a result, the MPRAGE can produce high-resolution, T1-weighted images with fine anatomical detail in a short scan time, which has made it attractive for structural brain

imaging in clinical and research settings [55],[65]. **Figure 2.3d** depicts a brain image from a healthy volunteer acquired with MPRAGE contrast at 7 T.

2.2.3.5 MP2RAGE

Magnetization prepared 2 rapid acquisition gradient echoes (MP2RAGE) is a sequence that aims at accounting for the increased inhomogeneity of the B1 field, responsible for the creation of intensity variations throughout the image, from higher static magnetic fields. It is an extension of the MPRAGE sequence which acquires 2 volumes following each inversion, allowing the estimation of the bias from B1 and its correction from the image. In a conventional MPRAGE, the signal is not only dependent on T1 contrast but also on M0 and T2*. By acquiring two MPRAGE images that only differ in their inversion times, they will be equally affected by B1, M0 and T2* and thus a combined image that takes their ratio into account will be independent of these added parameters. Bias field-independent images can be acquired through means of quantitative imaging, usually by T1 mapping [66][67]. **Figure 2.3e** depicts a brain image from a healthy volunteer acquired with MP2RAGE contrast at 7 T.

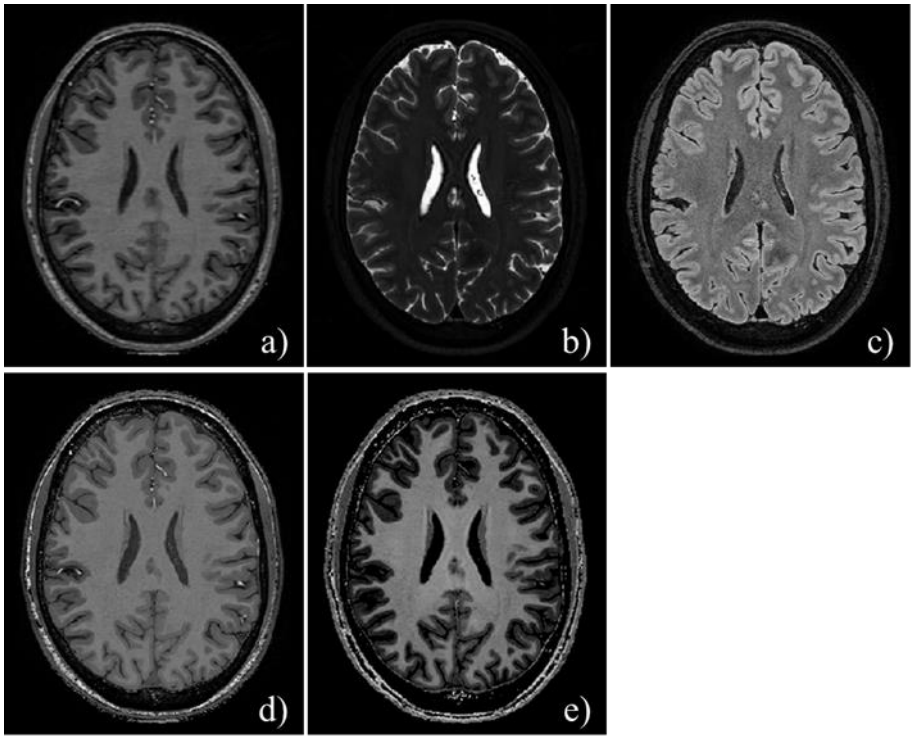

Figure 2.3: MRI scans acquired at 7 T with different contrasts, namely, T1w (a), T2w-TSE (b), FLAIR (c), MPRAGE (d) and MP2RAGE (e).

2.2.4 MR Image Processing

Medical imaging modalities have been described as one of the highest achievements of the twentieth century in the field of medicine. Their widespread use in clinical as well as scientific research highlights the potential of such techniques. But just as important as the acquisition of the data itself, is the handling of such data. With this regard, the main objectives of image processing and analysis are to improve the quality of the data acquired as well as to extract information of interest in a manner that is robust, time efficient and accurate [68].

As a medical imaging technique of high relevance today, MRI also requires proper data handling in order to be used as a diagnosis and research tool. When dealing with structural MRI data, certain pre-processing steps should be considered to improve its quality. These include noise reduction, motion correction, coregistration, skull stripping, spatial smoothing and bias correction. Processes like the ones mentioned ensure a better quality of the data for posterior analysis where new processing steps will occur, namely brain segmentation, subject registration, and cortical group surface creation, in the context of group analysis.

The choice of which processes to use and to incorporate into project pipelines is highly dependent on the study at hand, on its requirements as well as on the hypotheses to test. Likewise, the methodology chosen for the application of such processes will also depend on the needs of the project and also on a compromise between the previously mentioned factors: accuracy, time efficiency and robustness. The next sub-sections will highlight some of the imaging processing applied to MRI data with relevance for this dissertation.

2.2.4.1 Bias Correction

Bias is the presence of intensity nonuniformities in MRI images and results from inhomogeneity in the external static magnetic field, B_0, and RF excitation fields, as well as from regional differences in the magnetic properties of the imaged tissues. At 7 T these effects are intensified due to the greater main magnetic field and RF field inhomogeneities [69],[70].

Even though it is not required to correct for bias, it is known that without it the accuracy of computational imaging analysis processes such as brain segmentation and registration can be compromised [69],[71]. Furthermore, in the context of MS, it is known that subpial lesions may go undetected if bias is not corrected for [72].

Over the years, various methods have been proposed for the correction of bias. The most recognized ones can be categorized as either low-frequency models, hypersurface models or statistical models. The first, which assumes bias to be made of low-frequency components resorts to lowpass filtering for its correction. The last two are adaptive to the image and tend to present more stability which makes them more appealing. Notwithstanding, their increased complexity will also result in additional memory use and increased computing time.

When resorting to an image analysis software for bias correction, this step tends to appear merged with image segmentation in a single framework and therefore its success is also dependent on the performance of the segmentation [71]. This is the case in the software Statistical Parametric Mapping (SPM).

The statistical model used within SPM for the bias correction has a parametric nature, modelling the intensities of different tissues as a mixture of Gaussians. The bias is assumed to be multiplicative and the relation between bias and noise can be described by the following equation:

$$yi = \frac{(\mu i + ni)}{\rho i} \qquad \text{(Equation 2.7)}$$

In this model, the noise (n_i) is added to the signal (μ_i) before the scaling effect by bias (ρ_i) is considered. Bias is then parametrized as the exponential of a linear combination of low frequency basis functions [73].

Because the true amount of bias in MRI images is unknown it is generally difficult to accurately evaluate the performance of the methodology chosen. However, it is possible to assess its performance qualitatively through visual inspection of the corrected volumes in comparison with the original

volumes, or through inspection of the bias fields. Intensity histograms are another important qualitative tool for data quality check [69].

2.2.4.2 Registration

Image registration corresponds to the process of aligning two images. This way, common features overlap and differences between the two images, when existent, are emphasized and readily visible to the naked eye [74].

Coregistration is a type of registration which aims at spatially aligning a series of images that belong to the same subject with respect to a fixed or reference image. This image can be either the first volume acquired, a mean volume or a template space. It is a within-subject registration mostly associated with the alignment of structural and functional data as a way to map functional information into anatomical space. However, this alignment can also be done between MRI modalities or between images acquired in different sessions, as would be the case in a longitudinal study. This way, it can also serve as a motion correction step, to account for image differences resulting from slight subject head movement between scans [75].

Registrations, regardless of the type, require the use of transformations for the alignment to be successful. In order to transform the source or moving image to match the reference or fixed image, it is important to determine a mapping from each individual voxel in the reference image to a corresponding position in the source image. The source image then needs to be re-sampled at the new positions.

Rigid body transformations are a subset of affine transformations and account for only rotations and translations. When dealing with 3D volumes, this type of transformation is parameterized by three translations and three rotations about the different axes. Therefore, for each point *(x1, x2, x3)* in an image, an affine transformation can be defined into the coordinates of another space *(y1, y2, y3)*. This is usually represented by a simple matrix multiplication ($y = Mx$):

$$\begin{bmatrix} y1 \\ y2 \\ y3 \\ 1 \end{bmatrix} = \begin{bmatrix} m11 & m12 & m13 & m14 \\ m21 & m22 & m23 & m24 \\ m31 & m32 & m33 & m34 \\ 0 & 0 & 0 & 1 \end{bmatrix} \begin{bmatrix} x1 \\ x2 \\ x3 \\ 1 \end{bmatrix} \qquad \text{(Equation 2.8)}$$

where in the transformation matrix *M*, the forth column corresponds to the translations and the first three columns to the rotations around the three orthogonal planes [75].

In SPM, coregistration is done using a rigid body model in two steps. In the first step, the parameters are estimated and stored in a transformation matrix. The second step is the transformation itself, where one of the images is altered according to the estimated matrix [75]. The interpolation of data between spaces is done, by default, using the B-spline interpolation method.

There are several possible approaches to rigid body registration. The most recognized ones are either frame based, surface based, point landmark based or voxel based. The registration method used in SPM falls in the category of voxel similarity-based registration algorithms and therefore aims at optimizing a function measuring the similarity of all possible pairs of voxel grey-values. The main advantage of such method is that feature calculation is simplified. Yet, simple correlation of grey-values between modalities only works if a linear mapping between grey-values exists [76].

Subject registration, also referred to as spatial normalization, is an inter-subject registration of images acquired from different subjects. Its principal aim is to reduce the anatomical variability in brain scans obtained from different subjects as a result of factors such as brain morphology, age or pathology.

It is a procedure of relevance in voxel-wise group analysis of fMRI data as well as in studies of WM using diffusion tensor imaging. Furthermore, it can also be used to learn the nature of a specific brain tissue, landmark or structure from comparison with a template image or to assess volume changes in different anatomical structures over time, with relevance in diagnosis and disease monitoring [77].

Unlike coregistration where rigid body transformations are enough to perform the alignment of interest, in subject registration, to account for brain variability amongst subjects, non-linear transformations need to be taken into consideration, which generate deformations. This has the downside that processes will become increasingly more robust and complex and as a result more time consuming.

The main objective of most inter-subject image registration algorithms is to find a displacement field such that the warped image is as similar as possible to a reference or template image. For a given pair of subject and template images, algorithms differ mainly in the approach taken to modeling and estimating the field. A possibility is to model the displacement field in an elastic object or a viscous fluid. These methods are governed by partial differential equations that model the physical phenomenon [77].

Diffeomorphic anatomical registration through exponentiated lie algebra (DARTEL) is an algorithm for diffeomorphic image registration incorporated into a toolbox in SPM. It uses a single flow (velocity) field as a displacement field which remains constant over unit time. The differential equation which describes the evolution of a deformation is:

$$\frac{d\Phi}{dt} = u(\Phi^{(t)}) \qquad \text{(Equation 2.9)}$$

where u is the velocity field, and Φ the deformation. The DARTEL registration implies a simultaneous minimization of a measure of the difference between the image and the warped template as well as a minimization of an energy measure of the deformations used to warp such template. This energy is obtained through the integration of the energy of the velocity fields over time. The local stretching, shearing and rotating of the deformation field can be accessed through the Jacobian matrices. These matrices correspond to the derivatives of the deformations, which form a second order tensor field [78]:

$$J_\Phi(x) = \begin{pmatrix} \frac{\partial \Phi_1(x)}{\partial x_1} & \frac{\partial \Phi_1(x)}{\partial x_2} & \frac{\partial \Phi_1(x)}{\partial x_3} \\ \frac{\partial \Phi_2(x)}{\partial x_1} & \frac{\partial \Phi_2(x)}{\partial x_2} & \frac{\partial \Phi_2(x)}{\partial x_3} \\ \frac{\partial \Phi_3(x)}{\partial x_1} & \frac{\partial \Phi_3(x)}{\partial x_2} & \frac{\partial \Phi_3(x)}{\partial x_3} \end{pmatrix} \qquad \text{(Equation 2.10)}$$

In SPM, subject registration using DARTEL is performed in two steps. In the first, a group template is created from the individual subject images. Usually, the images used for the template creation are the resulting segmentation files differentiating each individual brain into its tissue classes, GM and WM. As a result of this step, individual flow fields containing the deformation information required to take each individual brain into this common space are created and can be used in the second part to create warped files and allow a spatial normalization of the images with regards to the template. Although DARTEL is considered inferior to variable velocity diffeomorphic models, its increase in speed of execution remains an advantage of practical nature when compared such models [78].

2.2.4.3 Segmentation

Segmentation consists in the separation of an image into disjoint regions of similar attribute which, ideally, should not overlap, be homogeneous and semantically meaningful. As a result, an image

of labels describing each region or a set of contours associated with region boundaries should follow [79],[80].

In brain MRI studies, an important component of the data analysis is the classification of the data into specific tissue types, as well as to identify and describe distinct anatomical regions. Typically, a differentiation of the three main regions of interest, namely WM, GM and CSF is implied. Therefore, a classification step is required, consisting in the assignment of each pixel or voxel, in a 3D image, to each tissue class. This implies that segmentation and classification are interlinked [80]. Additionally, segmentation can be performed to identify and isolate findings which are a result of disease.

Segmentation methods can be divided into intensity-based methods, atlas-based methods, surface-based methods or hybrid segmentation methods. Manual segmentation can also be included as a segmentation method, where the operator segments and labels the image by hand, typically in a "slice-by-slice" manner when dealing with 3D image volumes [80].

The brain segmentation procedures used in the software packages SPM and FreeSurfer are intensity-based, most specifically classification-based. Therefore, the voxel classification is performed with regards to its intensity value, typically using intensity histograms and by fitting a mixture of Gaussian functions. This allows an inference to be made on the probability of a given intensity corresponding to a given type of tissue [80].

One of the most commonly used parametric classifier in classification-based methods is the Bayesian classifier which models the probabilistic relationships between the attribute set and the class variables, used thereafter for estimating the class probability of the unknown variable. Both software packages make use of this Bayesian framework which contains three probability distributions: the prior distribution $P(x)$, the posterior distribution $P(x \mid y)$, and the conditional distribution $P(y \mid x)$, also known as likelihood. Here x stands for the estimated label output and y for the observed image. In the Bayes framework, the prior distribution is associated with the initial knowledge of likely configurations before any observation. The posterior distribution is derived after observation and the likelihood is defined as the probability of obtaining a particular observation given a set of model parameters. The relation between the three distributions is defined in the Bayes rule [80]:

$$P(x \mid y) = \frac{P(y \mid x)\, P(x)}{P(y)} \propto P(y \mid x)\, P(x) \qquad \text{(Equation 2.11)}$$

In SPM, segmentation or tissue classification requires an initial registration of the images with tissue probability maps. After registration, the tissue maps represent the prior probability of the different tissue classes being found at each position in the image. The Bayes rule allows the combination of the priors with tissue type probabilities derived from voxel intensities to provide the posterior probability [73]. In FreeSurfer, the Bayesian approach is also used to incorporate prior information, but in the end each voxel is assigned to one of 37 neuroanatomical classes. To account for the inherent ambiguity of class intensity distributions when using a larger class set, further space-varying classification procedures are added [81].

2.2.4.4 Cortical Surface Creation

The cerebral cortex surface is a highly folded sheet with most of its area buried within folds. This makes the cortex a difficult area for computational and visualization purposes. In order to compare anatomical features between subjects, it is necessary to establish a mapping between the locations in the different brains [82]. Most comparisons rely on 3D registration procedures but because the intrinsic topology of the cerebral cortex is the one from a two-dimensional (2D) sheet, this will result in an

underestimation of the true distance along the cortical sheet caused by poor anatomical precision and by poor estimation of the geodesic distances along the surface given by the cartesian distances [83].

One of the approaches to surface-based alignment consists in the application of fluid deformation to flattened representations of the cortical surface. This postflattening approach is driven by a small number of manually labeled anatomical landmarks and requires several incisions to be made to the cortical surface to allow it to lie flat without distortions. Not only do these manually added incisions introduce variability in the resulting surface, due to the difficulty in making incisions in similar points across subjects, but because the flattened surface boundary is not convex, the average surface-based coordinate of points on opposite sides of a cut may fall outside the surface [83].

Another possibility for surface-based alignment is the spherical coordinate system. In this system, the cortical surface of each hemisphere is topologically equivalent to a sphere. The reconstructed surface of each individual subject is first mapped onto a sphere, using a maximally isometric transformation, before being morphed into an average surface by a combination of folding-alignment and isometry-preserving forces. Amongst the advantages of this coordinate system are the conservation of the intrinsic topological cortical surface structure, the minimization of metric distortions and the nonnecessity of manual labeling of anatomical landmarks [83].

FreeSurfer makes use of the spherical coordinate system for its cortical surface creation. The robust procedure of cortex reconstruction is composed by several subtasks which include: the correction of intensity bias from magnetic field inhomogeneities followed by an image normalization; the removal of extracerebral voxels, often referred to as *skull-stripping;* a brain segmentation, created from global grey-scale-based thresholds or classes to label different tissue types; a representation of each cortex hemisphere from the computation of cutting planes responsible for avoiding connectivity between hemispheres; the generation of a uniquely connected mass representing the white matter structure of each hemisphere; and the triangular tessellation and deformation to produce an accurate and smooth representation of the grey/white interface as well as of the pial surface [84].

FreeSurfer also uses a unified procedure which, by taking into account the reconstructed cortex, allows the possibility of inflating the cortical surface, allowing the proper visualization of the sulci; the possibility of flattening an entire hemisphere, displaying the entire hemisphere in a single view; and the possibility of morphing the hemisphere into a surface that maintains the topological structure of the original surface, but has a natural coordinate system. These features are particularly relevant for the analysis of fMRI properties but can be extended to other types of analyses [82].

2.3 MRI in Multiple Sclerosis

2.3.1 Diagnosis of Multiple Sclerosis

The main requirement for the diagnosis of MS as shown in the McDonald criteria is evidence of damage in the CNS that is disseminated in time and space. Therefore, damage should occur on different dates and should be evident in two or more parts of the CNS [27].

Since the introduction of MRI into clinical use around 1980, this technique has developed into the widespread medical imaging tool it is today, used for depicting a variety of anatomical regions and answering questions of morphological or functional nature. It is no surprise that MRI emerged as one of the most relevant tools of diagnosis in medical imaging, decisive in the diagnosis of MS [59].

In 2015, members of the Magnetic Resonance Imaging in MS network released a set of guidelines for the implementation of MRI of the brain and spinal cord in the diagnosis of patients who are suspected

of having MS. This set of guidelines took into account several publications on the 2010 revisions of the McDonald criteria [28] which concerned the use of MRI. With regards to a possible standardized protocol for brain MRI, it is recommended to perform a multisequence MRI with a field strength of at least 1.5 T (preferably 3 T) with a maximum slice thickness of 3-mm and an in-plane spatial resolution of 1x1 mm (in voxel size, 3x1x1 mm). The entire protocol should not exceed 30 minutes and the mandatory sequences include, in a baseline evaluation, T2w sequences acquired in at least two planes, commonly axial and sagittal, and a contrast-enhanced T1w sequence, if lesions are seen on the T2w sequences. For the contrast enhancement, gadolinium is the contrast agent used as it allows the distinction between acute and chronic lesions, therefore allowing the demonstration of DIT. In a follow-up examination a new T2w image is required to detect active lesions. Additionally, although not mandatory, a postcontrast T1w image is recommended to facilitate the detection of new active lesions [85].

Following the 2017 revisions to the McDonald criteria, the potential of cortical lesions to contribute to diagnosis has been appreciated leading to the addition of cortical lesions to the MRI criteria to demonstrate DIS. As a result, in the current criteria it is stated that DIS can be demonstrated by one or more T2-hyperintense MS lesions in at least two areas of the CNS which now include periventricular, cortical or juxtacortical, and infratentorial brain regions, as well as the spinal cord. With regards to DIT, it can be demonstrated by the simultaneous presence of gadolinium-enhancing and non-enhancing lesions at any time or by a new T2-hyperintense or gadolinium-enhancing lesion on a follow-up MRI, with reference to a baseline scan, regardless of when the baseline MRI was performed. However, when it comes to cortical lesions, it is also mentioned that standard MRI currently has limited capacity to detect these types of lesions and that care must be taken in order to properly distinguish lesions from neuroimaging artefacts, which could result in overdiagnosis [86].

2.3.2 MRI and Cortical Lesions

2.3.2.1 Conventional MRI in Cortical Lesion Detection

There is no doubt that due to its higher sensitivity compared to other methods, MRI has become the most important paraclinical tool for the diagnosis of MS. Such accomplishment is also a result of the rapid advance of MRI techniques over the past few years. Yet, even then, grey matter pathology remains a challenge with a significant part of cortical lesions continuing to go unnoticed especially when using standard or high field strength MRI. For instance, at 1.5 T and 4.7 T MRI, sensitivity for intracortical lesions in a post-mortem sample when using T2w and FLAIR images is still below 10%, while mixed grey matter-white matter lesions can be detected in four out of five cases [87].

Specific grey matter pulse sequences seem to provide higher sensitivity to cortical pathology. The double inversion recovery (DIR) sequence with its ability to simultaneously suppress CSF and WM has enabled higher detection rates at 3 T, especially in the infratentorial region [88],[89]. Likewise, the phase-sensitive inversion recovery (PSIR) sequence has also proved to be promising, providing even more sensitivity to cortical lesions than the previous sequence [90].

Another highly mentioned sequence is the MPRAGE. Because of its higher resolution, finer anatomic detail and clear grey-white matter tissue contrast, this sequence allows a better delineation of lesion borders and surrounding grey-white matter junction, improving classification accuracy. In a study where 119 lesions were identified and divided into two different categories on both DIR and PSIR, in 30 cases MPRAGE overturned the original classification [91].

Despite these findings, the detection of cortical lesions at standard clinical field strength is still suboptimal, showing limited sensitivity and reproducibility as well as lack of accuracy [85].

2.3.2.2 Ultra-high Field MRI in Cortical Lesion Detection

Moving towards UHF scanners has the advantage of improving signal-to-noise ratio, thus allowing the visualization of smaller structures due to the improved spatial resolution. The main advantages of these systems in multiple sclerosis are related to a better visualization of WM lesions and their morphological characteristics, a higher sensitivity to GM lesions and their location and increased information of pathological nature particularly with regards to iron accumulation [5].

Working with higher strength fields also imposes additional problems, as, for example, an increase in MRI field strength results in increased field inhomogeneity, which can result in difficulties in lesion identification and in the application of segmentation algorithms. Metabolic analysis can also be compromised [5].

The use of 7 T MRI has resulted in an improvement in the detection and visualization of MS lesions compared to lower strength fields. When comparing 1.5 T and 7 T, WM lesions were depicted as more easily detected and delineated at 7 T, with 42% of patients showing additional WM lesions at 7 T. Accuracy is also mentioned, with a higher resolution favoring a better differentiation between juxtacortical WM lesions and cortical lesions. However, at 1.5 T, no cortical lesions could be identified with certainty [92]. When comparing 3 T and 7 T, increased lesion detection seems to be confined to GM, with the 7 T FLAIR sequence detecting 238% more cortical lesions than the respective 3 T sequence [93].

As a result of a better visualization of the distribution of GM lesions, it has become possible to further characterize them into their different types, namely type I (leukocortical), type II (intracortical) and type III/IV (subpial extending partly or completely through the cortical width), as suggested histopathologically [4],[17]. **Figure 2.4** depicts the different types of cortical lesions as assessed by 7 T in a post-mortem setting while **Figure 2.5** depicts the lesions as assessed in an in-vivo setting.

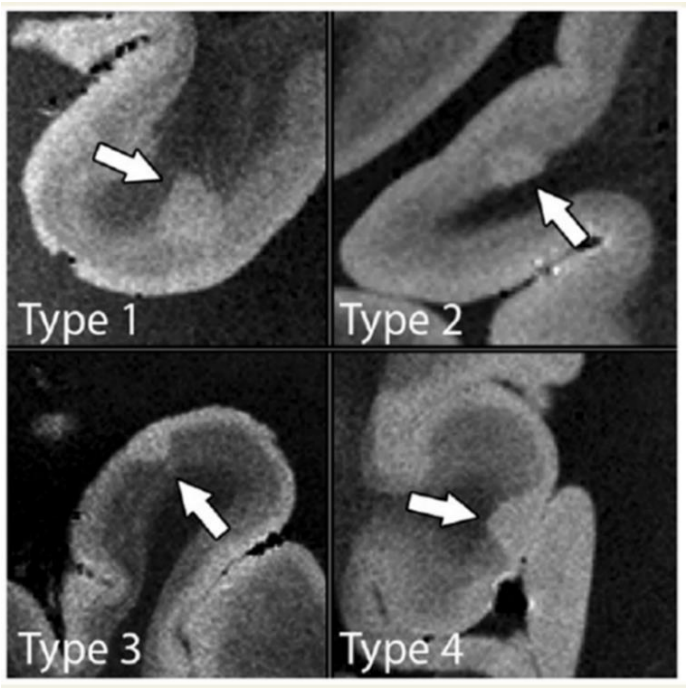

Figure 2.4: The different types of cortical lesions detected with 7 T T2* MRI in a post-mortem study [6].

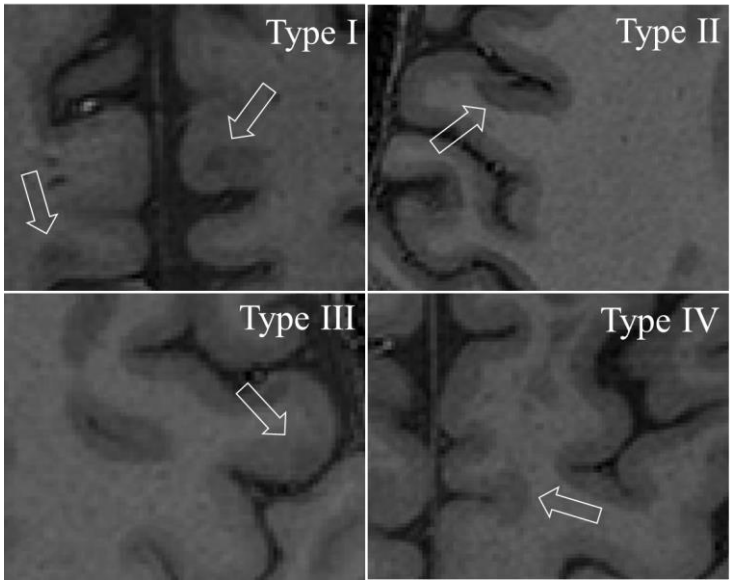

Figure 2.5: The different types of cortical lesions detected with 7 T MPRAGE MRI in-vivo.

2.3.2.3 Sensitivity to Cortical Lesions at 7 T

Despite the increase in total cortical lesion count, sensitivity for cortical lesions appears to be related to lesion type and to poor contrast and visibility caused by varying degrees of inflammatory activity within lesions [6].

In a study which aims at understanding whether cortical lesions occur in pediatric-onset MS patients, almost all lesions identified were classified as leukocortical, and only one of the three raters identified a few lesions as purely intracortical. Moreover, only 3 subpial lesions could be clearly identified. The authors refer that it is still to be determined whether subpial lesions are indeed a rare occurrence in pediatric-onset or if, instead, further sequence optimization was necessary to allow their proper visualization [7]. A post-mortem study reinforces this difference in lesion type detection by showing that when it came to lesions extending from the pia downwards into the cortex, i.e. type III and IV subpial lesions, a maximum sensitivity was found of 68% for type IV lesions and 32% for type III lesions. With regards to type I leukocortical lesions, a detection rate of up to 100% has been reported while type II intracortical lesions, even in post-mortem tissue samples, where there is an almost unrestricted acquisition time and movement artefacts are almost absent, were barely visible with MRI. They presented a maximum sensitivity of only 11% which is assumed to be caused by the small size of this type of lesion [6].

In addition to lesion type, sensitivity rates appear to be related to the MRI sequence used, which impacts the contrast between tissues. When comparing the performance of the MP2RAGE sequence and two T2*-weighted (T2*) sequences at 7 T, more cortical lesions were identified on MP2RAGE. In fact, 49% of cortical lesions were identified on both MP2RAGE and at least one of the T2* sequences, but 43% were identified only on MP2RAGE [94]. While examining the feasibility of the FLAIR and DIR MR sequences when compared to T1w and T2w sequences at 7 T, cortical and total lesion counts were higher for the FLAIR and DIR sequences. The same was seen with regards to lesion to white matter and grey matter contrast ratios [72]. Another study refers the potential of using magnetization transfer imaging (MTI) in cortical pathology over the MPRAGE, T2* and DIR sequences, specifically in detecting intracortical lesions [95]. When looking for the sequences used in clinical practice, the FLAIR

sequence came out as best at detecting cortical GM lesions, when compared to GM-specific DIR and conventional T1w and T2w sequences [96].

This difference in sensitivity with regards to sequence type is also present in the post-mortem study previously mentioned [6], where maximum sensitivity for type IV lesions of 68% was attained for a T2w image, whereas the maximum sensitivity for type III lesions came from the T2* sequence. Optimal sensitivity of 100% for type I lesions was obtained with T2w contrast and 11% sensitivity for type II lesions was acquired with both the FLAIR and T2w sequences. However, none of the five sequences involved detected significantly more lesions, leading the authors to propose that although increasing field strength has a clear effect on grey matter lesion detection, the type of sequence that is chosen at UHF does not seem to be as important. These studies seem to highlight a lack of consensus within the research community with regards to what sequences are optimal for the detection of cortical lesions at 7 T.

It has been acknowledged that not all brain regions are equally affected by the disease. In a 2003 study, it was already suggested that cortical demyelination seemed to be dominated by subpial lesions [17]. A 2016 study supports this fact by highlighting the larger incidence and size of lesions in cortical sulci and in deep invaginations of the brain surface, i.e. the cingulate gyrus and the insular cortex. Such topographical distribution was significantly associated with subpial cortical demyelination [97]. In a longitudinal study from 2019, it was revealed that new cortical lesions tend to develop predominantly intracortically and within cortical sulci. In the study, lesions are only categorized into leukocortical, if involving WM, or intracortical, where subpial lesions are included [98]. If subpial lesions have a low detection rate in MRI, even at UHF, this means we are still missing a large part of the cortical pathology present in MS. An important way of assessing to what extent these lesions are being detected is to look at post-mortem studies where a prospective as well as a retrospective scoring are performed, following the assessment of histopathological results.

In a study which aims at verifying the potential of the T2* sequence histopathologically and comparing it with the standard T2w sequence at 7 T, it is revealed that not only does the standard sequence detect more cortical lesions overall but that both sequences are only capable of detecting 16% and 28% of the total of GM lesions detected histopathologically, respectively. These numbers increase to 84% and 85%, respectively, in the retrospective study, i.e. when histopathologic information (lesion type, location) was revealed to the reader. Histopathology also revealed a specificity of 91.4% for the T2w sequence and 90.5% for the T2* sequence associated with the presence of false positives. The authors refer that the prospective rates could be improved with better a priori observer training [99]. When comparing the sensitivity of T2*-weighted gradient-echo and inversion recovery turbo-field-echo sequences for cortical multiple sclerosis lesions at 7 T, there is an improvement from 46% to 93% and from 42% to 82%, respectively, when moving from prospective to retrospective scoring [100]. These results show that cortical pathology is far more extensive than what ultra-high field 7 T images reveal for even retrospectively a significant percentage of cortical lesions is missed. However, the reason why not all cortical multiple sclerosis lesions are visible, even retrospectively, remains unclear.

2.3.2.4 Current Challenges

One of the concerns of the McDonald criteria is the possibility of misdiagnosis. It is even suggested that in addition to confirming dissemination in space and time, diagnostic rigor in the interpretation of clinical data, imaging findings, and test results is necessary [86].

Besides the inability to reach total sensitivity to cortical lesions, another limitation of MRI is lack of specificity with regards to differentiating tissue alterations in the brain parenchyma, namely demyelination and remyelination. As it happened in some of the previously mentioned studies, some

hyperintensities detected on MRI turned out to be areas of incomplete demyelination or partial remyelination when looked at from a histopathological view. This highlights the need for an imaging marker for remyelination and the currently difficulty in identifying and excluding false positives in in-vivo studies [6],[99].

There is no doubt that 7 T MRI has improved the detection of cortical lesions allowing the possibility for better understanding cortical pathology. In fact, the potential of 7 T MRI in cortical pathology goes beyond lesion sensitivity, with relevance in cortical thickness studies, where it has allowed higher accuracy for cortical thickness determination [101] or in iron studies, allowing a better understanding of changes in iron distribution in the brain and particularly within lesions, with potential in clinical differential diagnosis [102]. The potential of 7 T MRI in cognition and disability related studies has also been assessed, where it has been determined that cortical lesions are associated with cognitive and physical disability in MS and that leukocortical and subpial lesions have differing clinical relevance [8]. Notwithstanding, there is still a lot to be understood about cortical pathology and for that reason, research within this field is highly encouraged and should be expected in the following years as we are still only now visualizing the "tip of the pathological iceberg" [103].

3 Methodology

In this chapter, the methodology tested and implemented in this dissertation is described. Firstly, information related to the recruitment of subjects, equipment used in the acquisition of the data and specific MRI sequence parameters is given in **Section 3.1**. In **Section 3.2**, the image processing pipeline is described and schematically shown before the methodology followed in the different pipeline steps is presented in individual sections, to allow a better display and organization of the information.

3.1 Subject Recruitment and Data Acquisition

Twelve patients (age range: 23-65; age average: 43) mildly to moderately affected (EDSS of <5.5) with RRMS or SPMS and six healthy age-matched controls (age range: 24-57 years; age average: 37) were included in this project. The subjects correspond to a sample of the total number of recruited subjects for the CLiMS project. Of the twelve patients and six healthy controls, six and three, respectively, were females. The data acquisition took place between October 2018 and April 2019. All needed permissions from the local ethics committee, data protection and the Danish Medicines Agency had been obtained beforehand.

All participants were studied with whole-brain ultra-high field MRI at 7 T, using a research-only 7 T Achieva MR system (Philips, Best, The Netherlands) located at DRCMR. Whole-brain MR scanning was performed with a dual transmit, 32-channel receive head coil (Nova Medical Products).

The patients were scanned using four different MRI modalities, namely 3D-MPRAGE, 3D-FLAIR, 3D-T1w and 3D-T2w-TSE. The sequence parameters are provided in **Table 3.1**.

Table 3.1: Sequence parameters per pulse sequence at 7 T.

Contrast	3D-T1w	3D-FLAIR	3D-MPRAGE	3D-TSE
TE (ms)	2.2	391	3.2	319
TR (ms)	5.0	5000	7.5	3719
TI (ms)	-	1825	1100	-
Flip Angle (º)	7	55	8	100
FOV (mm^3)	246 x 246 x 174	230 x 230 x 168	228 x 228 x 166	256 x 256 x 190
Matrix (-)	248 x 246 x 174	328 x 330 x 240	352 x 348 x 256	320 x 322 x 475
Acq. Res. (mm^3)	0.99 x 0.99 x 1.0	0.70 x 0.70 x 0.70	0.65 x 0.65 x 0.65	0.80 x 0.80 x 0.80
Rec. Res. (mm^3)	0.85 x 0.85 x 1.0	0.69 x 0.69 x 0.70	0.65 x 0.65 x 0.65	0.40 x 0.40 x 0.40
Acq. Time (min/sec)	01:55	11:10	07:13	11:54

TE – Time of Echo; TR – Time of Repetition; TI – Time of Inversion; FOV – Field of View;
Acq. Res – Acquisition Resolution; Rec. Res. – Reconstructed Resolution; Acq. Time – Acquisition Time.

3.2 Image Processing Pipeline

This section describes the different approaches tested and the methodology implemented that gave rise to an image processing pipeline for MRI data of higher resolution obtained at a field strength of 7 T. This section is split so that each individual pipeline step can be easily accessed and to allow a better organization of the information.

The entire pipeline consists of five distinct processes: bias correction (**Section 3.2.1**), coregistration (**Section 3.2.2**), brain segmentation (**Section 3.2.3**), subject registration (**Section 3.2.4**) and surface creation (**Section 3.2.5**). The first two steps were applied to the entire dataset, i.e. healthy controls and patients. After this and in line with the segmentation step, a manual lesion segmentation was performed on the patients' data (**Section 3.2.3.1**). To lead to the acquisition of an average brain surface from the patient data where the sum of cortical lesions could be overlaid, the final two steps were applied to the patient data only.

The contrast of reference used in all pipeline steps was the MPRAGE due to its good resolution and T1w-contrast, commonly used in similar analyses. In the coregistration step, all contrasts were used to ensure a good alignment between the subjects' individual data and the possibility to perform the manual lesion segmentation in any of the available contrasts. As the coregistration is the second step of the pipeline and the pipeline steps are performed in sequential order, all MRI contrasts were also corrected for bias during the first pipeline step.

The steps that required the use of Statistical Parametric Mapping (SPM) or SPM toolboxes, i.e. Diffeomorphic Anatomical Registration Through Exponentiated Lie Algebra (DARTEL) and Computational Anatomy Toolbox (CAT), were written as MATLAB batch scripts, except for the coregistration step which was adapted from a previously written script using SPM's functions. When other software packages were considered, either the software GUI was used, as it happened with FMRIB Software Library (FSL) for its tools Brain Extraction Tool (BET) and FMRIB's Automated Segmentation Tool (FAST), or the commands were ran using a Unix shell. This was the case for fslmaths' commands, data display using FSLeyes or Freeview and for all FreeSurfer procedures.

All testing and analyses performed in this project were conducted within ThinLinc, a Linux remote desktop server. Whenever scripts were run in MATLAB or from the command line, one of the 5 machines for interactive use would be used. These machines each have two Intel® Xeon® Processors X5670 (2.93 GHz, 6 cores) with 64 GB RAM. As ThinLinc is shared with other users at DRCMR, the computational time of the steps ran in this project was not only dependent on the technical properties of the machines used but also on the amount of processes being ran at the same time in the cluster. This variable was not controlled for and therefore computational times for the different pipeline steps are not described in detail in this dissertation.

A scheme illustrating the different steps of the image processing pipeline and how they are related is presented in **Figure 3.1**. The images are results from the project visualized in FSLeyes and Freeview. The scheme starts from the perspective of one of the patients. The red image borders used in two images allow a better visualization of the images that are used in the following step. The orange borders highlight the individual and group surfaces with the overlaid lesions, the final outcomes of the image processing pipeline.

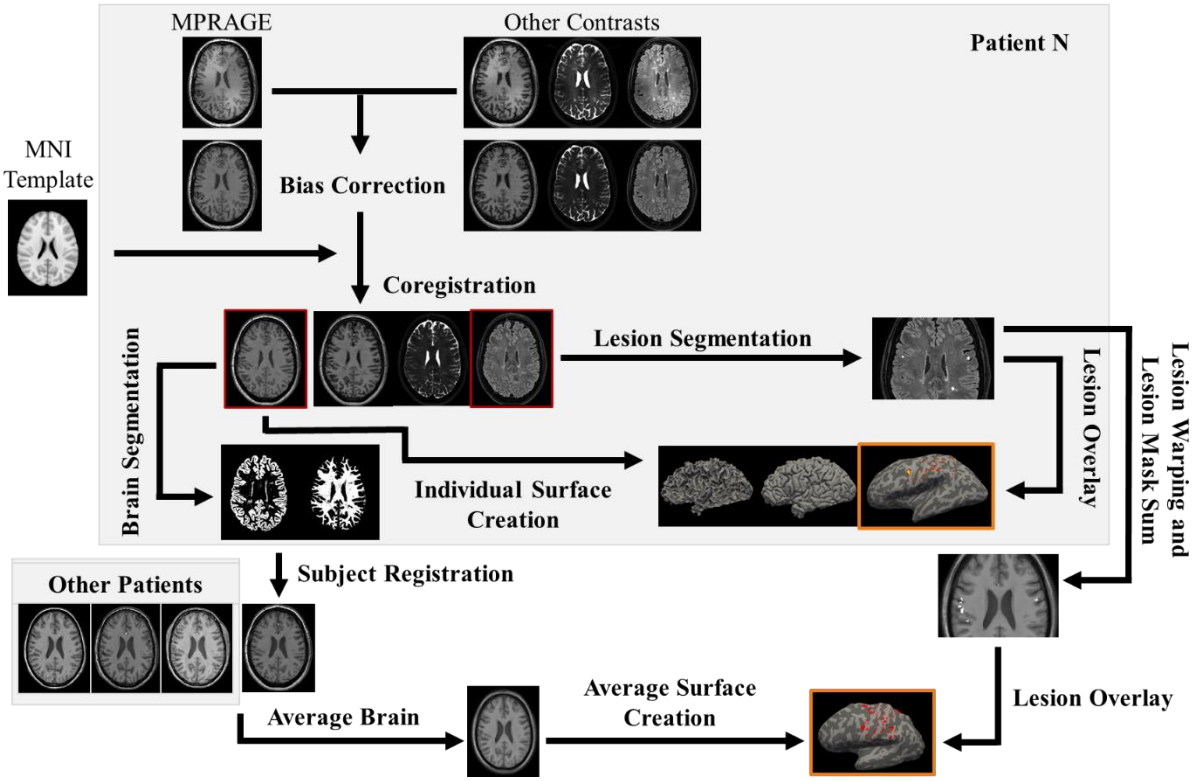

Figure 3.1: Schematic representation of the image processing pipeline starting from the individual data of one of the patients. The coregistered FLAIR and average brain images are used on the scheme to overlay the individual lesion mask from the lesion segmentation and the warped and combined patient lesion mask, respectively. The patient and average surfaces with the overlaid lesions are highlighted in orange.

3.2.1 Bias Correction

Literature pointed SPM as the software package which seems to be least affected by bias at 7 T, showing potential for the correction of bias in various MRI sequences [70],[104].

The bias correction step in SPM is performed within the segmentation module, *Segment*. In one of the studies [104], the SPM parameters for regularization and smoothing, as expressed by the measure full width at half maximum (FWHM), were changed in search for a configuration that led to a minimal root mean square error between the simulated and the estimated bias correction field at 1.5 T, 3 T and 7 T. This configuration is referred to as *enhanced* in contrast with the *default* one. At 7 T, this enhanced parameter configuration consisted of 30-mm for the FWHM and 10^{-2} for the regularization, instead of 60-mm for the FWHM and 10^{-3} for the regularization. In this project, both configurations were considered, and their original names were kept.

As the results from that study were applied to simulated data, besides the visual assessment of the bias corrected volumes, bias fields and segmentation results, a qualitative analysis using histograms was performed to better understand the difference between the enhanced configuration and the default one when using subject data. Whole 3D brain volumes were accounted for in the histograms to allow a more realistic analysis. Furthermore, to provide a better filtering of unwanted intensities and/or noise, brain masks were used to only account for the GM, WM and CSF regions. This was done in MATLAB by adding the individual segmented tissue classes obtained in the *Segment* module using the enhanced configuration and posteriorly multiplying the resulting mask, binarized, with the original, default and enhanced MPRAGE volumes of each participant before acquiring their respective histograms.

After deciding upon the enhanced configuration as the most promising, a MATLAB script was created for this step to automatically and iteratively apply the bias correction to all MRI contrasts of all eighteen participants. A MATLAB batch was used to call SPM without the need for the GUI framework.

3.2.2 Coregistration

Unlike the bias correction step where the decision to use SPM came from literature, for the coregistration step the decision of which software to use came from a group meeting where it was suggested that the approach currently used by the Reader Centre was tested. The Reader Centre is a small group of radiographers at DRCMR that work on the detection of lesions and other findings of interest associated with clinical projects taking place at the Centre. In particular, the group works on the manual segmentation and detection of white matter MS lesions from MS-related projects at 3 T. Before they start the detection of WM lesions, the images go through a coregistration procedure that uses SPM's functions to align the individual scans between each other and with respect to the MNI space by means of rigid body transformations.

As the data for this project comes from a cross-sectional study and all volumes are acquired within the same session, it was agreed that no structural changes would have occurred between the scans and therefore this coregistration could also be done by means of rigid body transformations. The alignment to the MNI space was also considered as it would already allow the volumes to reach a certain level of alignment at this point of the pipeline. The MATLAB script that automatically and iteratively applied the coregistration step to all MRI contrasts of all the participants from this project was adapted from the script used by the Reader Centre. The script was altered to suit the project data and account for the modifications needed to align data of higher resolution. For instance, the coregistration step was divided in three individual coregistration procedures:

1. Alignment of the masked MPRAGE volume to the masked MNI template.
2. Alignment of the unmasked MPRAGE volume to the masked MPRAGE volume.
3. Alignment of the remaining unmasked contrasts to the unmasked MPRAGE.

The first alignment was done between the masked volumes as opposed to the original volumes as aligning the unmasked volumes was resulting in alignment errors. These results can be seen in the **Appendix A** section of this dissertation.

To avoid downsampling the data by using an MNI template of resolution 1-mm or higher, the template of resolution 0.5-mm was used. To account for the inexistence of a masked MNI template brain of resolution 0.5-mm, the 1-mm MNI binary mask was initially used and resliced to the 0.5-mm template using the SPM GUI. After that, the 0.5-mm template and the newly acquired binary mask were multiplied in MATLAB to create a masked MNI template of resolution 0.5-mm. Once acquired, this volume was used for the automatic coregistrations of all eighteen participants.

For the MPRAGE masked brains, using the individual resulting segmented files from the same module that produced the bias corrected files, *Segment*, the volumes regarding WM, GM and CSF of each subject were added, binarized and further multiplied with the bias corrected MPRAGE file to create the masked file. This resulting file was the one who was then coregistered to the MNI mask using SPM's commands *spm_coreg* and *spm_reslice*. An excerpt of the code corresponding to the coregistration step can be seen in the **Appendix B** section of this dissertation.

The same SPM commands and a similar approach were followed for the remaining two alignments. The only difference were the defined moving and fixed files.

3.2.3 Brain Segmentation

The results acquired for the bias correction part of this pipeline already allowed the visualization of the brain segmentation using SPM. These initial positive results led SPM's module *Segment* to be considered for this pipeline step. However, given the coregistration step that followed the initial bias correction, the tissue classes obtained within that first step could not be directly used as they were not in the appropriate space. A similar coregistration procedure could have been applied to the segmented files already acquired. Instead, SPM's *Segment* module was used again. In the GUI framework of SPM, the MPRAGE files for a sample of the project data, bias corrected and coregistered to the MNI space, were added as input files and SPM was run without any changes in the default parameters.

SPM was used to obtain some segmentation results which were then applied to the remaining patient dataset and used in the remaining pipeline steps to acquire preliminary results required for the bigger project. Later, this segmentation step was revisited and two new approaches were tested and compared. The two new approaches were a toolbox from SPM, CAT, that also contains a segmentation module, and the segmentation tool from FSL, FAST.

Initially, CAT's module ran in the respective GUI framework without any implemented changes. A visual inspection of the results signaled a downsampling of the data as well as a registration procedure in-built in the code with regards to the MNI space. This is displayed in the **Appendix C** section of this dissertation for one of the patients. To account for these changes, the batch code was accessed and the voxel size of the normalized images was changed from 1.5-mm to 0.5-mm. Moreover, the WM and GM parameters related to native space were changed so that tissue class results aligned to the original image, that is, without a posterior normalization, were also produced.

Unlike the first two approaches, FAST requires the input volume to be masked before the segmentation step can be ran. More specifically, it requires the use of the tool BET, also a part of the software, for the acquisition of a brain mask. When running BET for the MPRAGE file without any change in the parameters, signs of brain extraction flaws were denoted. To overcome this problem, the *fractional intensity threshold* parameter of 0.50 was altered to understand whether it could improve the final brain mask. Upon testing it with values of 0.25 and 0.75, the value of 0.25 was adopted. These results can also be visualized in the **Appendix D** section of this dissertation.

For the acquisition of the preliminary results for the segmentation, a MATLAB batch script had been created to apply the segmentation method using SPM to the remaining patients. Upon revisiting this step, a new MATLAB batch script was created to perform the segmentation on the remaining patients using CAT.

3.2.3.1 Lesion Segmentation

The detection and segmentation of cortical lesions was performed manually. Due to the lack of approved guidelines for the detection of these lesions at 7 T, guidelines were made amongst the group involved in the bigger project. These guidelines were created after experimenting with different software packages, using different contrasts, doing the detection blindly or not. Time required to perform the segmentation was also considered as a weighting factor.

The lesions were detected and drawn on the axial plane with the possibility of using the other planes for validation. Contrast and zoom could be altered throughout the task and a lesion should include a minimum of 3 voxels and be present in at least 2 contiguous slices. This was consistent with literature [7][94].

Upon experimenting with all contrasts, the FLAIR sequence was chosen for the detection of cortical lesions, with the possibility to use the MPRAGE for confirmation. When using the FLAIR

sequence for the detection of cortical lesions, lesions should appear hyperintense compared to the surrounding normal GM tissue. When confirming the lesions on the MPRAGE they should look hypointense compared to the surrounding tissue. Due to the time-consuming task of manually drawing each lesion, it was agreed that only the lesions occurring in a region of interest which encompassed the sensory and motor cortices would be considered. This region should correspond approximately to the SM1 region.

With regards to software packages, Jim, the software used by the Reader Centre for segmenting MS WM lesions at 3 T, MIPAV, a software pointed several times in literature for the manual segmentation of cortical lesions [6],[7],[94],[99] and FSLeyes were considered. In the end, FSLeyes was the one chosen and all lesions were detected on its interface.

In FSLeyes, the *edit* mode was used for lesion delineation and drawing. Lesions would be spotted and only if visible on all three planes would the axial plane then be zoomed in. Afterwards, the *select* mode would be chosen, allowing voxels to be selected around the borders of the lesion and the possibility to move between slices. This mode also allows the interior of the borders to be automatically selected, an important time saver. Once all voxels have been selected, the brush tool on the left side of the interface allows the drawing of the lesion. Lesion voxels were altered during the delineation and set to specific values. Later, those voxels were identified using a MATLAB script and binary lesion masks for all patients were created.

For the creation of individual binarized lesion masks, the FLAIR volumes with the lesion voxels changed to a manually defined value were identified and set to value 1, whereas all the remaining voxels were changed to 0. As the manual lesion detection task in FSLeyes was performed by a second rater, both masks were combined using MATLAB's logical operation *or*. This was performed under the assumption that findings segmented by only one rater were lesions that had been missed by the other.

A CNR study was performed with preliminary results to validate the choice to use the FLAIR contrast. The analysis was performed to the final data to see if there was consistency with the previous findings and to assess if the final results showed statistical significance.

The CNR analysis was also performed in MATLAB. Initially, the MRI scans and lesion masks of the patients, whose lesions had already been segmented at the time, were loaded. In the lesion mask volumes, an additional step was conducted to assemble the voxels belonging to the same lesion and to label the result as a single lesion. For this, the MATLAB function *bwlabeln* was used with a connectivity parameter chosen of 26. To account for possible drawing lapses only the lesions with a volume bigger than 6 voxels were considered, which aligns with the rule that a lesion should include a minimum of 3 voxels and be present in at least 2 contiguous slices. Structural elements of radius 1 and 2 with spherical shapes were created using the MATLAB command *strel* and later applied to each lesion using the command *imdilate*. The results were subtracted giving rise to a spherical ring around the lesion with a certain separation from the lesion borders to account for any voxels that could be in a region of uncertainty and whose choice to include or not in the lesion drawing was dependent on the lesion drawer. This ring was defined as the neighborhood of the lesion. To ensure that the neighborhood of the lesion was always calculated on the same tissue, in this case GM was the chosen tissue, the ring was multiplied by the GM tissue class obtained in the segmentation step, binarized, before calculating any further parameters of interest.

The contrast parameter in the CNR formula was defined as the difference between the mean signal in the lesion and in the neighborhood for the specific MRI contrast. As the lesion is not always hyperintense compared to the surrounding GM tissue, this difference was made absolute so that all values were positive. The noise parameter was defined as the standard deviation in the lesion

neighborhood [105]. The CNR was calculated four times for each lesion to account for the four types of structural MRI contrasts used in this project. For the CNR calculations, MATLAB commands were used, namely, *mean*, *abs* and *std*. To deal with not-a-number (NaN) voxels present in the volumes which result from the coregistration and reslicing procedure, the 'NaNFLAG' flag in the MATLAB commands for *mean* and *std* commands was changed to 'omitnan' to not influence the results. An excerpt of the code is provided in the **Appendix E** section of this dissertation. To allow a better display and interpretation of these results, boxplots were created. To test if this difference between the FLAIR sequence and the other three contrasts is significant, three two-sample t-tests were performed in MATLAB using the command *ttest2*.

3.2.4 Subject Registration

For the inter-subject registration step of the pipeline, literature pointed in the direction of the DARTEL toolbox from SPM [106]. Its use on 7 T MPRAGE data, the field and contrast of choice in this project, contributed to the decision to use it. Furthermore, by using DARTEL, uniformity in the whole framework was maintained, continuing the pipeline construction from SPM tools and avoiding possibility of incompatibility between different software packages.

To account for the voxels on the borders of the MPRAGE volumes that upon the reslicing procedure in the coregistration step had been changed to NaN, the files were altered so that such voxels were changed to zero before initiating any step in DARTEL. This volume change was done in MATLAB.

DARTEL was initially used to create a template space corresponding to the average of the patients' brains using the segmented volumes acquired in the brain segmentation step using SPM. Later, when the segmentation step was revisited and CAT showed a better segmentation performance, CAT's segmentation files were incorporated into DARTEL to create an alternative average template. This was performed in a MATLAB batch that considered the DARTEL module *Run Dartel (create Templates).*

After the template creation, DARTEL was used again to register the MPRAGE volumes of the patients to the two acquired templates. This is possible due to the individual flow field volumes provided as output from the previous DARTEL step. This image registration procedure using non-linear tools corresponds to the DARTEL module *Create Warped* and was likewise ran in MATLAB for both sets. A schematic representation of the step performed in DARTEL is presented in **Figure 3.2** to illustrate the subject registration procedure. The images presented belong to the project and were acquired in FSLeyes.

To allow the comparison of the performance of DARTEL using the two different sets of input data, from SPM and CAT, the templates created were assessed in more detail, as well as the warped MPRAGE files. Moreover, a coefficient of variation (CV) analysis was performed to understand how the quality of the segmentation impacted the quality of the resulting average templates, and consequently of the registration. The significance of this parameter was tested with Mann-Whitney tests, making use of MATLAB's function *ranksum*.

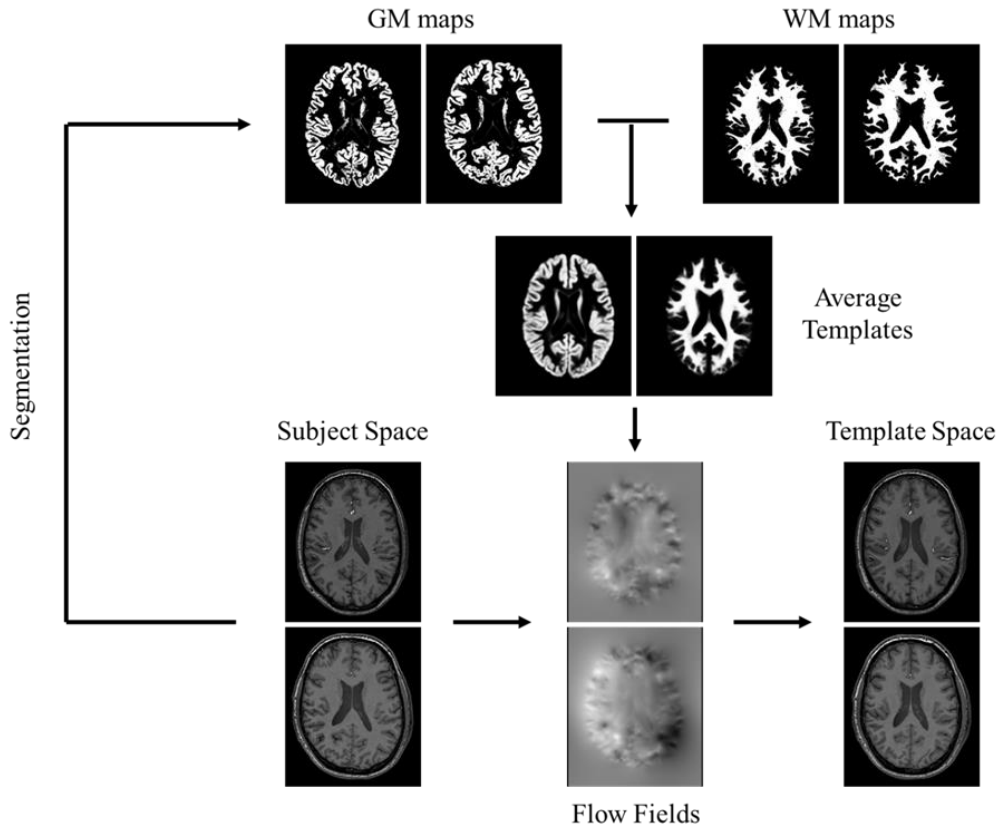

Figure 3.2: Schematic representation of the subject registration step. The MPRAGE segmented tissue maps are used to create average templates. The individual flow fields acquired during the template creation are applied to the individual MPRAGE volumes to register them to the template space. Even though all patients were used in the creation of these templates, the scheme only displays data from two for simplification. The presented tissue maps come from SPM's segmentation procedure.

3.2.5 Surface Creation

In this project and to meet the goals of the bigger project, FreeSurfer was used to create individual brain surfaces for all patients in the dataset as well as a brain surface from the average of the individual brains. This was thought to aid in the visualization of the topography of cortical lesions within the SM1 area.

Brain surfaces are acquired from a command called *recon-all*. To assess the quality of this tool using the project's 7 T data, the command was run for the warped MPRAGE volume of two patients and for an average brain volume acquired from the average of the warped MPRAGE volumes of all patients using the files from the CAT segmentation. To create the average brain volume, fslmaths, one of FSL's command line utilities, was used. In particular, the commands *sum* and *division* were considered.

With regards to running *recon-all* using 7 T data, literature recommended performing bias correction prior to the surface reconstruction [107]. This was already the case so no added steps needed to be integrated. It also recommended using a recent feature more adequate for data below 1-mm in resolution. However, this feature is said to work well with resolutions up to 0.75-mm in resolution. Due to the length of this step with the submillimeter feature, only the average surface went over this process.

To acquire the final individual brain surfaces, *recon-all* was run in parallel for the remaining patients using batch jobs.

To study cortical lesions on an individual and group level, the lesions masks needed to be overlaid on the respective surfaces. Following the approach used at DRCMR for fMRI data, a first command, *bbregister*, was applied to all patients' data to generate a transformation matrix with the information of how to get from the space of the lesions to the volumetric space of the respective patient in FreeSurfer. Secondly, the command *mri_vol2surf* was applied to all lesion masks to, based on the transformation matrix, assign the voxel values to their respective surface vertex, allowing the transition from volume to surface space to be performed to the lesion files. The group lesion mask also went through a similar process. To acquire the group lesion mask, fslmaths' *sum* command was used to acquire the volume of the sum of all individual lesions masks.

The *mri_vol2surf* command was run for all subjects and for the average brain. Moreover, it had to be run twice for each case to cover both hemispheres. When it came to projecting the lesions along the surface normal, defined in the parameter *projfrac*, an average along the normal was considered instead of favoring a particular area of the cortical surface by choosing a value between 0 and 1. The possibility of displaying the maximum along the normal was also not considered so that the projection would be more realistic in displaying the concentration of lesions found along that normal. The visualization of the lesions was performed on the inflated surfaces as they allow a proper visualization of the sulci.

The *mri_vol2surf* command was run for all subjects and for the average brain. Moreover, it had to be run twice for each case to cover both hemispheres. When it came to projecting the lesions along the surface normal for the individual subjects, defined in the parameter *projfrac*, an average along the normal was considered instead of favoring a particular area of the cortical surface by choosing a value between 0 and 1. For the average brain, the maximum along the normal was considered to allow an easier interpretation of the results. The visualization of the lesions was performed on the inflated surfaces as they allow a proper visualization of the sulci.

4 Results

In this chapter, the results obtained for the image processing pipeline are introduced. The results are split into the different steps so they can be easily identified and accessed. The sections are built in sequential and chronological order and follow a similar structure to the one presented in **Chapter 3** with regards to the pipeline steps.

Most of the analyses performed were of visual nature. Therefore, to avoid a numerous number of figures, results had to be simplified, only displaying data from a sample of the dataset, and making use of the different contrasts and anatomical planes. The predominant use of the MPRAGE contrast is related to its use as the reference contrast, going through all pipeline steps. The axial plane is also predominately used for data display due to its role as the plane where cortical lesions were initially identified and afterwards segmented. Despite the simplifications made to avoid an extensive section, the results presented are a carefully selected fraction of the overall results obtained and aim at accurately representing what was commonly found across the different subjects.

During each step, cortical lesions are assessed to ensure that the ability to spot, segment or analyze them is not compromised by the procedures taking place.

4.1 Bias Correction

The results acquired for the bias correction step of this image processing pipeline are presented in this section of the dissertation. Apart from **Figure 4.1**, created in MATLAB, the results are screenshots of volumes visualized in the image viewer FSLeyes.

A histogram analysis was performed across the entire dataset to qualitatively assess and compare the two SPM configurations, enhanced and default, as well as the advantage of performing bias correction. **Figure 4.1** depicts the plotted MPRAGE histograms for four patients and two healthy controls. The black, red and green curves correspond to the uncorrected, corrected with the default configuration and corrected with the enhanced configuration volumes, respectively. The remaining histograms can be found in the **Appendix F** section of this dissertation.

Apart from one patient whose histograms can be found in the **Appendix F**, two peaks are always visible on the corrected volumes which correspond to the tissue classes GM and WM. A third region corresponding to the CSF can also be distinguished. In the MPRAGE contrast the CSF class appears darker, therefore corresponding to the lowest voxel intensity peak/region, followed by GM and WM. When looking at the regions corresponding to GM and WM, the histograms show that, for the enhanced volume histogram, the GM and WM peaks are steeper, suggestive of a clearer differentiation between the two classes.

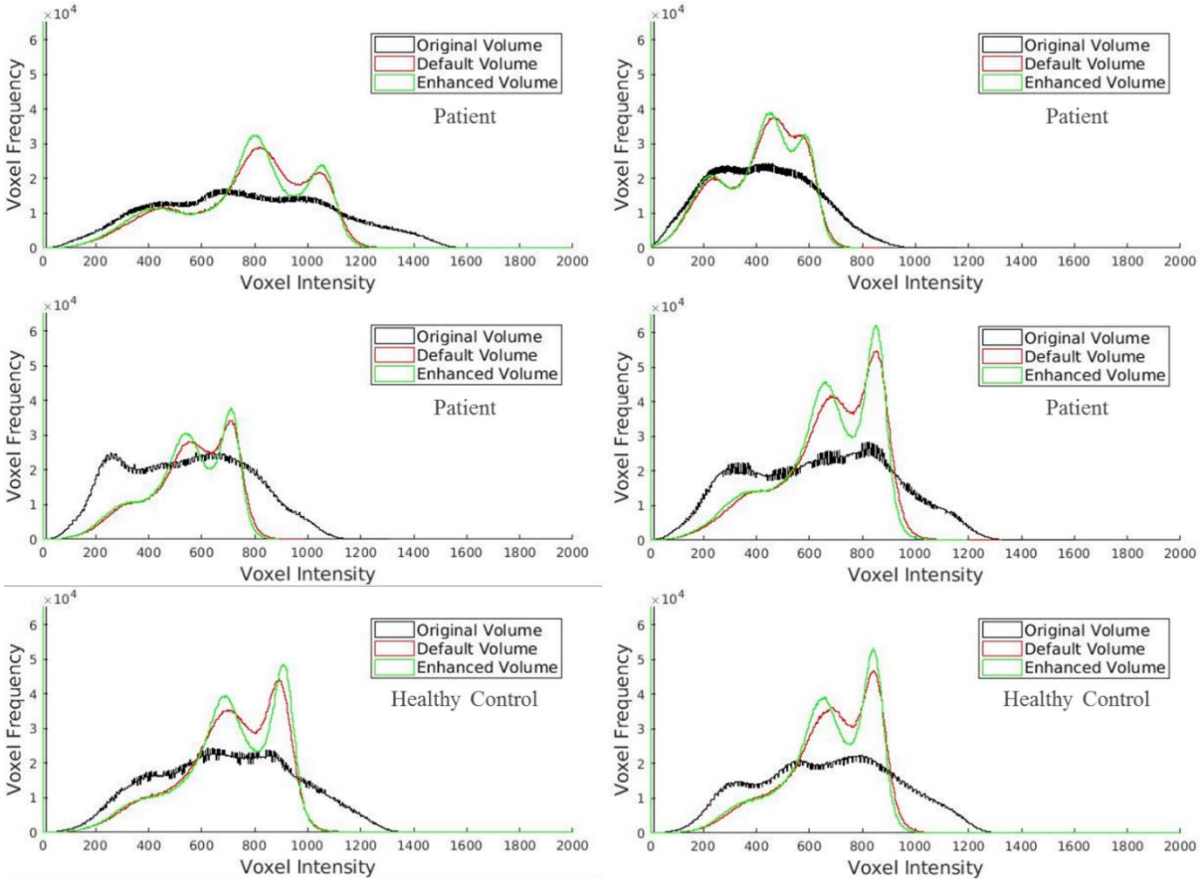

Figure 4.1: Histograms showing the voxel intensity distribution of WM, GM and CSF for a sample of the dataset for the original and bias corrected volumes using SPM's default and enhanced parameters. Despite the better depiction of the GM and WM peaks from the correction of bias, the steepness of the enhanced volume histograms is suggestive of a better differentiation of the two classes.

Intersubject variability can also be seen by the differences between the plots. This is a result of the qualitative nature of this analysis, of the MPRAGE sequence and of the inherent differences between the subjects which stem from age differences, as well as differences in disease progression and manifestation, in the case of the patients. Still, the histograms from the healthy controls point at a higher peak for WM, compared to the GM peak. In the patient data this is not always found. The amount of white matter lesions, a marker of MS, which appear darker on the MPRAGE images, should contribute to the increase in the GM peak and consequently a decrease in the WM peak in some patients.

Bias and its correction can also be assessed visually by displaying the original and corrected volumes. The segmentation results and the bias fields can also aid in the visual analysis. **Figure 4.2** allows this visual analysis to be done by presenting data from a patient and a healthy control using their FLAIR and MPRAGE images, respectively.

A visual assessment can be easily done between the original and the corrected images. Both cases show clear regions where the original MRI signal is more intense and where it is weaker leading to differences in the image intensities. This is seen in the lateral sides of the head, for the axial cut, and in the cerebellum, for the sagittal cut, regions where the signal is poorer. For the comparison between the images using different SPM parameters, the visualization of the bias fields and segmentation results allows an easier perception of the differences. Even then, the sagittal cut images already highlight a better correction of bias using the enhanced parameters, particularly in the cerebellum, which led to a better segmentation of this structure.

The bias fields suggest more focality in the delineation of bias in the images for the enhanced parameters and as a result, the segmentation of GM is improved. This is seen in the segmentation images by the higher predominance of high probability tissue values and a better differentiation between the tissue classes, if it assumed that voxels with a value below 0.5 are more likely to belong to WM in the given examples.

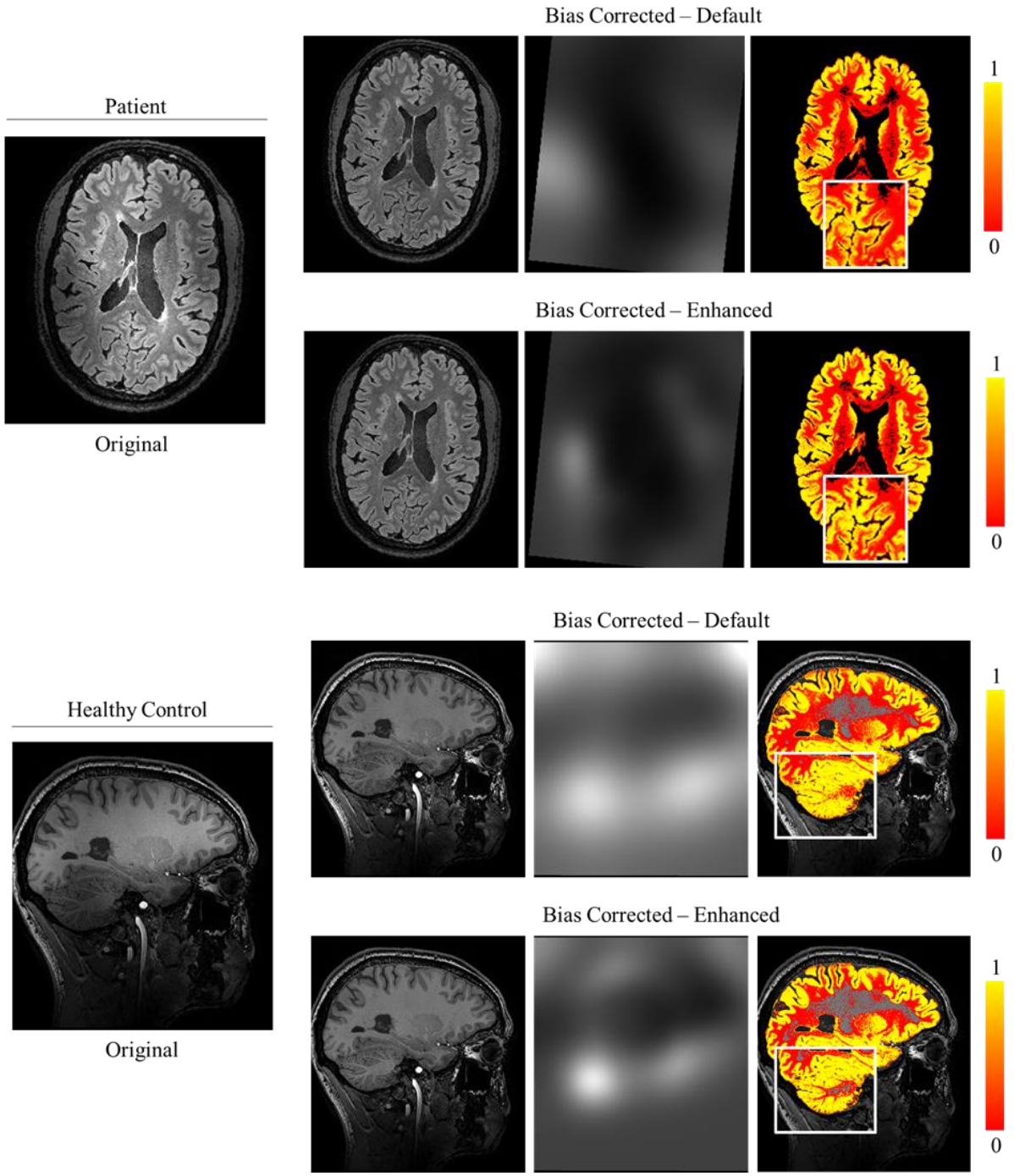

Figure 4.2: FLAIR and MPRAGE cuts of a patient and a healthy control, respectively, showing the differences in the bias correction using SPM's default and enhanced parameters. The bias fields and GM probability maps are included. As a result of a more localized depiction and consequently correction of bias, a better segmentation of the cortex and cortical structures results.

The histograms and visual assessments led the enhanced SPM configuration to be chosen for the project pipeline. Before advancing to the following pipeline step, the patient data was reevaluated for confirmation that the ability to detect and consequently segment cortical lesions would not be compromised by the correction of the images for bias. Some of the results found across the different MRI modalities for several patients are presented in **Figure 4.3**. All screenshots are taken from the axial plane as it is the one where lesions are detected and therefore the main plane of interest when looking at cortical lesions.

As depicted, some contrasts, i.e. the MPRAGE and T1w, show lesions as hypointensities compared to the surrounding tissue, whereas other contrasts, i.e. FLAIR and T2w-TSE, show lesions as hyperintensities. Depending on where in the cortex the lesion is found and how much bias exists in the original images, the bias corrected image will display the lesion and the area around it as brighter or darker, compared to the uncorrected image. The different examples reject the assumption that lesions lose their integrity after the image correction and can no longer be detected. Moreover, the contrast relation between the lesion with regards to the surrounding tissue, seems to be preserved.

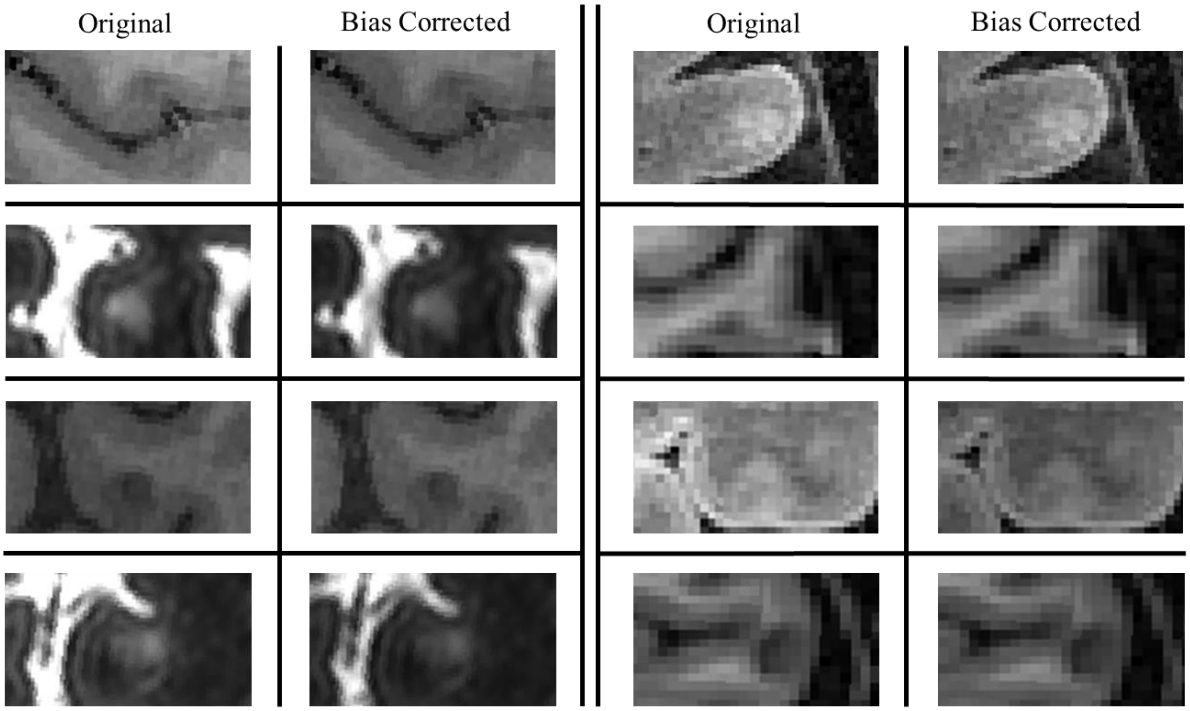

Figure 4.3: Axial cuts displaying cortical lesions before and after bias correction across the patient dataset. Despite the intensity correction, the integrity of the lesions is preserved and their contrast, in relation to the surrounding tissue, is maintained.

4.2 Coregistration

The results acquired for the coregistration step of this image processing pipeline are presented in this section of the dissertation. As explained in the Methodology section, the coregistration step incorporates three separate coregistration procedures which were thought to allow a proper alignment of the structural volumes belonging to each participant. They also allow an alignment of all the data to the MNI space of resolution 0.5-mm. The screenshots of the MRI scans were acquired in FSLeyes.

Figure 4.4 shows the registration of the masked MPRAGE volumes to the masked MNI template, the fixed volume, for a patient and a healthy control as a result of the first alignment. This figure shows the differences in brain size and morphology between the subjects' brains and the template that remain after the alignment. They are a result of the absence of non-linear transformations in this registration aligned with the inherent differences between the fixed and moving images. The still existent differences in alignment after coregistration are better seen with reference to the green axis, particularly in the cerebellum. In the MNI template, this structure is well aligned to the horizontal axis, but the same is not found on the subjects' images. This can also be seen by the inadequate alignment of the corpus callosum in the patient example. The misalignment on the healthy control is not as easily depicted due to the presence of a flow artifact.

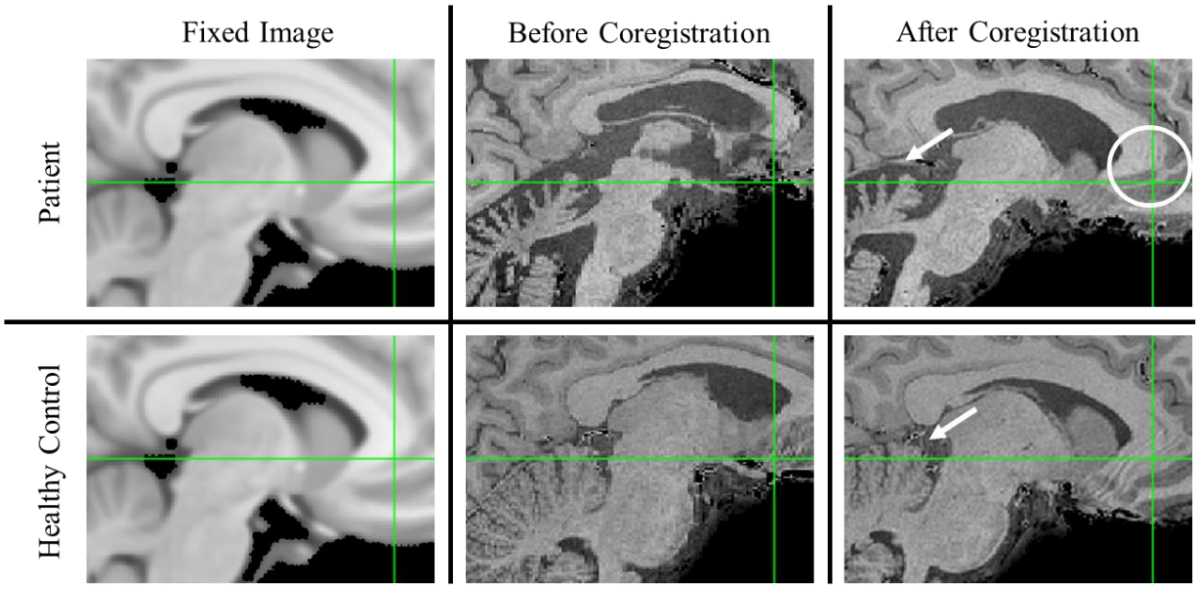

Figure 4.4: Brain sections of a patient and a healthy control displaying the result of the alignment between the subjects' masked MPRAGE images and the masked MNI template, the fixed image. Due to the absence of non-linear registration tools, the alignment of structures with reference to the fixed image is present but individual morphological differences are responsible for the misalignment that prevails after the coregistration.

Figure 4.5 follows a similar structure to **Figure 4.4** and displays the registration of the unmasked MPRAGE volumes to the corresponding masked MPRAGE volumes, the fixed images, for a patient and a healthy control as a result of the second alignment. Once again, the registration is made by use of rigid body transformations only, but because the fixed and moving volumes are from the same subject, a good alignment between the brain structures is expected. The fixation of the green axis on a point on the corpus callosum for the two subjects shows a very accurate alignment of this structure, for both cases.

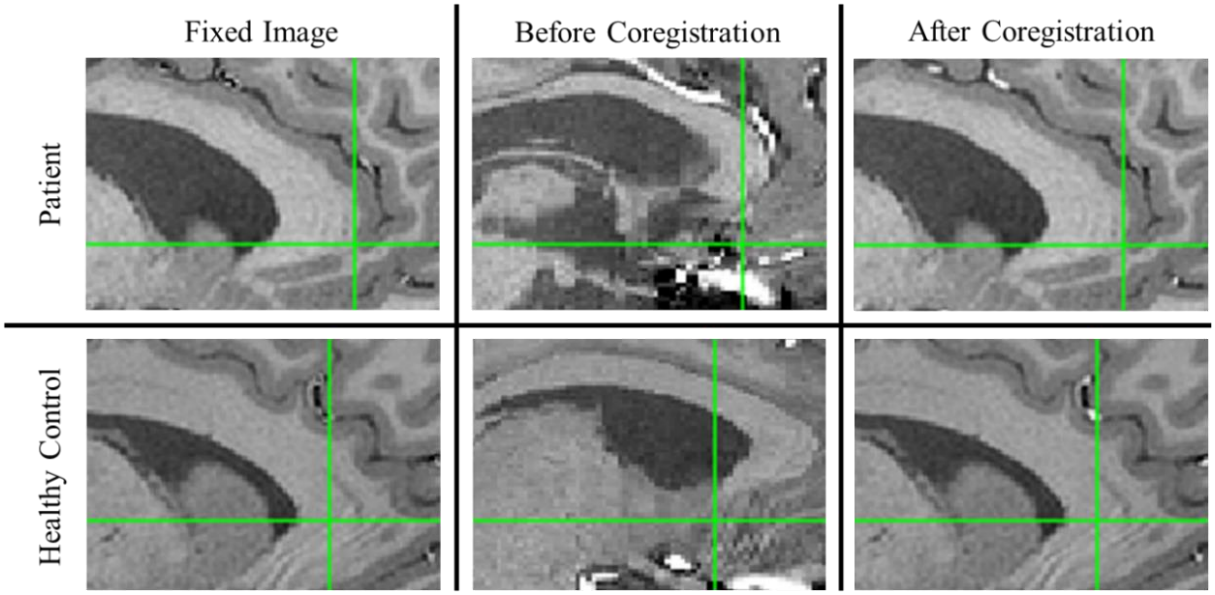

Figure 4.5: Brain sections of a patient and a healthy control displaying the result of the alignment between the subjects' unmasked MPRAGE images and their respective masked MPRAGE images, the fixed images. The green axis fixed on a point on the corpus callosum depicts the clear alignment of this structure after the coregistration, present for both subjects.

Figure 4.6 illustrates the result of the final coregistration procedure, that is, the result of the coregistration step in the alignment of the different individual MRI contrasts for a patient and a healthy control. For the representation of this part, results are shown before and after the coregistration step to not only highlight the alignment in the end but also the original misalignment between MRI contrasts as a result of motion between scans.

By overlaying the moving image on top of the fixed MPRAGE volume, it is possible to notice the misalignment by assessing areas of discontinuity. The arrows were added to the images before the coregistration to draw attention to specific anatomical regions where an original misalignment can be seen and where it no longer is present after the coregistration. For instance, on the coronal section, the misalignment is present in the sulcus delineation and in the superior cortical border. On the sagittal section, there is a visible misalignment in the skull edge, nose region and corpus callosum. The coregistration shows a successful alignment of these regions between contrasts.

As the contrasts' alignment is the third alignment performed, the alignment to the MNI template has already occurred and should also be noticeable in these results. This is particularly clear in the sagittal section by the change in the position of the head in both contrasts after the coregistration procedure. The final orientation of the corpus callosum should be consistent with the alignment of the same structure shown in **Figure 4.4**.

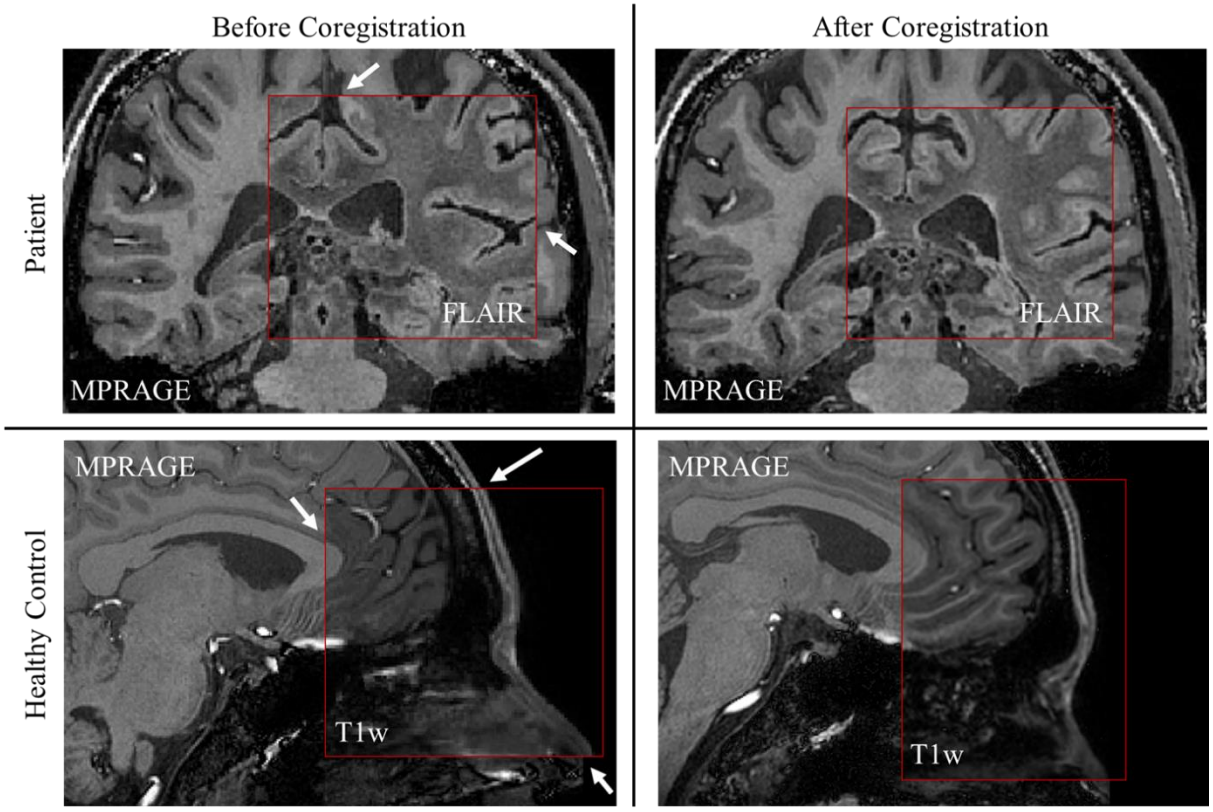

Figure 4.6: Brain sections of a patient and a healthy control displaying the quality of the contrasts' alignment. The arrows point at the regions where a clear misalignment of structures is depicted before the coregistration procedure and where it no longer is present after.

The quality of the coregistration can also be observed by assessing the lesions before and after the coregistration. If the alignment is correct, it should be possible to shift between contrasts during the lesion segmentation task to confirm whether a finding of interest is a lesion. **Figure 4.7** shows an example of a lesion and how it is displayed in all MRI contrasts before and after applying the coregistration. The green axis was used to fix a voxel on the lesion border and display the level of misalignment between the contrast before the coregistration. After the coregistration it is no longer present. **Figure 4.8** displays other examples of the successful alignment of cortical lesions between contrasts.

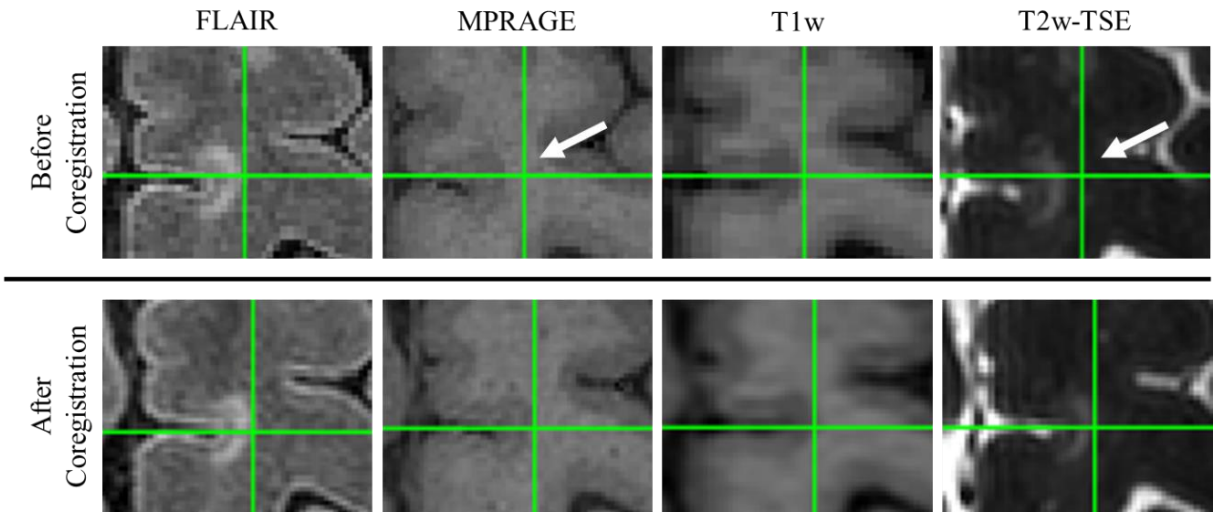

Figure 4.7: Axial cuts displaying a patient's subpial lesion in the different MRI contrasts before and after the coregistration. The fixation of the axis on a lesion border allows the display of the original misalignment, particularly clear on the MPRAGE and T2w-TSE images, and that is no longer present after the coregistration.

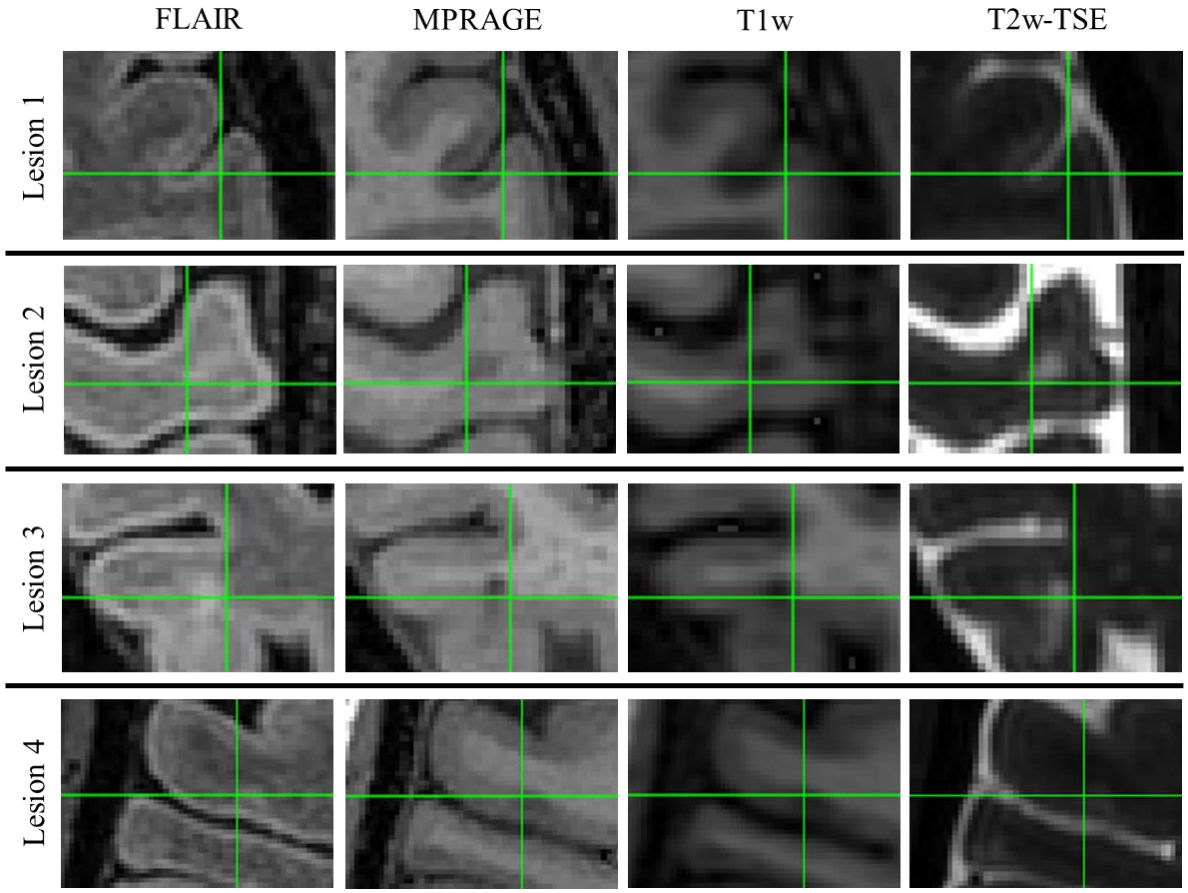

Figure 4.8: Axial cuts displaying four different lesions as seen by the different MRI contrasts after the coregistration. The alignment between the different contrasts should be present and is confirmed by the green axis fixed on a point on the lesion borders.

4.3 Brain Segmentation

The results acquired for the segmentation step of this image processing pipeline are presented in this section of the dissertation. For the brain segmentation, three different approaches were tested: the regular 'Segment' module from SPM, the segmentation method incorporated in the SPM toolbox, CAT, and the segmentation approach from FSL, FAST. To avoid a numerous number of figures this analysis displays the results for one of the patients but the results were consistent across the tested subjects.

To allow a better visual comparison between the software packages, the resulting grey matter probability maps were displayed in FSLeyes and changed to a red-yellow color range to simplify the analysis. These results are presented in **Figure 4.9** for one of the patients in the dataset in an axial cut. The white matter probability maps are thought to add redundancy to this analysis, as they should have an inverse behavior of the grey matter maps, when looking at the boundaries between GM and WM. For this reason, they were not included in the main text of this dissertation but can still be found in the **Appendix G** section of this dissertation.

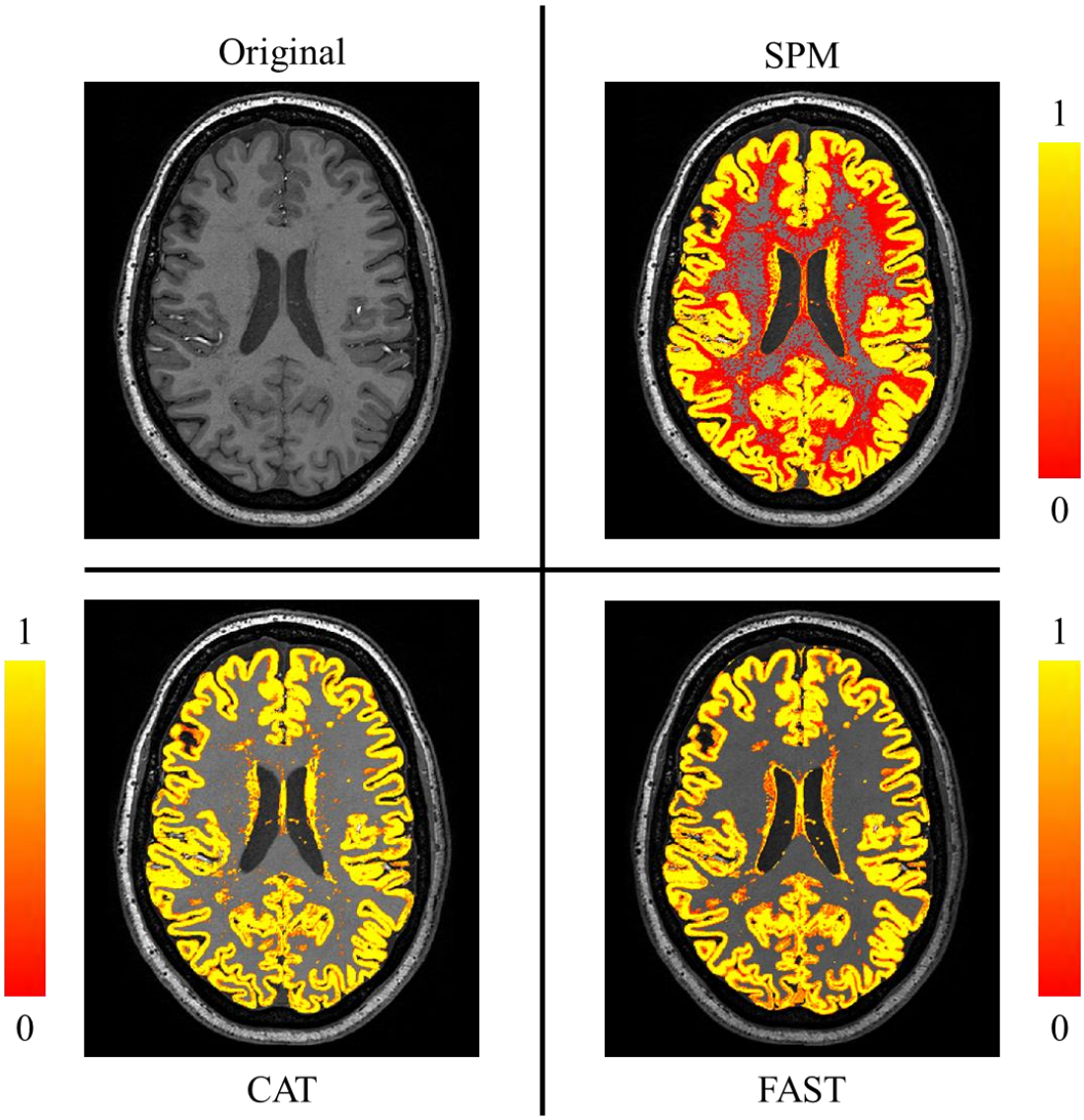

Figure 4.9: Axial cuts of the GM probability maps acquired from the three tested segmentation approaches. The predominance of voxels with low tissue probability in WM in the SPM image suggests a poorer segmentation performance using this approach.

From this first assessment, SPM showed a weaker performance, failing to distinguish GM and WM voxels found deep within WM. This is seen by the low but still existent probabilities given to voxels in WM, which are not as eminent in CAT or FAST.

A more detailed analysis of the three approaches was conducted to support or reject this first finding. For this second assessment, the results focused on two variables: certainty of the cortex voxels and accuracy in the delineation of the cortex.

Figure 4.10 looks at the former, by displaying for a zoomed area of an MPRAGE slice the grey matter maps with different threshold levels: 0.25, 0.50, 0.75 and 0.99. By increasing the threshold level more certainty is required and therefore a filtering of the data results. When setting the threshold to an extreme value of 0.99, CAT clearly outperforms the other approaches. SPM has a considerable decay in the density of voxels that are under that condition whereas FAST continues to choose voxels that fall outside GM. An arrow was drawn to highlight the region where FAST fails, even at a threshold of 0.99.

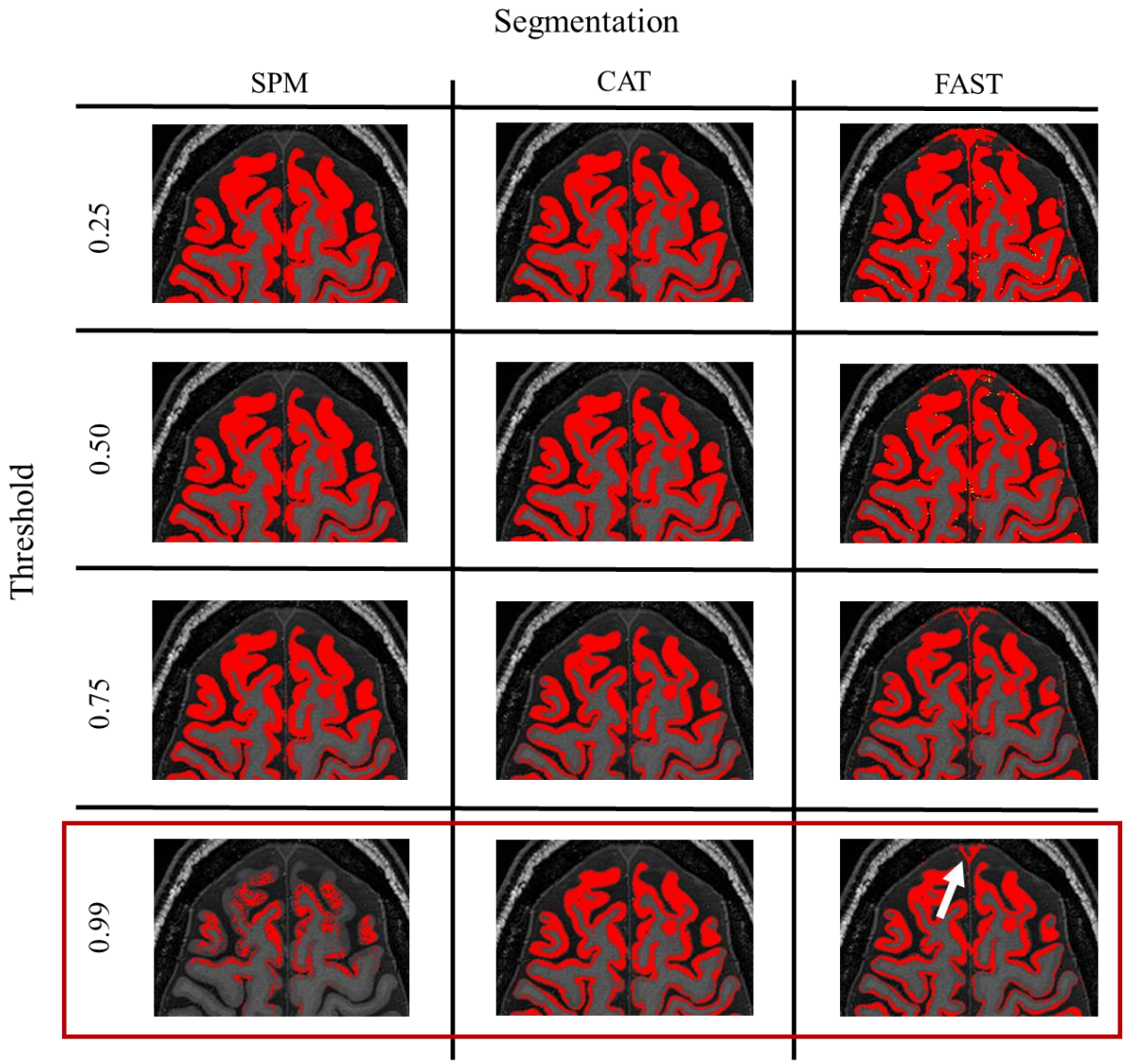

Figure 4.10: Axial sections displaying the GM binary masks for the three segmentation approaches using multiple threshold values. For a voxel certainty of 0.99, it becomes clear that CAT outperforms the other two approaches, displaying more voxel density than SPM and avoiding selecting voxels outside the cortex as happened with FAST, depicted with an arrow.

In **Figure 4.11**, the accuracy in the delineation of the cortex for the different approaches is explored. On a zoomed area of the brain, the different maps were overlaid on the MPRAGE image with a similar threshold value, in this case of 0.5, to allow a better discrimination of the maps and the actual grey matter. A level of opacity was defined but as it is not quantifiable in FSLeyes, its value is omitted from this description. Nevertheless, care was taken to ensure that the opacity was approximately the same for all maps.

Due to the poor contrast between WM and GM in the central sulcus in the original MPRAGE image, all approaches failed to accurately delineate the cortex in that region. Of the three, CAT still managed to pick more GM voxels than the other two approaches. Once again, CAT seems to outperform SPM and FAST. SPM tends to overestimate the class values seen in the boundary regions between GM and WS, whereas FAST shows difficulty in recognizing and excluding voxels outside GM from the resulting maps, which leads to unreliability in the quality of the segmentation.

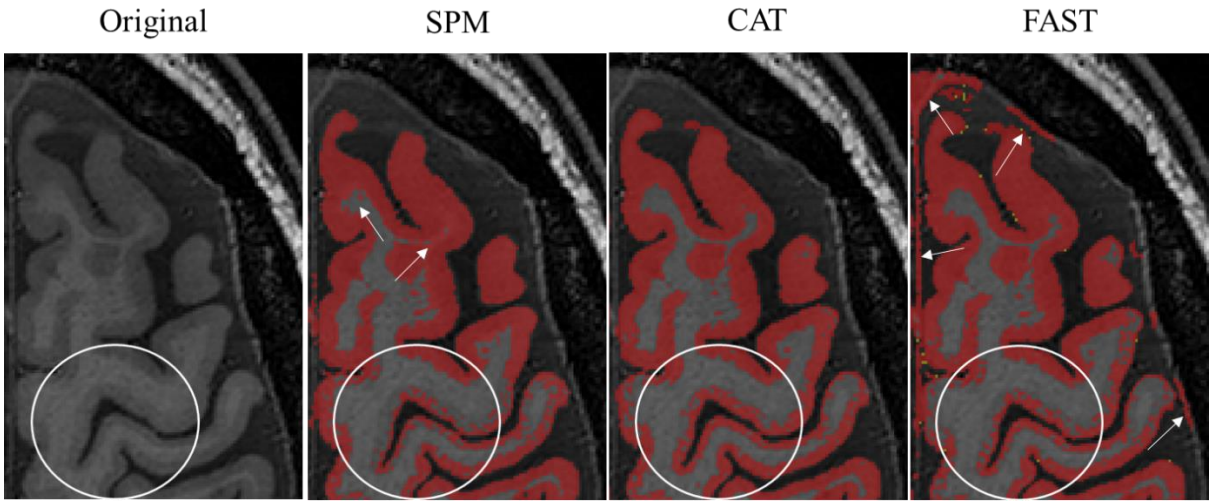

Figure 4.11: Axial sections displaying the GM probability maps for the three segmentation approaches overlaid on the original image. The poor contrast between WM and GM in the central sulcus, highlighted with a circle, impacted the quality of all segmentations. Still, CAT continues to show a better performance overall. SPM tends to overestimate the GM tissue values, whereas FAST shows a tendency to segment and classify voxels outside the cortex as GM.

4.3.1 Lesion Segmentation

The detection and segmentation of lesions was performed manually. As mentioned in **Chapter 3**, this was done with FSLeyes using the FLAIR image for drawing and the MPRAGE for confirmation. The axial plane was the anatomical plane used for drawing the lesions.

To validate the choice of using the FLAIR sequence to perform the detection and segmentation task, a CNR analysis was performed. The lesion neighborhood was created as a spherical ring around the lesion created with the MATLAB tools *strel* and *imdilate*. As previously mentioned, the ring corresponds to the difference between two spheres around the lesion of radius 1 and 2 pixels. The distance between the lesion border and the interior border of the ring aims to account for a region of uncertainty. **Figure 4.12** visually displays what was done for one of the lesions.

Figure 4.12a displays the lesion as spotted on the axial plane of the FLAIR contrast. The same cut seen on the MPRAGE, **Figure 4.12b**, allowed the confirmation of the lesion as cortical and the better visualization of the cortical borders. In **Figure 4.12c**, the MPRAGE is displayed with the lesion mask voxels colored in red. The voxels that belong to the ring created around the lesion are displayed in blue.

Figure 4.12d displays similar results to the previous figure but the ring has been altered so as to only account for the voxels within the GM class. This altered region corresponds to the neighborhood of the lesion, used in the calculations of the CNR parameter. The four figures were obtained in MATLAB.

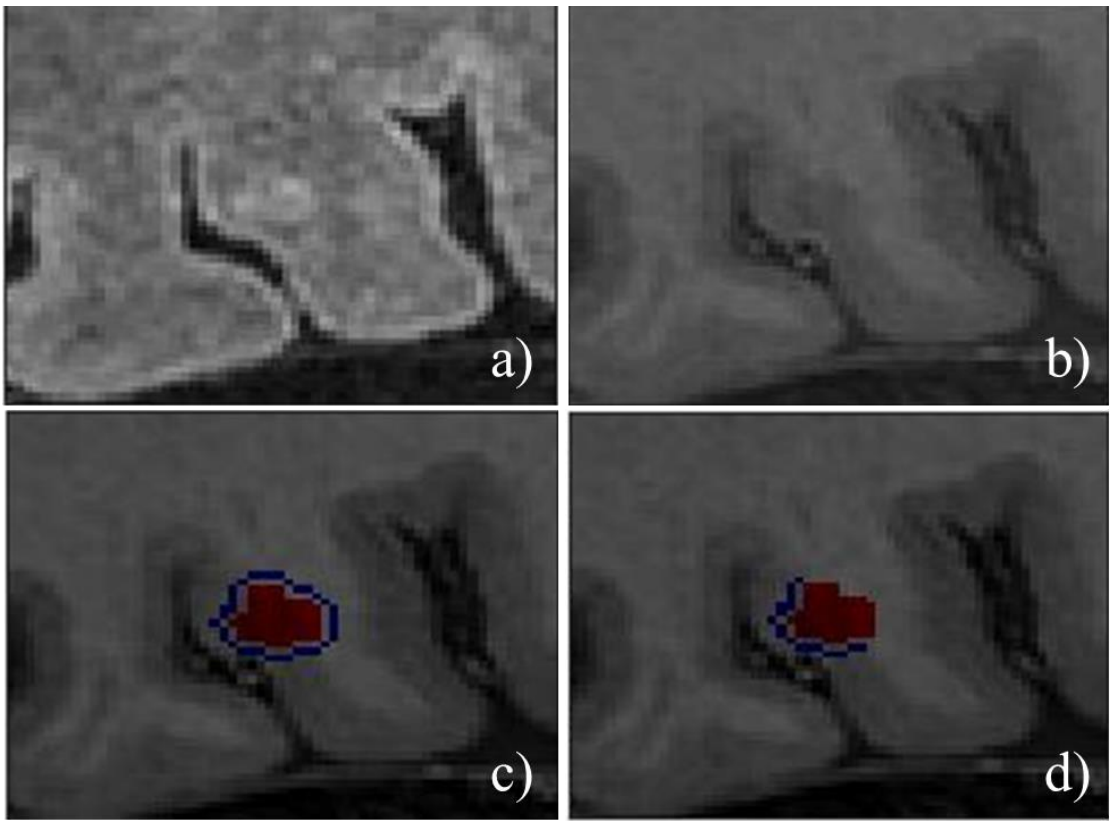

Figure 4.12: Visual display of a lesion as spotted in the axial plane on the FLAIR contrast (a) and confirmed on the MPRAGE (b). (c) depicts on the MPRAGE the lesion segmentation, in red, and the ring created around the lesion, in blue. In (d) the ring has been altered to only include the voxels within GM, the neighborhood of the cortical lesion.

The CNR parameter was calculated twice. The first time it was applied to data from four patients whose lesions had already been detected and segmented at the time. When using the entire patient data, the CNR was calculated for a total of 253 lesions and their respective values, for each contrast, were gathered in boxplots that can be seen in **Figure 4.13**.

The boxplots suggest higher CNR values using the FLAIR contrast. This is seen by the discrepancy of most measures, i.e. the minimum, median or the quartile values, in the FLAIR boxplot compared to the others. To test if the difference between the FLAIR sequence and the other three contrasts was significant, three two-sample t-tests were performed. All tests allowed the rejection of the null hypothesis corresponding to the equality of the mean values with a statistical significance of 0.001, added to the plots with the respective label. The p-values for the three tests were 4.345e-35, 2.092e-34 and 9.827e-23 for the comparison between the FLAIR and the MPRAGE, T1w and T2w contrasts, respectively. The figure was acquired in MATLAB.

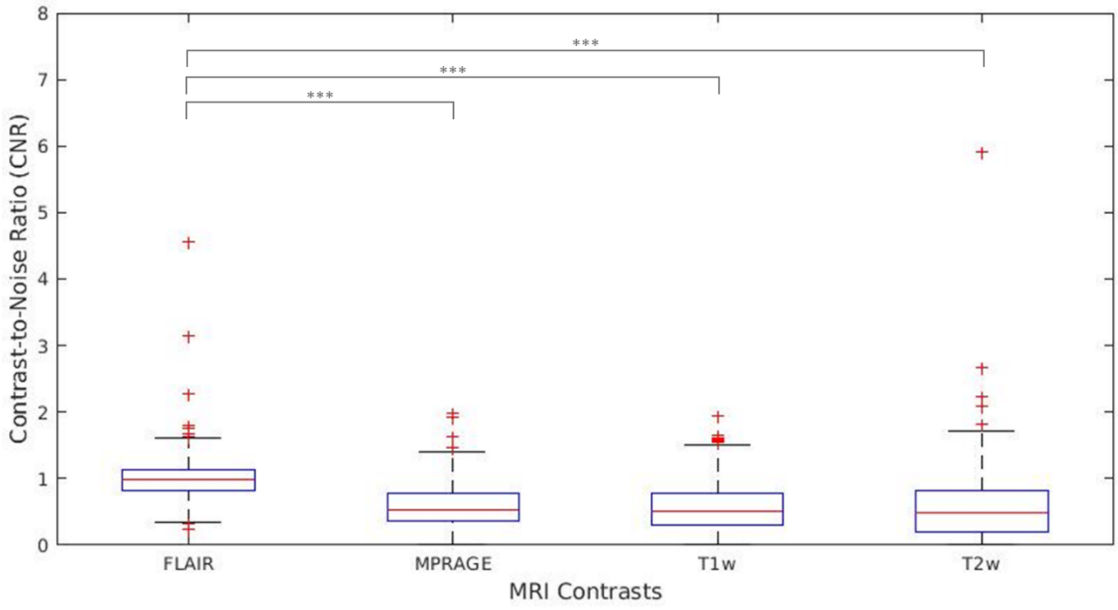

Figure 4.13: Boxplots of the distribution of the CNR parameter across the 253 lesions in the dataset for the different MRI contrasts.

4.4 Subject Registration

The results of the inter-subject alignment, an important step in group analysis, are presented in this section of the dissertation. For this step, the only approach tested was DARTEL. However, two sets of data were used in the creation of the average templates to be used in the registration procedure: the segmented files from SPM and the segmented files from CAT. The former had been used to acquire preliminary results and the latter was later added as an attempt to optimize the pipeline. Therefore, these results will aim at assessing the performance of DARTEL and understanding how the segmentation step, prior to this registration, impacts the quality of the results. The screenshots of the MRI scans were acquired in FSLeyes.

Figure 4.14 depicts the quality of the average GM and WM templates created using the segmented files from SPM and CAT. Both tissue templates using CAT's volumes show an improvement in the level of detail. This is reflected in a better delineation of the tissues with a lower smoothing effect.

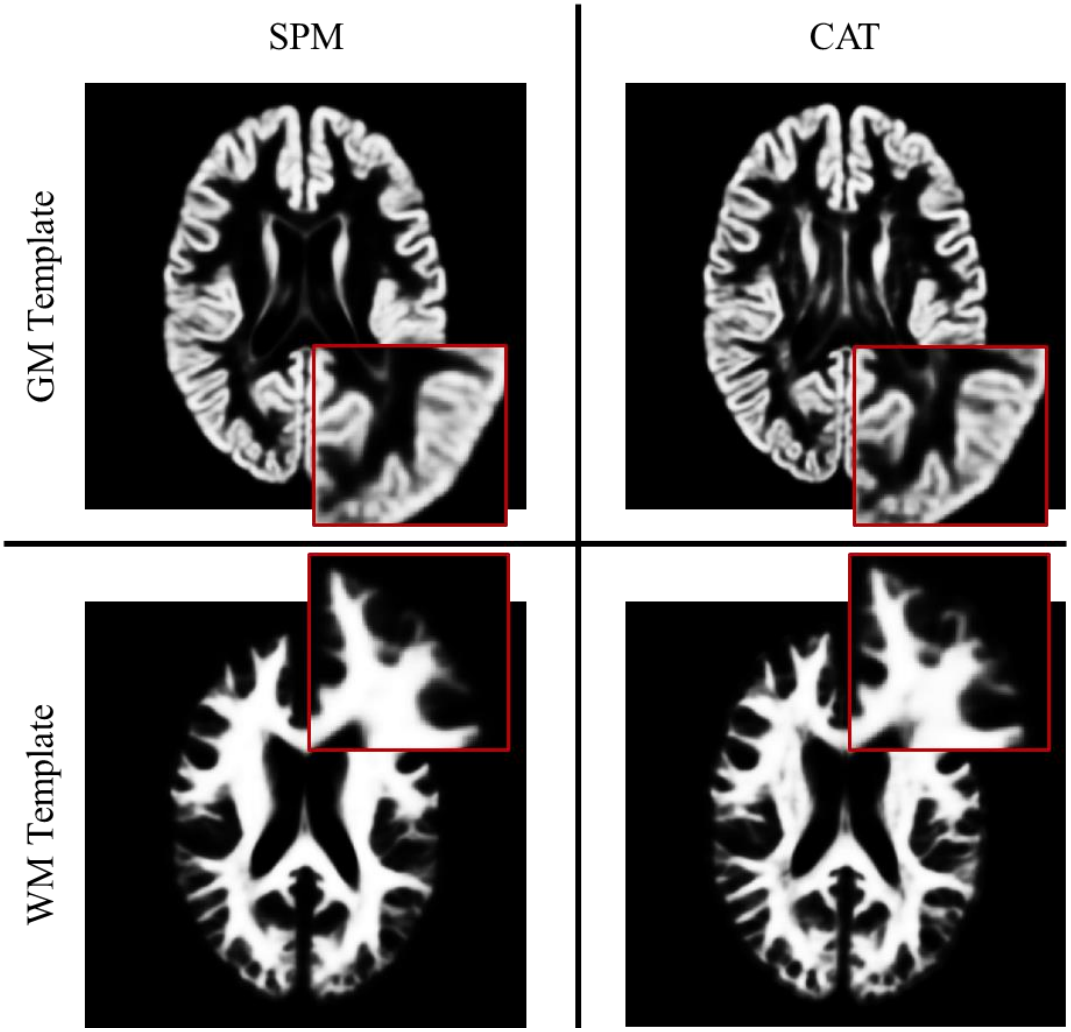

Figure 4.14: Axial cuts displaying the average DARTEL templates for GM and WM created from patients' segmented volumes using SPM and CAT. To highlight the differences in the templates and the better performance using CAT's volumes, enlarged cuts of the images were added.

To understand whether the differences in the templates could be explained by a stronger dispersion of voxel values in the segmented tissue classes using SPM, the coefficient of variance parameter was calculated for the tissue classes of all twelve patients and organized in boxplots. Those boxplots can be seen in **Figure 4.15**.

The boxplots for GM and WM using the segmented volumes from CAT occupy lower CV values and show a smallest distribution of the values across the patient dataset compared to those from SPM. If this parameter measures the degree of dispersion of values around the mean, higher CV values for the SPM segmentation indicate a higher dispersion of the tissue voxel values, or probabilities, compared to CAT. The longer whiskers are suggestive of more inconsistency in the results which appear to be more influenced by the patients' data.

The significance of these measures was assessed with Mann-Whitney tests which compared the medians of the CV parameter for the GM and WM classes for both segmentations. Both tests allowed the rejection of the null hypothesis of the equality in the median values with a significance value of 0.001, added to the plots with the respective label. A p-value of 3.659e-05 was obtained for both tests.

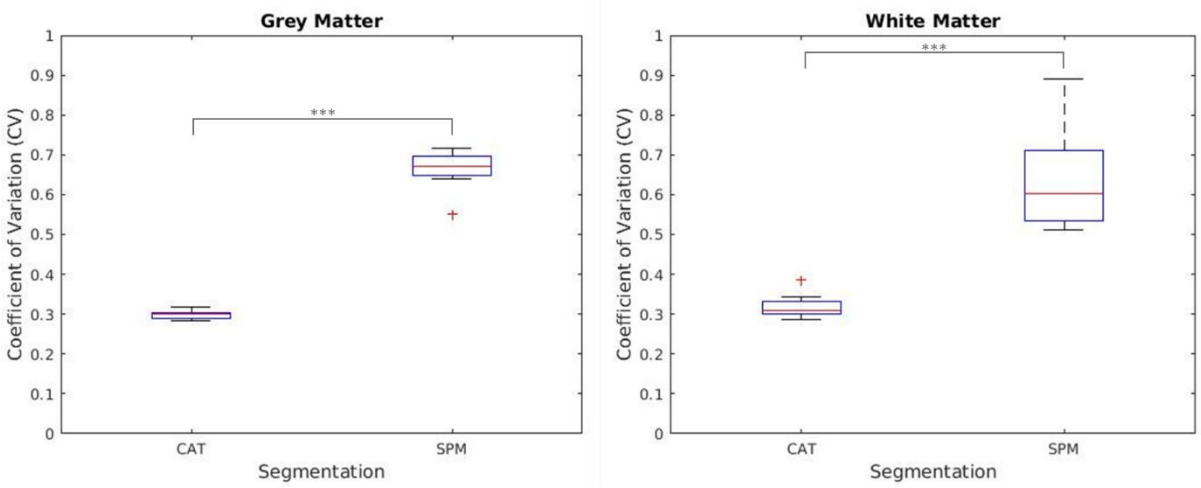

Figure 4.15: Boxplots of the distribution of the CV measure in the tissue classes across the patient data for the two segmentation approaches, CAT and SPM.

When assessing the quality of the DARTEL registration, **Figure 4.16** depicts the result of the registration of a patient's warped MPRAGE volume to the respective template space. In this case, the putamen was chosen as the fixed point of reference and the green axis allows the visualization of the good alignment of the structure when comparing the templates and the warped volumes. This alignment is present in both segmentation approaches, i.e. CAT and SPM, showing good overall performance of both approaches.

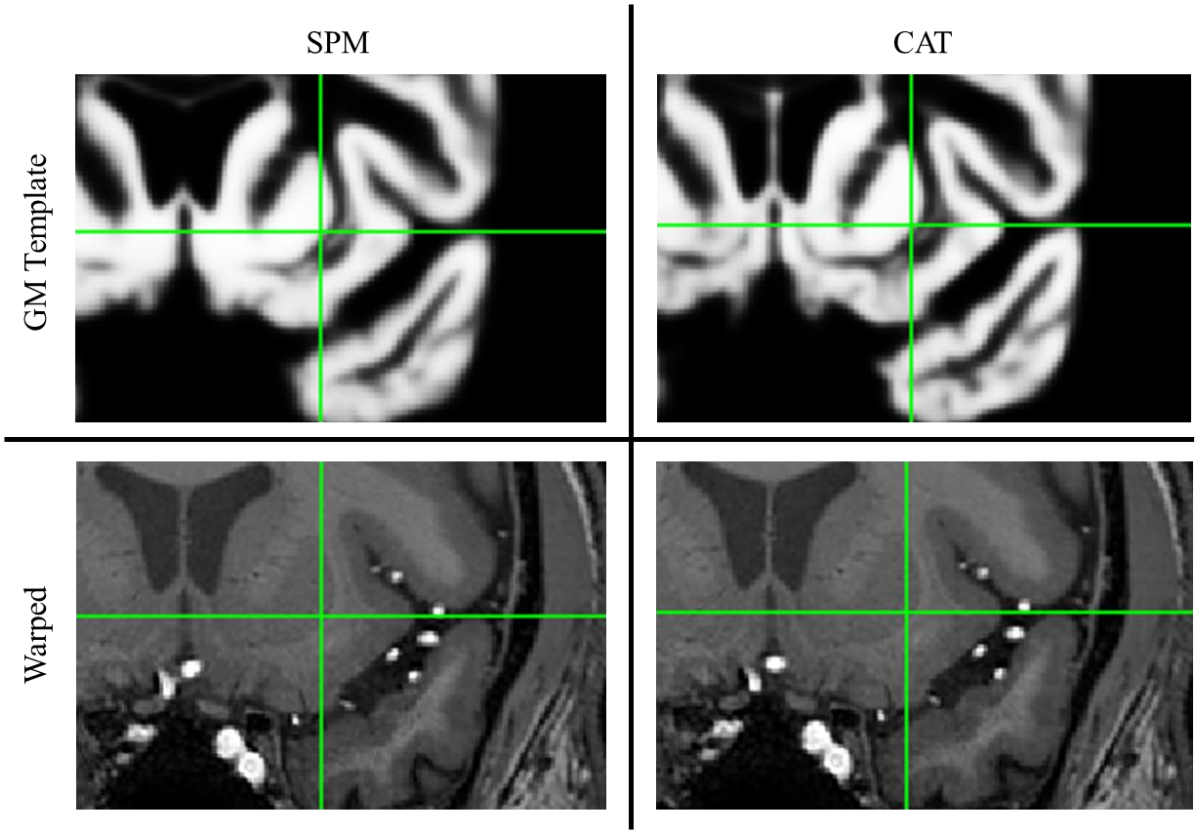

Figure 4.16: Coronal section displaying a good alignment of the warped MPRAGE volumes of a patient to the respective GM template, present for both segmentation approaches. The alignment is fixed on the putamen.

The alignment between patients was assessed by visual comparison of the warped MPRAGE volumes of the youngest and the oldest patients in the dataset, as suggested by literature [78]. This is believed to be the most extreme scenario, as there is a higher possibility that the combination of factors that lead to intersubject variability will be stronger here. This is depicted in **Figure 4.17**. When fixing a point on the cerebellum, a complicated area highly affected by bias at 7 T, the comparison of the alignment between the two patients shows that while there is a good alignment of the structures when using the segmentation results from CAT, SPM leads to a poorer alignment of the structure which could compromise further pipeline steps. It is noticeable in both approaches that the visible cortex is not identical between the two patients, showing that although this registration procedure, particularly using CAT's segmented files, does a good job at aligning the brain structures and overall morphology, individual differences can remain, particularly when going to more external brain regions, such as the cortical borders.

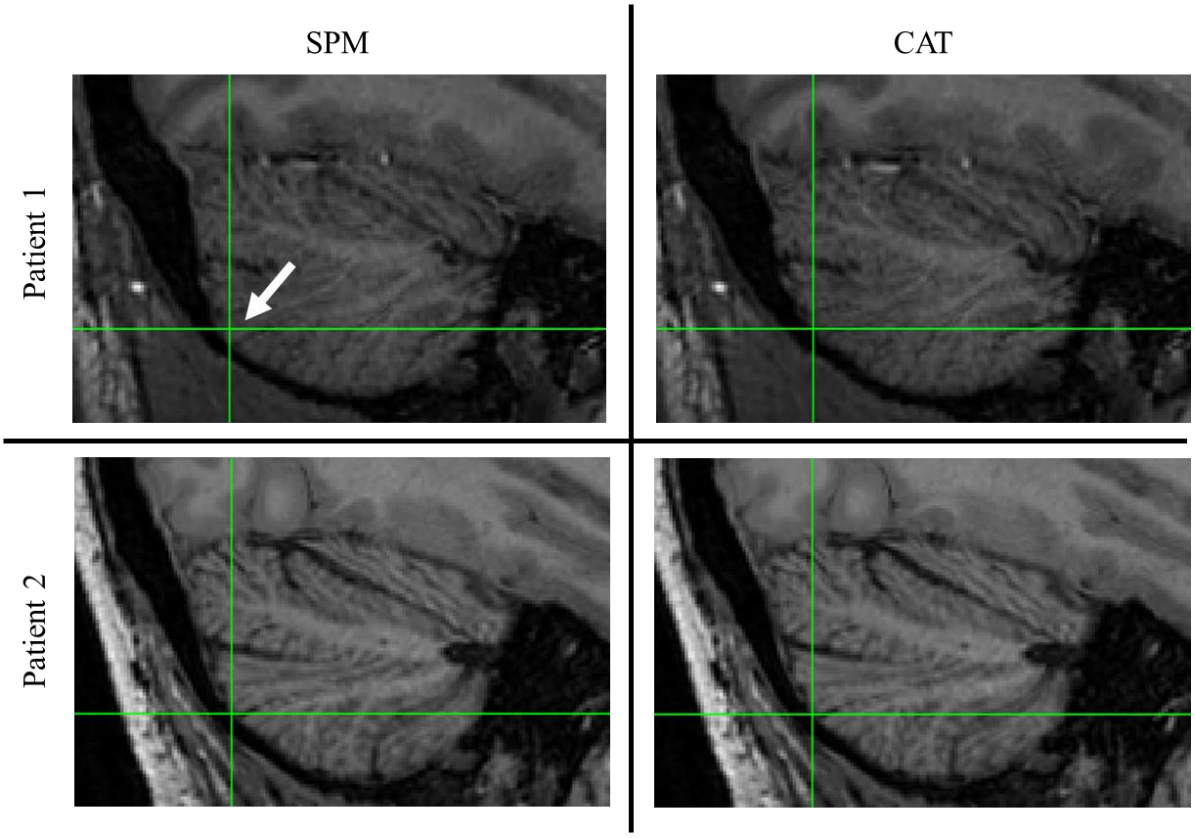

Figure 4.17: Sagittal section displaying the quality of the inter-subject registration, represented by the two age extremes of the patient dataset. The alignment is fixed on the cerebellum, a problematic area due to the original effect of bias. The arrow highlights the misalignment between the two patients present in the results from SPM.

It is hard to validate the quality of the subject registration step when looking at the lesions as there is no ground truth of what to expect from a lesion after having been warped to the template space. That is why a comparison of the registration of lesions between the two segmentations is not performed.

If the brains suffer deformations to align with the template brain, the lesions should also be deformed and, as a result, lose their original topography. If the flow fields that come from the creation of the average templates are applied the respective lesion masks, they should be able to accompany the change in topography and to continue to represent the lesion. The quality of the alignment is influenced by the quality of the lesion segmentation. This is depicted in **Figure 4.18**.

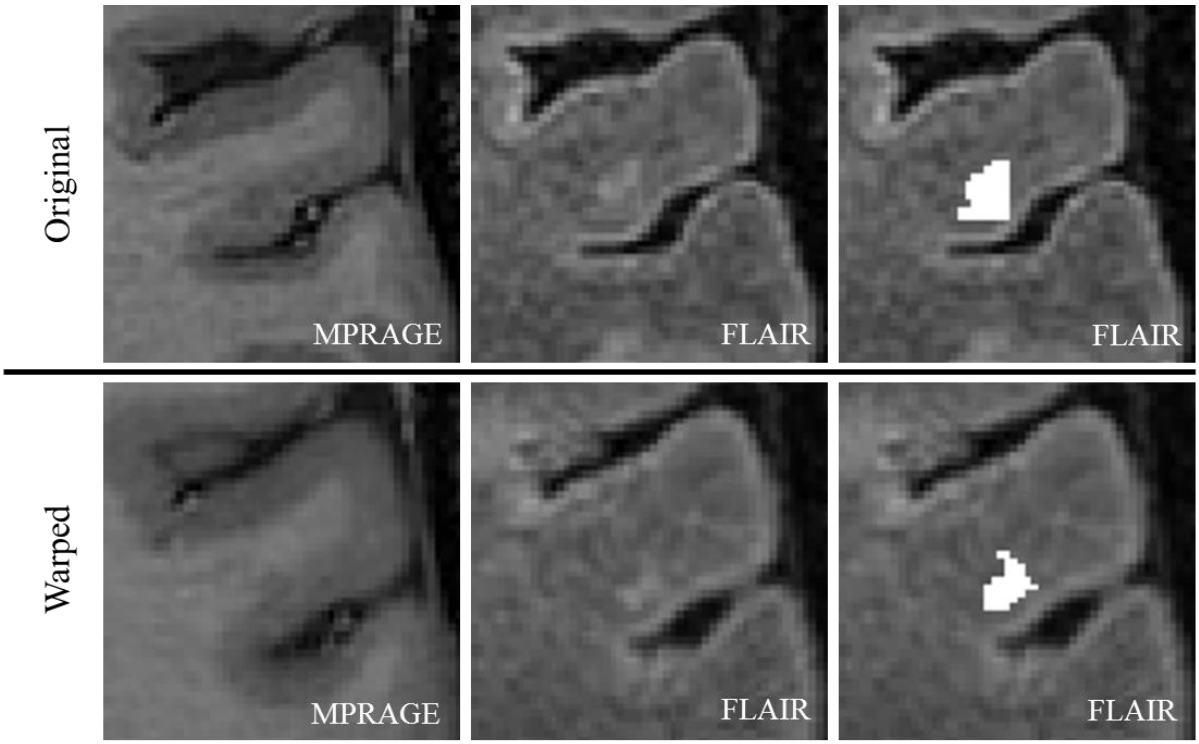

Figure 4.18: Axial cuts displaying the warping of a lesion following the subject registration. The FLAIR image is also included to allow a better perception of the lesion borders which influenced the manual segmentation. When the patient's flow field is applied to the lesion mask, the resulting mask shows a reasonable depiction of the new lesion topography.

4.5 Surface Creation

The warped MPRAGE volumes acquired from the subject registration using CAT were used to acquire an average brain. In **Figure 4.19**, the average brain for the patient dataset is displayed and two warped volumes from two patients are included for comparison.

As expected, the average brain is more affected by smoothing than the subjects' brains. This was already suggested by the subject registration step where a good alignment to the template brain was accomplished in more central structures but where a comparatively weaker alignment was found for the brain borders due to the still existing morphological individual differences. If the individual data already went over non-linear transformations to align to the template brain, already causing some smoothing of the data, the averaging procedure can only increase this effect on the resulting image. Still, the capacity of the average brain to represent the anatomy of the organ has not been compromised. In the figure, an area where the individual differences is well denoted on the warped images, which translated into the smoothing effect mentioned on the average brain, is highlighted.

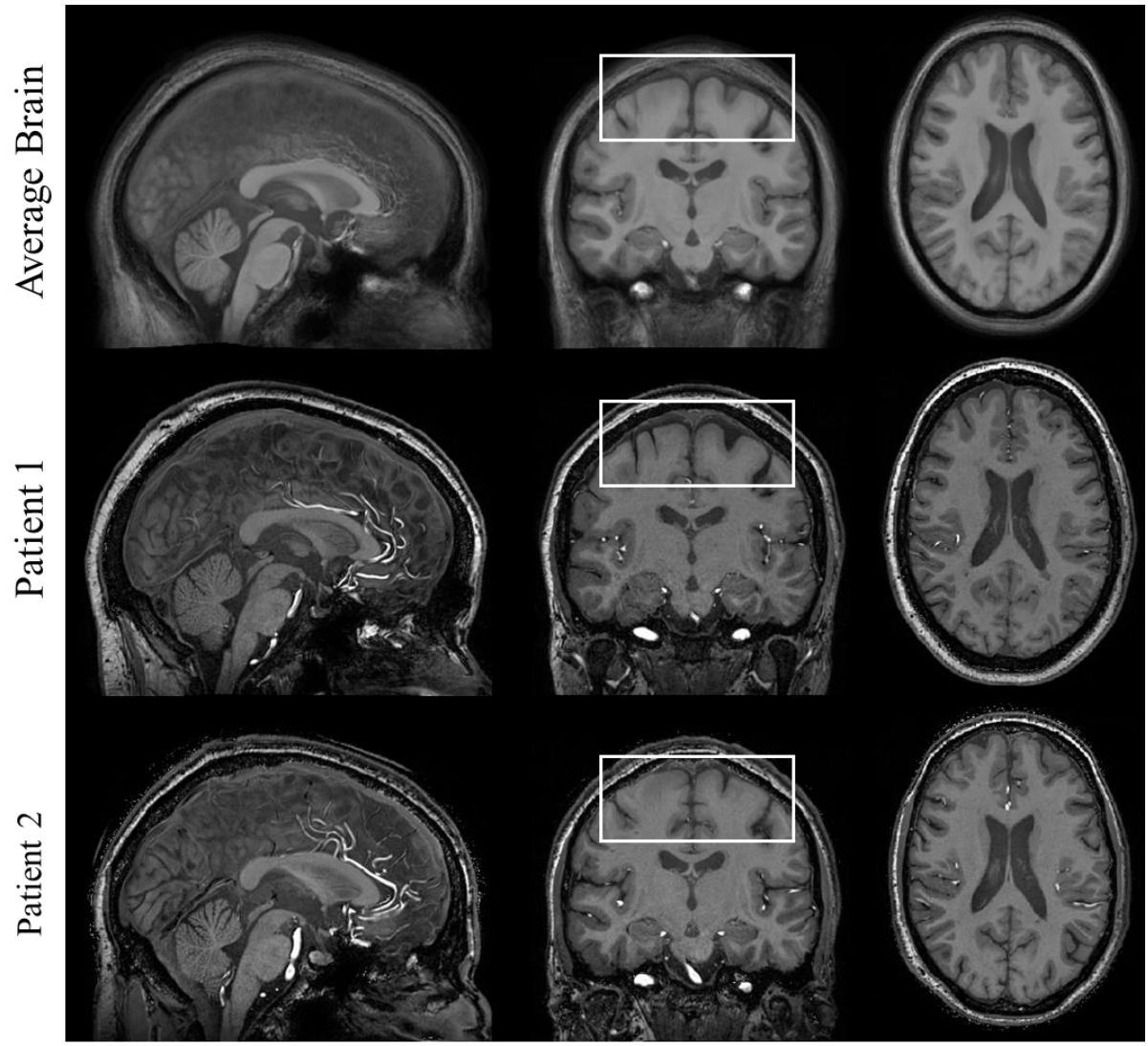

Figure 4.19: Average MPRAGE brain created from the patients' warped volumes. The warped volumes for two patients are displayed for comparison. Inherent differences between the patients which were not accurately corrected during the subject registration contributed to the smoothing effect present on the average brain.

Afterwards, FreeSurfer's *recon-all* procedure was run for the same two patients and the average brain to create the surfaces of interest. As there was a possibility of running the procedure with a feature to account for submillimeter resolution data, this alternative approach at surface creation was considered, although only to the average brain, due to time limitations. The acquired surfaces for white matter, grey matter (or pial surface) and the inflated surface are presented in **Figure 4.20**. Overlaid on the average brain is the result from the recon-all procedure for submillimeter data, to allow a better comparison with the conventional procedure.

The three surfaces show expected results for all cases, when compared to what literature suggests [82],[84],[107]. The use of the feature for submillimeter data originated poor results. This is seen by a rough white matter surface, a fragmentation of the gyri in the pial surface and by the presence of gyri fragments in the sulci regions and vice-versa in the inflated surface.

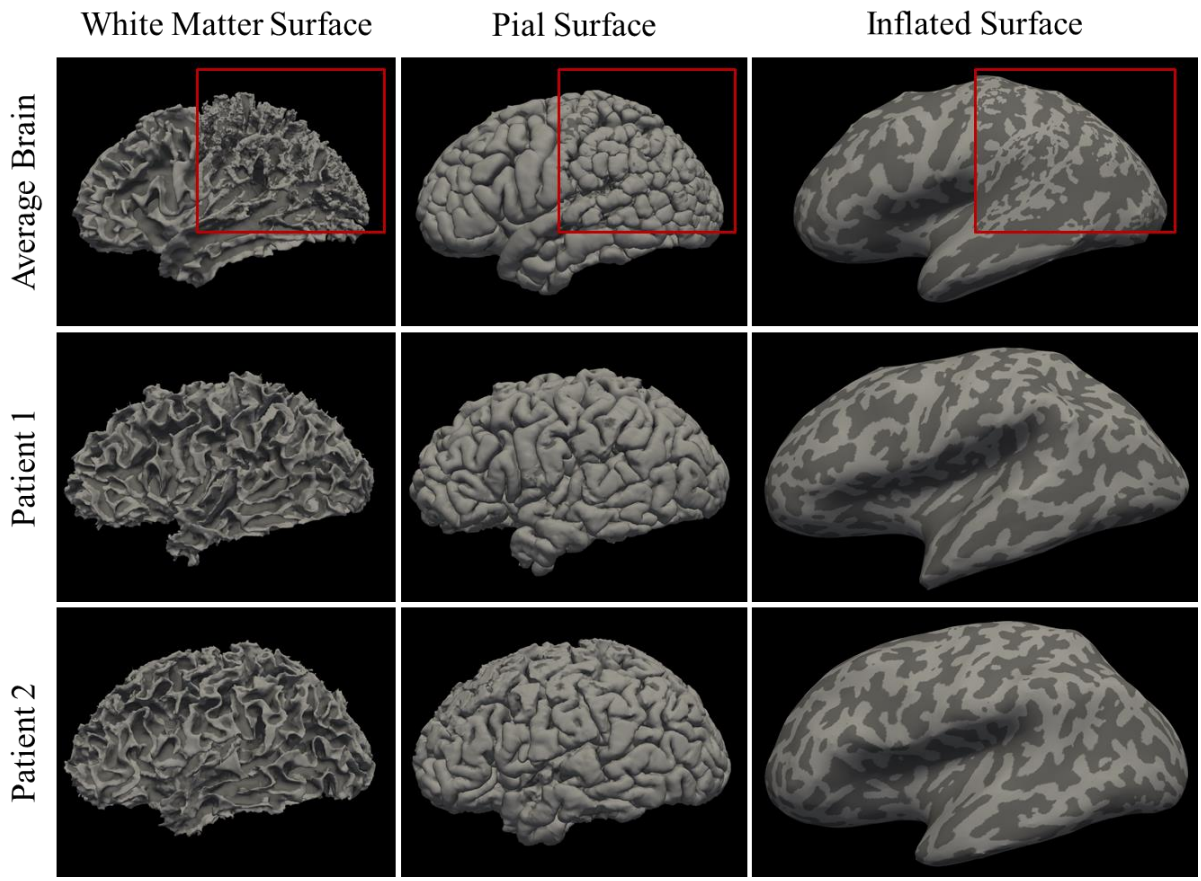

Figure 4.20: White, pial and inflated surfaces created in FreeSurfer for the average brain and two patients. The feature for submillimeter resolution applied to the average brain, overlaid on the images, led to unwanted results in all three surfaces.

For the representation of the cortical lesions, the surface of interest is the inflated one, as it allows a good visual representation of the sulci. On the inflated surface sulci and gyri are distinguished by their coloration with sulci corresponding to the dark grey tone and gyri to the light grey. The result of the overlay of the lesion masks on the respective surfaces, for the two patients and the average brain, is shown in **Figure 4.21**. The entirety of the patients' inflated surfaces with their respective overlaid lesions can be found on the **Appendix H** section of this dissertation.

In total, 253 cortical lesions were segmented and are distributed across the individual patient inflated surfaces and combined in the average brain. Of those, 119 lesions were found in the left hemisphere, whereas the remaining 134 were on the right. There was only convergence of two lesion voxels in the patient dataset. Some of those situations are highlighted in the average surface image with arrows. The figures suggest that the overlap of lesions tends to be more frequent in the cortical sulci compared to the gyri.

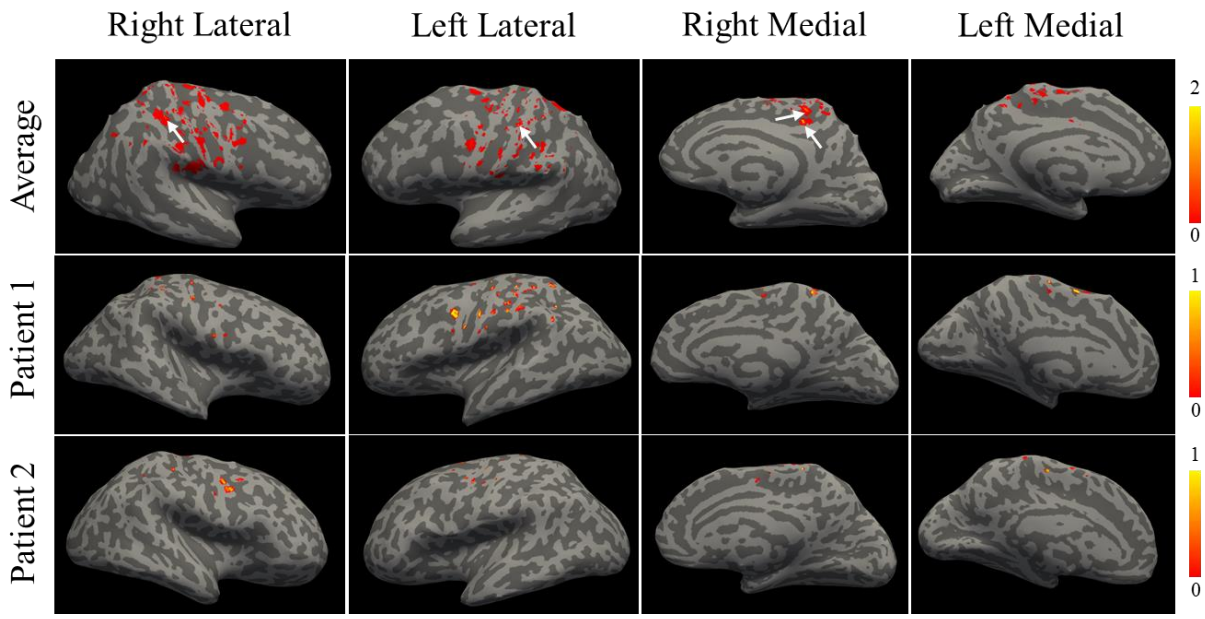

Figure 4.21: Inflated surfaces of two patients and the average brain displaying the topography of cortical lesions for the patients and the entire patient dataset, respectively. The arrows on the average surface point at areas where overlaps of lesions were found.

5 Discussion

In this chapter, the results obtained and presented in **Chapter 4** are discussed. The chapter is organized in a similar way to the previous chapters, separating the pipeline steps into individual sections to allow a better organization of the work. In the end, some final remarks on the project are given.

5.1 Bias Correction

As mentioned in the Background section of this dissertation, bias is the result of inhomogeneity in the external magnetic field, B_0, and RF excitation fields, B_1, as well as a result of regional differences in the magnetic properties of the imaged tissues which are intensified at higher magnetic fields [69],[70]. Even though bias correction is not a mandatory step in MRI image processing, its effect is stronger when dealing with higher fields and can compromise the accuracy of other image analysis methods. Furthermore, at 7 T, it is known that MS' subpial lesions may go undetected if bias is not corrected for [72]. That is why a bias correction step was incorporated in this project.

For this step, literature pointed in the direction of SPM and two different configurations were tested in the assessment of the quality of the bias correction using this software. The two configurations corresponded to the default SPM12 configuration and a configuration that was equal to the default one except for a difference in the FWHM and regularization parameters. This configuration corresponded to the ideal one in a study which combined the different possibilities for the two parameters in search for one that led to a minimal root mean square error between the simulated and the estimated bias correction field at 1.5 T, 3 T and 7 T [104]. To assess the quality of SPM in the correction of bias in this project's data and using these two different configurations, a visual and a histogram analysis were conducted.

In the uncorrected volume histograms, it was always hard to distinguish the three regions corresponding to the three tissue classes, GM, WM and CSF. Correcting for bias, regardless of the parameters, already contributed to a clear distinction between GM and WM, and the identification of a third region as CSF. The histograms also showed that for the enhanced volume histogram, the GM and WM peaks were steeper, which would signify a more accurate definition of a threshold boundary to separate both classes. The presence of the GM and WM peaks was only absent for one of the patients due to the amount of brain damage from the disease associated with high degrees of motion during the MPRAGE scan.

When doing a visual assessment of the data, shown in this dissertation using data from a patient and a healthy control, the nonuniformities in the image intensities were easily noticeable in the original scans. The cerebellum was one of the structures particularly affected by bias, appearing much darker than the surrounding tissue, and leading to a loss of signal in this region. This was also common in other lower brain structures as well as in the lateral regions.

The SPM parameters that were changed in the correction of bias were the FWHM and the bias regularization. The first tells us how smooth or sharp the Gaussian function that models the bias across the image will be. If the parameter is large, the correction is smoother and happens more globally. By aiming at smaller values, the correction is done more locally. The bias regularization works on the

intensity variations within the Gaussian function and accounts for the flexibility in the correction of bias. Usually, if data is expected to be heavily affected by bias, this parameter should be lighter to allow the model more flexibility [108]. In the study which inspired the approach tested in this bias correction step, it was the combination of a smaller FWHM and of a higher regularization that led to the enhanced configuration at 7 T [104].

It was possible to denote whether the enhanced configuration was a good combination, compared to the default one, by assessing the bias fields that SPM created, bearing in mind that the bias field in SPM is multiplicative. The results showed that the bias field in the enhanced configuration is more accurate at finding the regions within the brain that have been affected by bias. This is a result of the narrower Gaussian function, which caused the estimated bias field to be more localized. As a result, the correction is also more focal which led in the sagittal cut result to a stronger correction of the bias in the cerebellum. In the default configuration, the image intensities upon correction are more distributed throughout the entire image, extending to areas outside of the brain which are not of interest to this pipeline.

Another way of understanding the impact of one method over the other was to look at the quality of the segmentation, since the bias correction step in SPM is integrated in a segmentation procedure and both processes are intertwined. These results were shown by displaying with a warm colormap the voxel probabilities normalized for one of the tissue classes, in this case GM. When looking at GM/WM boundary regions it should be expected that if a voxel displays a probability close to 1 of belonging to GM, in the respective WM map the same voxel would display a probability close to 0. These results showed a more accurate delineation of the cortex for the enhanced configuration. This was seen by more certainty being given to the cortical voxels (displayed by a higher density of voxels with higher probabilities, i.e. a higher predominance of yellow voxels) and a better segmentation of the cerebellum. The consistency found in the visual results which aligned with the histogram analysis led to the choice of using SPM in the correction of bias using the enhanced configuration parameters.

Cortical lesions were also checked before advancing in the pipeline. This was due to the concern that the ability to spot cortical lesions could be compromised after performing bias correction. Results showed that the correction of bias did not alter the visibility of cortical lesions, regardless of their type, size or location. Lesions remained as hypointensities or hyperintensities, depending on the contrast used in their visualization, compared to the surrounding tissue after being corrected.

5.2 Coregistration

As the data for this project came from a cross-sectional study and all volumes were acquired within the same session, it was agreed that no structural changes would have occurred between the scans and therefore the coregistration could be done by means of rigid body transformations. For this reason, the starting point for this coregistration step was the script built using SPM's functions for the pre-processing of 3 T data from MS patients at DRCMR. This script performed within-subject registration and an alignment to the MNI template of 1-mm by means of rigid body transformations.

In the initial attempt to run the script without any alterations other than the change of the MNI template to one of resolution 0.5-mm to avoid downsampling the data, it was denoted that the skull seemed to be influencing the quality of the data. To account for this, the alignment to the MNI space was performed with masked brains, instead. It was also decided that the coregistration would be split into different steps so that firstly only one contrast was aligned to the MNI space and after that the resulting contrast became the volume to which the other contrasts would be aligned to. This way, the main within-subject alignment was still performed between the individual 7 T data, instead of with

regards to the MNI template acquired from 3 T data. An intermediate step would be added so that the final alignment could be done between unmasked volumes. This was thought to improve the quality of the results.

The results showed that the three distinct coregistration processes integrated into this step successfully aligned the individual subjects' data. For instance, the alignment of the masked MPRAGE volumes to the masked MNI template allowed a good alignment of the data to the template, but by avoiding non-linear transformations the individual data preserved its morphology and location. This was important as the cortical lesions had not been manually segmented at this point. The intermediate alignment between the masked and unmasked MPRAGE of each participant unsurprisingly led to a very accurate alignment of the images due to their resemblances. At last, the success of the within-subject alignment was confirmed by the overlay of the different contrasts for the same subject in search for the correction of areas of discontinuity.

A successful coregistration should allow the different contrasts to be used during the lesion detection task to confirm whether a finding of interest is a lesion and whether it is found within GM or in between GM and WM. The results presented confirm the ability to shift between the different contrasts and to confirm the presence of cortical lesions after coregistration.

SPM proved to be a fast and trustworthy tool in the performance of small alignments to correct for motion between the MRI scans acquired. That led to its integration in the image processing pipeline for the within-subject registration of this project's data. Motion can also occur during scans but the 7 T Achieva MR system used at DRCMR contains a patch that already accounts for and corrects some of the subject motion during the data acquisition by making use of a navigator-based prospective motion correction system called iMOCO [109]. That is the reason why within-motion was not a concern in this project.

5.3 Brain Segmentation

Three different approaches were tested for brain segmentation: SPM, the SPM toolbox CAT and FSL's FAST tool. As SPM had been the software used in the previous steps and its results were suggestive of a positive handling of UHF data, it was initially considered for this next pipeline step and to provide preliminary results needed for the CLiMS project. The other two approaches were later considered and came from suggestions of other researchers at DRCMR. The results for the brain segmentation focused on the GM probability maps, given the interest in studying cortical pathology.

It became clear from the first assessments that SPM had a lower performance than the other two approaches, displaying a low but still present likelihood of voxels within WM belonging to GM, not as pronounced in CAT nor FAST. Upon closer inspection and by filtering the data with changes in the threshold values, higher threshold values led to a weak representation of the cortex in SPM. FAST revealed a tendency to pick and classify voxels outside of the cortex as GM, even at high threshold values. When looking at the delineation of the cortex, CAT showed more accurate results, even in areas where a poorer contrast between GM and WM was present as a result of differences in tissue properties.

In the end, CAT was chosen for the brain segmentation of the patients' data for its consistent accuracy and reliability in the segmentation of the GM class, also applicable to the WM class. So long as its code is accessed and changed to avoid data downsampling, the segmentation that results shows adequacy.

5.3.1 Lesion Segmentation

Literature on cortical lesions at 7 T vastly showed that cortical lesions are still being manually segmented due to the absence of more robust computational tools for their detection. This is also a result of the recent interest in studying cortical pathology after decades of focusing on WM pathology in MS. As it has been pointed out in other parts of this dissertation, there is still a lot to be understood about cortical lesions. UHF-MRI scanners have improved the ability to spot them, but their sensitivity is still nonideal. Moreover, it is still unknown how to properly identify and segment cortical lesions at 7 T and how to differentiate a lesion from other possible findings. The ideal MRI contrast to detect cortical lesions, if it exists, is still under debate.

In this project the detection and segmentation of cortical lesions was done manually using FSLeyes. MIPAV and Jim were also tested but the former did not offer a simple and intuitive interface. The drawing task was also the most time consuming out of the three approaches. Jim offered an interface that was not suitable when looking for small findings. The shifting between anatomical views was not as direct and easily available as in FSLeyes, making it hard to look for and to confirm the nature of the lesions without repetitively making use of zooming tools.

Common guidelines were made for making the lesion segmentation task less rater-dependent. Still, group discussions confirmed that the drawing of lesions, particularly the definition of the lesion borders were always dependent on the drawer. Due to the inexperience of all elements of the group in the detection of cortical lesions at 7 T, it was not always possible to confirm whether a finding was indeed a lesion or not. A robust automatic tool for lesion detection, possibly combining the field of neuroimaging and machine learning, would be a definite help in the detection of these lesions. It would not only significantly speed up the process and exclude the subjective element in the detection but it would offer more accuracy and reliability. For now, the task is still dependent on external factors, some extrinsic to the rater, such as the light in the room where the task is performed or the brightness and size of the screen, and some intrinsic to the rater, such as the level of boredom, concentration or tiredness, attention to detail and patience.

Upon experimenting with all available contrasts, the FLAIR sequence was chosen for the detection of cortical lesions, with the possibility to use the MPRAGE for confirmation. The possibility to blindly perform the detection was considered but discarded upon the creation of the segmentation guidelines due to the difficulty in identifying findings and confidently classifying them as cortical lesions. This led to the decision to include a second contrast that showed good contrast between grey matter and white matter to avoid misclassifying WM-GM lesions as cortical lesions and/or skip over leukocortical lesions.

A CNR study was performed with preliminary results to look for a way to validate the choice to use the FLAIR sequence. At the time, several lesions had already been detected with the FLAIR sequence. Even though negative outcomes would not have changed the choice to use the FLAIR contrast in this project, the knowledge that came from this analysis could still impact the choices for the CLiMS project and lead to changes in the course of the detection from then on. That is why it was still decided to perform this parallel study to the segmentation task. However, the positive preliminary results already indicated a better CNR for the FLAIR sequence confirming the choice to use in this task. When applying this analysis to the full data, the results showed consistency with the preliminary results but more reliability, due to the higher number of lesions included. The p-values obtained confirmed the difference already denoted in the boxplots.

The CNR parameter is a measure that is deeply influenced by the way the lesion and consequently the neighborhood of the lesion is defined. By being detected by unexperienced raters, it is not possible

to secure that all lesions were well detected and delineated and that they do not include voxels from non-lesioned tissue. On the other hand, the regions created around the lesion and used in the calculation of the lesion neighborhood were defined to be spheres. Lesions differ in shape and are rarely depicted as exact spheres but this was thought to be the closest approximation to their shape. This could have also impacted the quality of the neighborhood regions created around some lesions.

The mean of values, used in the calculation of the *signal* parameter in the lesion and neighborhood regions, already aimed at reducing the weight of those wrongly classified voxels in the measures. Still, their effect is still present in the values obtained. The neighborhood, built to consider only GM values, was also an attempt to avoid differences which were not a result of the noise but of the different regions where the neighborhood might have fallen depending on where the lesion was found. Still, if the neighborhood is still dependent on the quality of the segmentation of GM which albeit good was still not ideal, as seen in **Chapter 4** Section 4.3, this could explain the outliers found for some of the CNR values present in the different contrasts. Even then, the quality of the coregistration procedure which aligned the four contrasts and allowed this study to be performed to all contrasts should ensure that at least all CNR values were calculated on the same regions and under the same conditions.

5.4 Subject Registration

Subject registration, the inter-subject alignment procedure of this pipeline, was performed in DARTEL using two different sets of data for the creation of an average template to which the MPRAGE volumes would then be warped too and consequently reach an alignment by means of non-linear transformations.

The different sets of data corresponded to the resulting tissue class volumes from the segmentation of the MPRAGE volumes using SPM or CAT. As it was previously mentioned, SPM had originally been used for the acquisition of preliminary results and later, when the segmentation procedure was revisited and CAT was tested, its improvement in the quality of the segmentation was assumed to also extend to a better registration of the subjects' data.

The first assessment done was the visual comparison of the average templates. It was found that CAT better delineated the cortical borders in the GM template and showed better detail on the WM in the WM template. This led to a better definition of the templates, particularly in the brain borders, and a lower effect of smoothness, more present in SPM's average templates. To understand if this difference could also be explained by a more pronounced variance in the tissue class voxel values of the subjects' tissue maps obtained with SPM with regards to the mean values, a coefficient of variance analysis was performed for all patients.

The boxplots for GM and WM using the segmented volumes from CAT occupied lower CV values and showed a smaller distribution of the values across the patient dataset. The boxplots for the tissue classes using SPM occupied higher values on the CV scale, which varies between 0 and 1. In the WM class there was also a better dispersion of CV values between the patients, seen by the longer whiskers. If this parameter measures the degree of dispersion of values around the mean, higher CV values for the SPM segmentation indicate a higher dispersion of the tissue voxel values compared to CAT. The results shown in **Chapter 4** Section 4.3 already revealed that CAT had more density of voxels with high certainty, which should consequently increase the mean value for this class. The longer whiskers in the SPM results were also suggestive of more inconsistency in the results which appear to fluctuate depending on the patient and, possibly, the level of damage from the disease or the image quality.

The low sharpness of the SPM templates translated into a poorer registration of the subjects' data. When looking at central brain regions both approaches displayed a good alignment and warping of the individual morphology, but more peripherical regions, such as the cerebellum, strongly affected by bias at 7 T, already led to a discrepancy in the performance of the registration using SPM or CAT's results, with the former failing to align this structure between patients. The results also showed that although good alignment of the overall structures is obtained with CAT's results, there is still variability within the structures themselves and therefore an ideal warping was still not obtained.

The registration led to a warping of the lesions and therefore a loss of their initial topography. As the lesions had already been detected and segmented, the use of non-linear transformations did not compromise the quality of the results. Moreover, the good alignment of the warped lesion masks to the warped lesions ensured a good tracking of the lesions and a good representation of their new morphology after the registration. It also helped to prove the accurate and consistent performance of DARTEL.

DARTEL showed a good performance and stability when using 7 T data of higher resolution. The templates revealed a good depiction of the expected brain tissues classes and the quality of the alignments, subject to template, subject to subject, or lesion mask to lesion, showed an accurate registration of the data, particularly when using the segmentation results obtained with CAT. That is why DARTEL was chosen and implemented in the image processing pipeline. The ability to accurately depict the lesions does not seem to be a limitation of DARTEL but, instead, of the quality of the manual segmentation task. If the masks fail to accurately delineate the lesion borders in the original image, they will extend into a poorer delineation of the lesions pos-registration.

5.5 Surface Creation

The aim of the surface creation step was to acquire surfaces for the individual as well as average brains so that the respective cortical lesions could be overlaid and a good visualization of the distribution of these lesions and their overlaps, when existent, could be done.

From the surfaces that FreeSurfer allows, the inflated was the surface of interest due to its ability to display the sulci. The creation of the average brain was the first step towards allowing the creation of an average surface. The comparison of this result to the warped volumes of two patients demonstrated that although some level of smoothness was present due to individual differences that had not been removed after the warping, a good representation of the brain and its anatomy was still present.

Upon running FreeSurfer for the three mentioned cases, the surfaces obtained already showed consistency with what was expected from literature [82],[84],[107]. Successful results were not obtained for the *recon-all* procedure using the feature for higher-resolution data. Even with the correction of the skull-stripping problem, which was done using FreeSurfer commands and later by using in-house tools which are still being developed, the resulting surfaces still displayed poor results. This was seen by a rougher appearance in the white matter surface and a strange fragmentation of the cortex in the pial surface, both of which extended into the inflated surface to a non-uniform distinction of the gyri and sulci regions which contained fragments of the other.

The success of this submillimeter approach had been achieved for data of 0.75-mm in resolution [107] and it is likely that more modifications need to be implemented before similar results can be achieved for higher resolution data. The consequence of not resorting to this submillimeter tool was a downsampling of the data to 1-mm during this procedure. As FreeSurfer was only used in the end of the pipeline this downsampling of the data was not considered to be an inconvenient. The acquired maps

showed good quality, including the average map, and the possibility of overlaying the cortical lesions on the respective maps, the main objective of this step, was accomplished for all cases.

The individual surfaces with the overlaid lesions, found both in **Chapter 4** Section 4.5 and in the **Appendix H** section of this dissertation, denoted the discrepancy in the extension of lesions found for the different patients. Whereas for some patients, cortical lesions were abundant, some had barely any lesion. When displaying the results of the sum of all lesions masks, overlaid on the average brain surface, it was found that only overlaps of two lesion voxels occurred for the 253 lesions detected in total. In this study, lesions were more predominant on the right side and the visual analysis suggested that the overlaps tend to be more common in the cortical sulci. Even though the study was performed on a very limited number of patients and this analysis is done without the use of robust tools for cortical lesion detection, this would support recent literature that suggests that cortical lesions develop predominantly intracortically and within sulci [98]. A more in-depth analysis will allow a better understanding of how the lesions are distributed between the cortical sulci and gyri on the SM1 area.

5.6 Final Remarks

Although the aims of this project were accomplished and a pipeline for the processing of structural 7 T MRI data from MS patients was built, a few considerations should be made on the overall project.

Time and lack of prior knowledge on the implementation of the different pipeline steps using higher resolution data were the two main limiting factors during this project and influenced the extent of the analyses and tests performed at each step. Priority was given to visual assessments, as these should always be integrated to ensure and confirm the quality of the data at each moment. Furthermore, as a part of a bigger project focused on the quality of the pipeline for the identification and study of cortical lesions, the use of visual results in the display of the progress made allowed a clearer knowledge transfer between the group elements.

If the main challenge of UHF-MRI scanners is the added bias, the bias correction step should have been better explored, making use of different software tools besides SPM and testing it under different conditions. Although the results obtained highlighted the potential of the enhanced SPM parameters in the correction of bias, only two configurations were tested. The experimentation with other sets of parameters could have contributed to a better correction of bias, extending into subsequent steps. Moreover, the exploration of the default configuration in the quality of the following pipeline steps would have allowed a more conclusive understanding of the impact of a poorer bias correction on the final pipeline results.

Due to the limiting factors previously mentioned, the ability to experiment with different software packages and approaches was compromised and was the reason why in some steps only one approach was considered and later implemented, so long as it provided adequate results. This was also a result of the time-consuming task of manually segmenting cortical lesions using guidelines that were also being developed at the time. Lack of proper tools for lesion segmentation, need for more expertise and the repetitiveness of the job further contributed to the slowness of the process.

The results obtained for the average brain, displaying levels of smoothing, depicted the challenges of the subject registration step. Even though an adequate alignment of the cortex borders and brain structures was reached, an impeccable warping of the patients' individual data was not obtained. It would be unrealistic to expect an exact warping of the patients' data. Still, the procedures implemented and the results obtained, particularly the average brain surface to which the sum of the lesions segmented was overlaid, confirmed a good processing of this project's data. This shows that the MRI image

processing tools currently available and tested in this project present overall good performance and reliability in the processing of higher resolution data of MS patients, one of the initial concerns of this project.

This project's positive outcomes lay the foundation for further analyses to be conducted in the CLiMS project. Some of the future work envisaged in the following months include: a parcellation of the inflated brains in FreeSurfer to properly identify the location of the lesions and exclude any lesions detected outside the SM1 region; a differentiation of the lesions into their different types so that lesion location, amongst other parameters and correlates, can also be studied by lesion type; the application of the coregistration tools and FreeSurfer commands to the fMRI data acquired to overlay it on the respective brain surfaces and enable its correlation with the lesions; and the application of the pipeline steps to the quantitative MRI data acquired in the bigger project for its use in quantitative studies that will monitor the subtle changes across subjects that might have occurred due to the progression of the disease. Should it be necessary, the healthy controls' data, only processed up to the brain segmentation step, can also undergo the remaining pipeline steps. This might be the case if it is agreed that the average brain should consider, not only the patients' data, but the entire dataset.

6 Conclusion

The Master's project extensively described in this dissertation aimed at processing the structural 7 T MRI data from a PhD project taking place at DRCMR. More specifically, it aimed at developing a semi-automated pipeline to be used in the display and study of cortical lesions in an individual and group setting. The initial assumption was that the performance of common medical imaging software packages would be poorer when using inherently higher resolution data. Results showed that the current MRI image processing tools available present overall good performance and reliability in the processing of higher resolution data of MS patients. Still, the quality of the outcomes can be optimized by including additional steps or changes to the original software configurations. More research is needed to understand the performance of these and other software packages in the processing of higher resolution MRI data and how to fully exploit these tools in the study of clinical data at 7 T.

The manual lesion segmentation task proved to be time-consuming and rater-dependent. Internal and external factors which influenced the detection of cortical lesions could be minimized by a robust automatic tool, needed to improve the reliability of this task. Even then, it was found that, from the 253 cortical lesions manually segmented during this project, the majority occurred on the right hemisphere and lesion overlaps between patients were more common in cortical sulci. The manual lesion segmentation and application of this pipeline to the remaining patients will allow a more extensive study of cortical pathology and the possibility of understanding the impact of single or groups of cortical lesions on the connectivity and functional integrity of the cortical area affected.

The work carried for this dissertation contributed to the development of two abstracts. The first was presented at the annual meeting for the Danish Multiple Sclerosis Society, *Scleroseforeningen*, on March 29, 2019. The second will presented at the 2019 European Committee for Treatment and Research in Multiple Sclerosis (ECTRIMS) conference in September 2019. Information regarding the two publications and the researchers involved can be found on the **Appendix I** section of this report. The success of this project also granted the author the possibility of continuing to work at DRCMR with a Research Assistant position starting in October 2019, for an extended period of six months.

References

[1] Geurts JJ, Barkhof F. Grey matter pathology in multiple sclerosis. Lancet Neurol 2008;7:841–51.

[2] Kidd D, Barkhof F, McConnell R, Algra PR, Allen IV, Revesz T. Cortical lesions in multiple sclerosis. Brain 1999;122:17–26.

[3] Magliozzi R, Reynolds R, Calabrese M. MRI of cortical lesions and its use in studying their role in MS pathogenesis and disease course. Brain Pathol 2018;28:735–42.

[4] Mainero C, Benner T, Radding A, Van Der Kouwe A, Jensen R, Rosen BR, et al. In vivo imaging of cortical pathology in multiple sclerosis using ultra-high field MRI. Neurology 2009;73:941–8.

[5] Filippi M, Evangelou N, Kangarlu A, Inglese M, Mainero C, Horsfield MA, et al. Ultra-high-field MR imaging in multiple sclerosis. J Neurol Neurosurg Psychiatry 2014;85:60–6.

[6] Kilsdonk ID, Jonkman LE, Klaver R, Veluw SJ Van, Zwanenburg JJM, Kuijer JPA, et al. Increased cortical grey matter lesion detection in multiple sclerosis with 7 T MRI : a post-mortem verification study. Brain 2016;139:1472–81.

[7] Datta R, Sethi V, Ly S, Waldman AT, Narula S, Dewey BE, et al. 7T MRI Visualization of Cortical Lesions in Adolescents and Young Adults with Pediatric-Onset Multiple Sclerosis. J Neuroimaging 2017;27:447–52.

[8] Harrison DM, Roy S, Oh J, Izbudak I, Pham D, Courtney S, et al. Association of Cortical Lesion Burden on 7-T Magnetic Resonance Imaging With Cognition and Disability in Multiple Sclerosis. JAMA Neurol 2015;72:1004–12.

[9] Huntenburg JM, Steele CJ, Bazin PL. Nighres: processing tools for high-resolution neuroimaging. Gigascience 2018;7:1–9.

[10] GBD 2015 NDCG. Global, regional, and national burden of neurological disorders during 1990 – 2015 : a systematic analysis for the Global Burden of Disease Study 2015. Lancet Neurol 2017;16:877–97.

[11] Reich DS, Lucchinetti CF, Calabresi PA. Multiple Sclerosis. N Engl J Med 2018;378:169–80.

[12] Olsson T, Barcellos LF, Alfredsson L. Interactions between genetic , lifestyle and environmental risk factors for multiple sclerosis. Nat Publ Gr 2016;13:25–36.

[13] Thompson AJ, Baranzini SE, Geurts J, Hemmer B, Ciccarelli O. Multiple sclerosis. Lancet 2018;6736:1–15.

[14] Hemmer B, Kerschensteiner M, Korn T. Role of the innate and adaptive immune responses in the course of multiple sclerosis. Lancet Neurol 2015;14:406–19.

[15] Lucchinetti C, Bruck W, Parisi J, Scheithauer B, Rodrigues M, Lassmann H. Heterogeneity of Multiple Sclerosis Lesions : Implications for the Pathogenesis of Demyelination. Ann Neurol 2000;47:707–17.

[16] Lucchinetti CF, Popescu BFG, Bunyman RF, Moll NM, Roemer SF, Lassman H, et al. Inflammatory Cortical Demyelination in Early Multiple Sclerosis. N Engl J Med 2011;365:2188–97.

[17] Bo L, Vedeler CA, Nyland HI, Trapp BD, Mork SJ. Subpial Demyelination in the Cerebral Cortex of Multiple Sclerosis Patients. J Neuropathol Exp Neurol 2003;62:723–32.

[18] Gilmore CP, Donaldson I, Bö L, Owens T, Lowe J, Evangelou N. Regional variations in the extent and pattern of grey matter demyelination in multiple sclerosis: a comparison between the cerebral cortex, cerebellar cortex, deep grey matter nuclei and the spinal cord. J Neurol Neurosurg Psychiatry 2009;80:182–7.

[19] Green AJ, Mcquaid S, Hauser SL, Allen I V, Lyness R. Ocular pathology in multiple sclerosis: retinal atrophy and inflammation irrespective of disease duration. Brain 2010;133:1591–601.

[20] Barros P, Sá MJ. Management of Motor Symptoms in Multiple Sclerosis. Eur Neurol Rev 2013;8:124–9.

[21] Brassington JC, Marsh N V. Neuropsychological Aspects of Multiple Sclerosis. Neuropsychol Rev 1998;8:43–77.

[22] Galey T, Miller C, Nazareth M, Bakshi R, Brownscheidle CM, Weinstock-Guttman B, et al. Sensory Abnormalities in MS: Patient Descriptions of "Macrosomatic Illusions". Int J MS Care 2004;6:144–7.

[23] Chiaravalloti ND, DeLuca J. Cognitive impairment in multiple sclerosis. Lancet Neurol 2008;7:1139–51.

[24] Trapp BD, Nave K-A. Multiple Sclerosis: An Immune or Neurodegenerative Disorder? Annu Rev Neurosci 2008;31:247–69.

[25] Noseworthy JH, Lucchinetti C, Rodrigues M, Weinshenker BG. Multiple Sclerosis. N Engl J Med 2000;343:938–52.

[26] Types of MS 2018. https://www.mstrust.org.uk/about-ms/what-ms/types-ms (accessed September 1, 2019).

[27] Mcdonald WI, Compston A, Edan G, Goodkin D, Hartung H, Lublin FD, et al. Recommended Diagnostic Criteria for Multiple Sclerosis : Guidelines from the International Panel on the Diagnosis of Multiple Sclerosis. Ann Neurol 2001;50:121–7.

[28] Polman CH, Reingold SC, Banwell B, Clanet M, Cohen JA, Filippi M, et al. Diagnostic Criteria for Multiple Sclerosis : 2010 Revisions to the McDonald Criteria. Ann Neurol 2011;69:292–302.

[29] Brownell B, Hughes T. The distribution of plaques in the cerebrum in multiple sclerosis. J Neurol Neurosurg Psychiatry 1962;25:315–20.

[30] Lumsden CE. Handbook of Clinical Neurology. Vol. 9. Amsterdam: Elsevier; 1970.

[31] Peterson JW, Bö L, Mörk S, Chang A, Trapp BD. Transected Neurites, Apoptotic Neurons, and Reduced Inflammation in Cortical Multiple Sclerosis Lesions. Ann Neurol 2001;50:389–400.

[32] Calabrese M, Filippi M, Gallo P. Cortical lesions in multiple sclerosis. Nat Rev Neurol 2010;6:438–44.

[33] Calabrese M, Magliozzi R, Ciccarelli O, Geurts JJG, Reynolds R, Martin R. Exploring the origins of grey matter damage in multiple sclerosis. Nat Rev Neurosci 2015;16:147–58.

[34] Levin LI, Munger KL, Rubertone M V, Peck CA, Spiegelman D, Ascherio A. Multiple Sclerosis and Epstein-Barr Virus 2003;289:1533–6.

[35] Maggi F, Fornai C, Vatteroni ML, Siciliano G, Menichetti F, Tascini C, et al. Low prevalence of TT virus in the cerebrospinal fluid of viremic patients with central nervous system disorders. J Med Virol 2001;65:418–22.

[36] Krishnamoorthy G, Saxena A, Mars LT, Domingues HS, Mentele R, Ben-Nun A, et al. Myelin-specific T cells also recognize neuronal autoantigen in a transgenic mouse model of multiple sclerosis. Nat Med 2009;15:626–32.

[37] Gardner C, Magliozzi R, Durrenberger PF, Howell OW, Rundle J, Reynolds R. Cortical grey matter demyelination can be induced by elevated pro-inflammatory cytokines in the subarachnoid space of MOG-immunized rats. Brain 2013;136:3596–608.

[38] Magliozzi R, Serafini B, Rosicarelli B, Chiappetta G, Veroni C, Reynolds R, et al. B-cell Enrichment and Epstein-Barr Virus Infection in Inflammatory Cortical Lesions in Secondary Progressive Multiple Sclerosis. J Neuropathol Exp Neurol 2013;72:29–41.

[39] Kreutzberg GW. Microglia: a sensor for pathological events in the CNS. Trends Neurosci 1996;19:312–8.

[40] Fischer MT, Wimmer I, Höftberger R, Gerlach S, Haider L, Zrzavy T, et al. Disease-specific molecular events in cortical multiple sclerosis lesions. Brain 2013;136:1799–815.

[41] Sailer M, Fischl B, Salat D, Tempelmann C, Schönfeld MA, Busa E, et al. Focal thinning of the cerebral cortex in multiple sclerosis. Brain 2003;126:1734–44.

[42] De Stefano N, Matthews PM, Filippi M, Agosta F, De Luca M, Bartolozzi ML, et al. Evidence of early cortical atrophy in MS: Relevance to white matter changes and disability. Neurology 2003;60:1157–62.

[43] Kutzelnigg A, Faber-Rod JC, Bauer J, Lucchinetti CF, Sorensen PS, Laursen H, et al. Widespread demyelination in the cerebellar cortex in multiple sclerosis. Brain Pathol 2007;17:38–44.

[44] Calabrese M, De Stefano N, Atzori M, Bernardi V, Mattisi I, Barachino L, et al. Detection of Cortical Inflammatory Lesions by Double Inversion Recovery Magnetic Resonance Imaging in Patients With Multiple Sclerosis. Am Med Assoc 2007;64:1416–22.

[45] Calabrese M, Gallo P. Magnetic resonance evidence of cortical onset of multiple sclerosis. Mult Scler 2009;15:933–41.

[46] Geurts JJG, Roosendaal SD, Daniëls R, Barkhof F, Bö L, Hazes T, et al. Extensive hippocampal demyelination in multiple sclerosis. J Neuropathol Exp Neurol 2007;66:819–27.

[47] Calabrese M, Poretto V, Favaretto A, Alessio S, Bernardi V, Romualdi C, et al. Cortical lesion load associates with progression of disability in multiple sclerosis. Brain 2012;135:2952–61.

[48] Scalfari A, Romualdi C, Nicholas RS, Mattoscio M, Magliozzi R, Morra A, et al. The cortical damage, early relapses, and onset of the progressive phase in multiple sclerosis. Neurology 2018;90:e2107–18.

[49] Bloch F. Nuclear Induction. Phys Rev 1946;70:460–74.

[50] Purcell EM, Torrey HC, Pound R V. Resonance Absorption by Nuclear Magnetic Moments in a Solid. Phys Rev 1946;69:37–8.

[51] Damadian R. Tumor Detection by Nuclear Magnetic Resonance. Science (80-) 1971;171:1151–3.

[52] Lauterbur PC. Image Formation by Induced Local Interactions: Examples Employing Nuclear Magnetic Resonance. Nature 1973;242:190–1.

[53] Mansfield P, Grannell PK, Maudsley AA. Diffraction and microscopy in solids and liquids by NMR. Proc 18th Ampere Congr Magn Reson Relat Phenomena Nottingham, UK 1974:431–2.

[54] Henderson RG. Nuclear magnetic resonance imaging: a review. J R Soc Med 1983;76:206–12.

[55] McRobbie DW, Moore EA, Graves MJ, Prince MR. MRI from Picture to Proton. 3rd ed. Cambridge: Cambridge University Press; 2017.

[56] Bushberg JT, Seibert JA, Leidholdt EMJ, Boone JM. The Essential Physics For Medical Imaging. 2nd ed. Philadelphia: Lippincott Williams & Wilkins; 2002.

[57] Hendee WR, Ritenour ER. Medical Imaging Physics. 4th ed. New York: Wiley-Liss; 2002.

[58] Moser E, Laistler E, Schmitt F, Kontaxis G. Ultra-High Field NMR and MRI–The Role of Magnet Technology to Increase Sensitivity and Specificity. Front Phys 2017;5:1–15.

[59] Ladd ME, Bachert P, Meyerspeer M, Moser E, Nagel AM, Norris DG, et al. Pros and cons of

ultra-high-field MRI/MRS for human application. Prog Nucl Magn Reson Spectrosc 2018;109:1–50.

[60] Moser E. Ultra-high-field magnetic resonance: Why and when? World J Radiol 2010;2:37.

[61] Balchandani P, Naidich TP. Ultra-high-field MR neuroimaging. Am J Neuroradiol 2015;36:1204–15.

[62] Westbrook C, Kaut C. MRI in Practice. 2nd ed. Oxford: Wiley-Blackwell; 1998.

[63] Hajnal J V., de Coene B, Lewis PD, Baudouin CJ, Cowan FM, Pennock JM, et al. High Signal Regions in Normal White Matter Shown by Heavily T2-Weighted CSF Nulled IR Sequences. J Comput Assist Tomogr 1992;16:506–13.

[64] Hajnal J V., Bryant DJ, Kasuboski L, Pattany PM, de Coene B, Lewis PD, et al. Use of Fluid Attenuated Inversion Recovery (FLAIR) Pulse Sequences in MRI of the Brain. J Comput Assist Tomogr 1992;16:841–4.

[65] Wang J, He L, Zheng H, Lu ZL. Optimizing the Magnetization-Prepared Rapid Gradient-Echo (MP-RAGE) sequence. PLoS One 2014;9:1–12.

[66] Marques JP, Kober T, Krueger G, van der Zwaag W, Van de Moortele PF, Gruetter R. MP2RAGE, a self bias-field corrected sequence for improved segmentation and T1-mapping at high field. Neuroimage 2010;49:1271–81.

[67] Van de Moortele PF, Auerbach EJ, Olman C, Yacoub E, Uğurbil K, Moeller S. T1 weighted brain images at 7 Tesla unbiased for Proton Density, T2 * contrast and RF coil receive B1 sensitivity with simultaneous vessel visualization. Neuroimage 2009;46:432–46.

[68] Demirkaya O, Asyali MH, Sahoo P. Image processing with MATLAB : applications in medicine and biology. 1st ed. Boca Raton: CRC Press; 2009.

[69] Arnold JB, Liow JS, Schaper KA, Stern JJ, Sled JG, Shattuck DW, et al. Qualitative and quantitative evaluation of six algorithms for correcting intensity nonuniformity effects. Neuroimage 2001;13:931–43.

[70] Uwano I, Kudo K, Yamashita F, Goodwin J, Higuchi S, Ito K, et al. Intensity inhomogeneity correction for magnetic resonance imaging of human brain at 7T. Med Phys 2014;41:2–9.

[71] Hou Z. A Review on MR Image Intensity Inhomogeneity Correction. Int J Biomed Imaging 2006;2006:1–11.

[72] De Graaf WL, Zwanenburg JJM, Visser F, Wattjes MP, Pouwels PJW, Geurts JJG, et al. Lesion detection at seven Tesla in multiple sclerosis using magnetisation prepared 3D-FLAIR and 3D-DIR. Eur Radiol 2012;22:221–31.

[73] Ashburner J, Friston KJ. Unified segmentation. Neuroimage 2005;26:839–51.

[74] Rockmore DN, Healy Jr. DM. Modern Signal Processing. vol. 46. Cambridge: MSRI Publications; 2003.

[75] Ashburner J, Friston K, Penny W. Human Brain Function. 2nd ed. Amsterdam: Elsevier; 2003.

[76] Collignon A, Maes F, Delaere D, Vandermeulen D, Suetens P, Marchal G. Automated Multi-modality Image Registration Based on Information Theory. Inf Process Med Imaging 1995;3:263–74.

[77] Ardekani BA, Guckemus S, Bachman A, Hoptman MJ, Wojtaszek M, Nierenberg J. Quantitative comparison of algorithms for inter-subject registration of 3D volumetric brain MRI scans. J Neurosci Methods 2005;142:67–76.

[78] Ashburner J. A fast diffeomorphic image registration algorithm. Neuroimage 2007;38:95–113.

[79] Jobin Christ MC, Parvathi RMS. A Survey on MRI Brain Segmentation. Adv Intell Soft Comput 2012;166:167–77.

[80] Despotović I, Goossens B, Philips W. MRI Segmentation of the Human Brain: Challenges, Methods, and Applications. Comput Math Methods Med 2015;2015:1–23.

[81] Fischl B, Salat DH, Busa E, Albert M, Dieterich M, Haselgrove C, et al. Whole Brain Segmentation: Automated Labeling of Neuroanatomical Structures in the Human Brain. Neuron 2002;33:341–55.

[82] Fischl B, Sereno MI, Dale AM. Cortical Surface-Based Analysis: II. Inflation, flattening, and a surface-based coordinate system. Neuroimage 1999;9:195–207.

[83] Fischl B, Sereno MI, Tootell RBH, Dale a M. High-resolution inter-subject averaging and a surface-based coordinate system. Hum Brain Mapp 1999;8:272–84.

[84] Dale AM, Fischl B, Sereno MI. Cortical Surface-Based Analysis: I. Segmentation and Surface Reconstruction. Neuroimage 1999;9:179–94.

[85] Rovira À, Wattjes MP, Tintoré M, Tur C, Yousry TA, Sormani MP, et al. MAGNIMS consensus guidelines on the use of MRI in multiple sclerosis - clinical implementation in the diagnostic process. Nat Rev Neurol 2015;11:471–83.

[86] Thompson AJ, Banwell BL, Barkhof F, Carroll WM, Coetzee T, Comi G, et al. Diagnosis of multiple sclerosis : 2017 revisions of the McDonald criteria. Lancet Neurol 2018;17.

[87] Geurts JJG, Blezer ELA, Vrenken H, Van Der Toorn A, Castelijns JA, Polman CH, et al. Does high-field MR imaging improve cortical lesion detection in multiple sclerosis? J Neurol 2008;255:183–91.

[88] Simon B, Schmidt S, Lukas C, Gieseke J, Träber F, Knol DL, et al. Improved in vivo detection of cortical lesions in multiple sclerosis using double inversion recovery MR imaging at 3 Tesla. Eur Radiol 2010;20:1675–83.

[89] Wattjes M, Lutterbey G., Gieseke J, Traber F, Klotz L, Schmidt S, et al. Double Inversion Recovery Brain Imaging at 3T : Diagnostic Value in the Detection of Multiple Sclerosis Lesions. Am J Neuroradiol 2007;28:54–9.

[90] Sethi V, Yousry TA, Muhlert N, Ron M, Golay X, Wheeler-Kingshott C, et al. Improved detection of cortical MS lesions with phase-sensitive inversion recovery MRI. J Neurol Neurosurg Psychiatry 2012;83:877–82.

[91] Nelson F, Poonawalla A, Hou P, Wolinsky JS, Narayana PA. 3D MPRAGE improves classification of cortical lesions in multiple sclerosis. Mult Scler 2008;14:1214–9.

[92] Kollia K, Maderwald S, Putzki N, Schlamann M, Theysohn JM, Kraff O, et al. First clinical study on ultra-high-field MR imaging in patients with multiple sclerosis: Comparison of 1.5T and 7T. Am J Neuroradiol 2009;30:699–702.

[93] De Graaf WL, Kilsdonk ID, Lopez-Soriano A, Zwanenburg JJM, Visser F, Polman CH, et al. Clinical application of multi-contrast 7-T MR imaging in multiple sclerosis: Increased lesion detection compared to 3 T confined to grey matter. Eur Radiol 2013;23:528–40.

[94] Beck ES, Sati P, Sethi V, Kober T, Dewey B, Bhargava P, et al. Improved Visualization of Cortical Lesions in Multiple Sclerosis Using 7T MP2RAGE. Am J Neuroradiol 2018;39:459–66.

[95] Abdel-Fahim R, Mistry N, Mougin O, Blazejewska A, Pitiot A, Retkute R, et al. Improved detection of focal cortical lesions using 7 T magnetisation transfer imaging in patients with multiple sclerosis. Mult Scler Relat Disord 2014;3:258–65.

[96] Kilsdonk ID, De Graaf WL, Soriano AL, Zwanenburg JJ, Visser F, Kuijer JPA, et al. Multicontrast MR Imaging at 7T in Multiple Sclerosis: Highest Lesion Detection in Cortical Gray Matter with 3D-FLAIR. Am J Neuroradiol 2013;34:791–6.

[97] Haider L, Zrzavy T, Hametner S, Hoftberger R, Bagnato F, Grabner G, et al. The topograpy of demyelination and neurodegeneration in the multiple sclerosis brain. Brain 2016;139:807–15.

[98] Treaba CA, Granberg TE, Sormani MP, Herranz E, Ouellette RA, Louapre C, et al. Longitudinal Characterization of Cortical Lesion Development and Evolution in Multiple Sclerosis. Radiology 2019;291:740–9.

[99] Jonkman LE, Klaver R, Fleysher L, Inglese M, Geurts JJG. Ultra-High-Field MRI Visualization of Cortical Multiple Sclerosis Lesions with T2 and T2 *: A Postmortem MRI and Histopathology Study. Am J Neuroradiol 2015;36:2062–7.

[100] Pitt D, Boster A, Pei W, Wohleb E, Jasne A, Zachariah CR, et al. Imaging cortical lesions in multiple sclerosis with ultra-high-field magnetic resonance imaging. Arch Neurol 2010;67:812–8.

[101] Lüsebrink F, Wollrab A, Speck O. Cortical thickness determination of the human brain using high resolution 3T and 7T MRI data. Neuroimage 2013;70:122–31.

[102] Hametner S, Bianco AD, Trattnig S, Lassmann H. Iron related changes in MS lesions and their validity to characterize MS lesion types and dynamics with Ultra-high field magnetic resonance imaging. Brain Pathol 2018;28:743–9.

[103] Seewann A, Vrenken H, Kooi E, Valk P Van Der, Knol DL, Polman CH, et al. Imaging the tip of the iceberg : visualization of cortical lesions in multiple sclerosis. Mult Scler J 2011;17:1202–10.

[104] Ganzetti M, Wenderoth N, Mantini D. Quantitative Evaluation of Intensity Inhomogeneity Correction Methods for Structural MR Brain Images. Neuroinformatics 2016;14:5–21.

[105] Hendrick ER. Brest MRI. 1st ed. New York: Springer; 2008.

[106] Seiger R, Hahn A, Hummer A, Kranz GS, Ganger S, Küblböck M, et al. Voxel-based morphometry at ultra-high fields. A comparison of 7T and 3T MRI data. Neuroimage 2015;113:207–16.

[107] Zaretskaya N, Fischl B, Reuter M, Renvall V, Polimeni JR. Advantages of cortical surface reconstruction using submillimeter 7 Tesla MEMPRAGE. Neuroimage 2018;Jan 15:11–26.

[108] Lüsebrink F, Sciarra A, Mattern H, Yakupov R, Speck O. T1-weighted in vivo human whole brain MRI dataset with an ultrahigh isotropic resolution of 250 μm. Sci Data 2017;4.

[109] Andersen M, Björkman-Burtscher IM, Marsman A, Petersen ET, Boer VO. Improvement in diagnostic quality of structural and angiographic MRI of the brain using motion correction with interleaved, volumetric navigators. PLoS One 2019;14:1–16.

Appendices

Appendix A

In this section, sagittal and coronal sections of a patient and a healthy control displaying the outcome of the first alignment between the subjects' unmasked MPRAGE images and the unmasked MNI template, the fixed image, are presented. The misalignment found for the patient, particularly seen in the coronal section with reference to the vertical axis, was the reason why the alignment was performed between masked images.

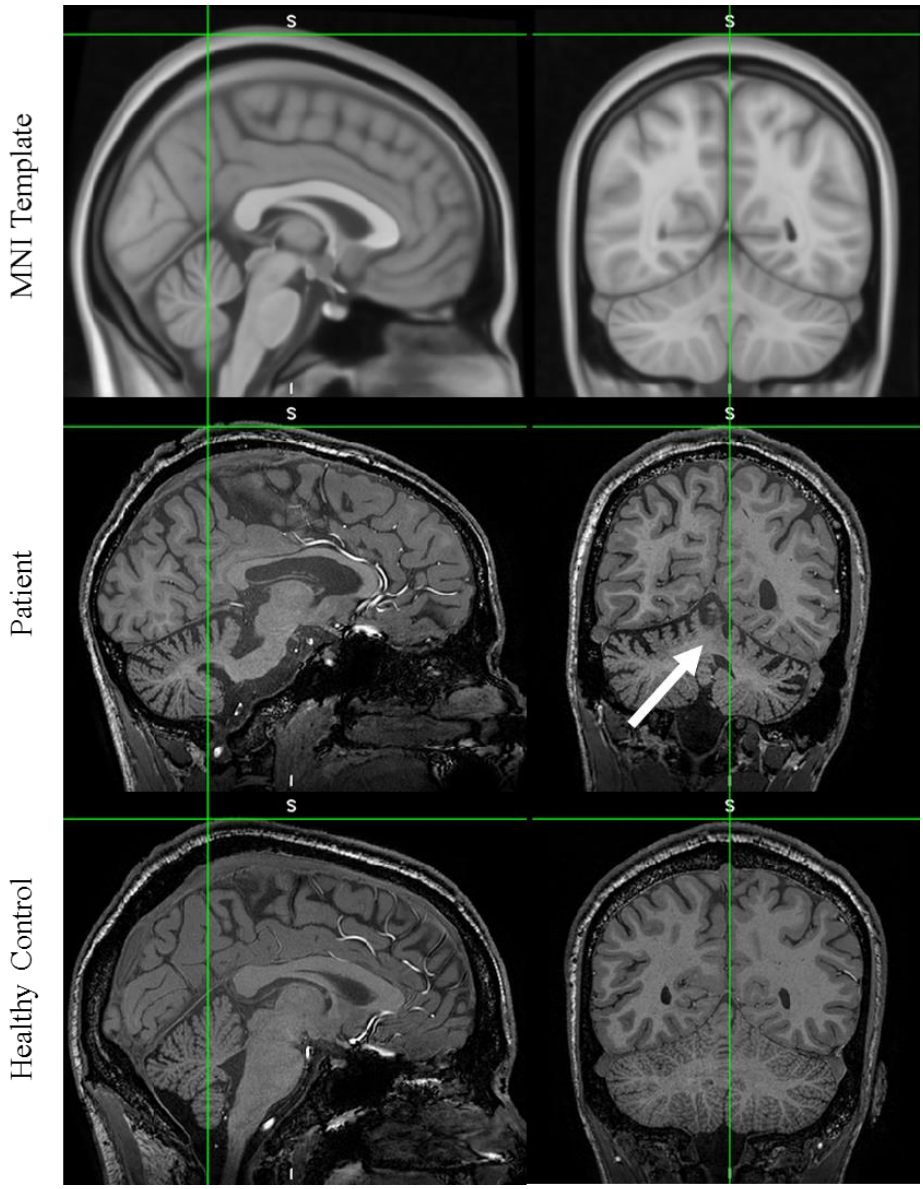

Figure A.1: Sagittal and coronal sections of a patient and a healthy control displaying the poor outcome of the first alignment between the subjects' unmasked MPRAGE images and the unmasked MNI template, the fixed image.

Appendix B

In this section, an excerpt of the coregistration script that calculates the transformation matrix from the masked MPRAGE to the masked MNI space and applies it to the image, performing its coregistration and reslicing it, using specific SPM commands, is given. The remaining alignments in the coregistration procedure follow a similar approach, only differing in the files defined as "RefVol" and "AtlasSpace", namely, the moving and fixed files.

```
AtlasSpace =
['/mnt/projects/CLiMS/7TMRI/CoregAnalysis_Marta/masked_MNI152_T1_0.5mm.ni
i'];
RefVol = dir('masked*MPRAGE.nii');

flags = [];
IMG = [RefVol.folder,'/',RefVol.name];
IMG = [patdir,RefVol.name];

P = spm_coreg(AtlasSpace,IMG);
% calculate rotation matrix from mprage to mni
mni2mpr = spm_matrix(P); % affine transformation matrix from P
V = spm_vol(IMG);
mpr = V.mat;
M = inv(mni2mpr)*mpr;

% save new image in outdir with updated matrix
Iout = spm_read_vols(V);
Vout = V; Vout.mat = M; Vout.fname = fullfile(patdir,RefVol.name);
spm_write_vol(Vout,Iout);

% reslice to highres mni
flags.mean = 0;
flags.which = 1;
spm_reslice({AtlasSpace;Vout.fname},flags);
```

Appendix C

In this section, axial cuts displaying the results from the segmentation using CAT's default parameters are shown. Due to an integrated registration step to the MNI space of 1.5-mm, a warping and downsampling of the MPRAGE image resulted which extended into the segmentation results.

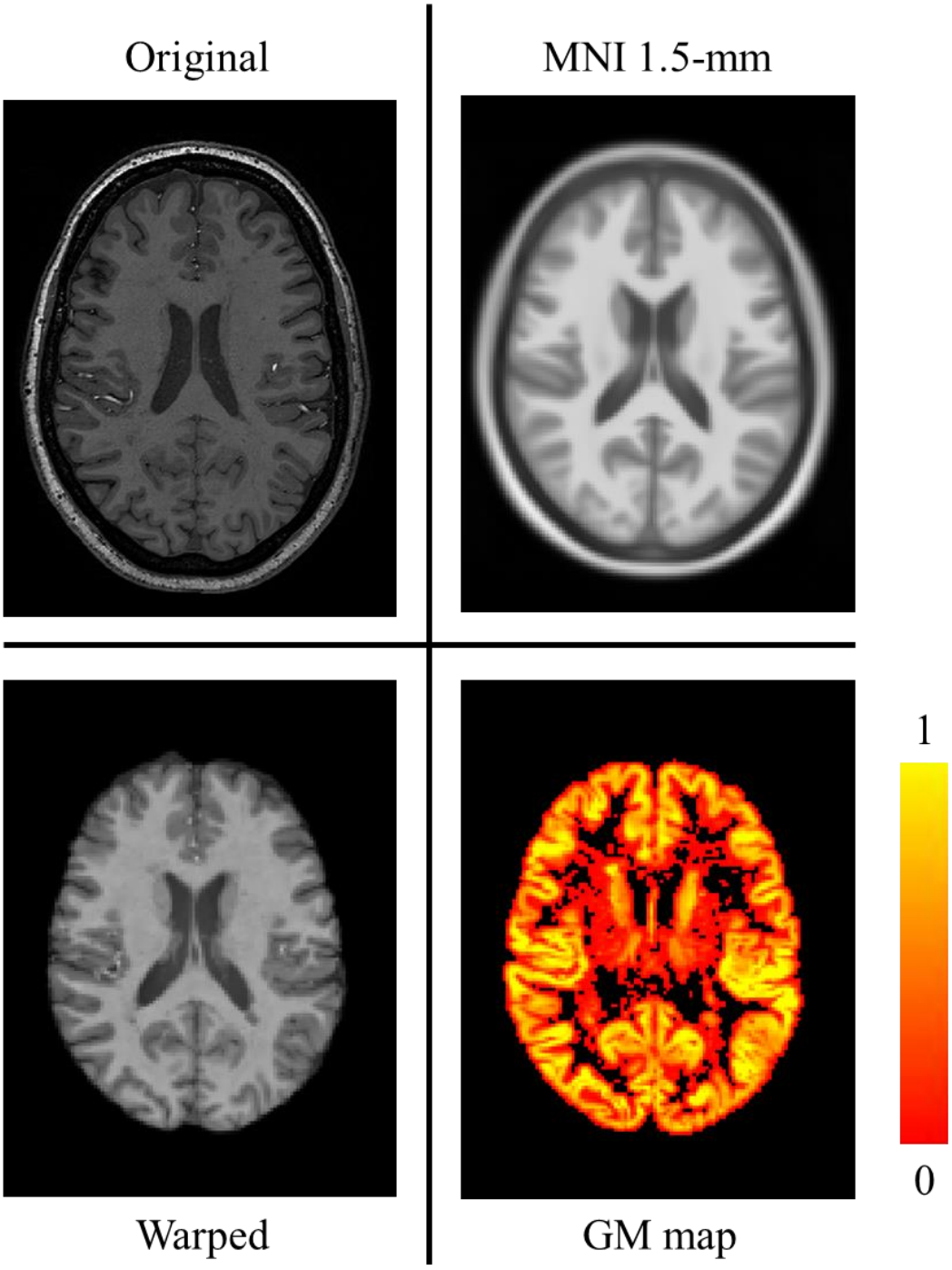

Figure A.2: Outcomes from the segmentation step using CAT's default parameters.

Appendix D

In this section, brain-extracted masks acquired from FSL's BET tool overlaid on the original MPRAGE volume for a participant are given. The most accurate depiction of the brain was obtained for the lowest fractional intensity threshold value.

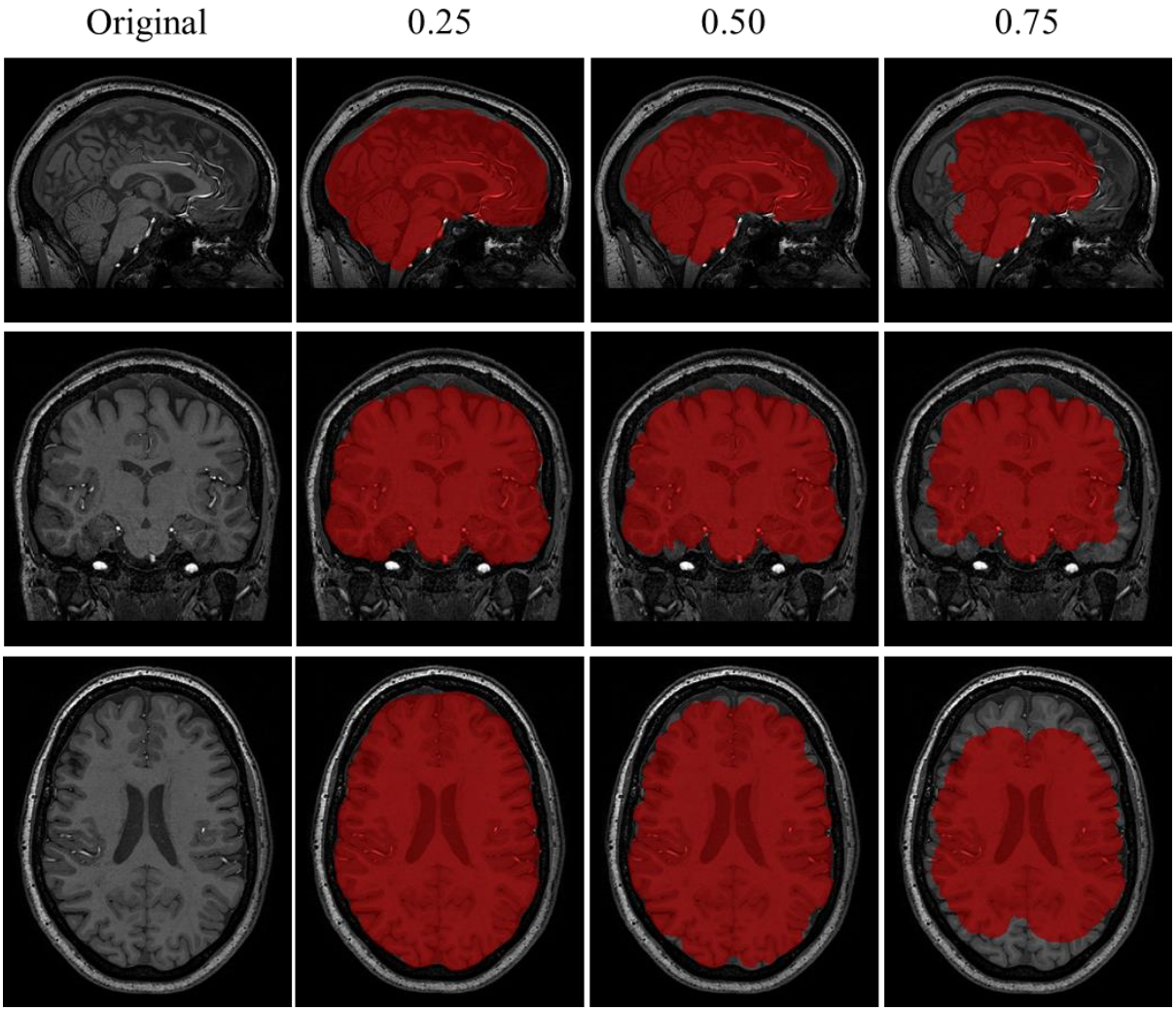

Figure A.3: Brain-extracted masks overlaid on the original MPRAGE volume for a participant using different fractional intensity threshold values.

Appendix E

In this section, an excerpt of the code created in MATLAB for the CNR analysis is provided.

```
gm(gm(:)>0)=1;

% - Connecting Lesions -
[lesion_label,number] = bwlabeln(mask,26);

% - Labelling lesions and excluding "false lesions" based on volume -
j = 0;
vol = [];
lesion_label_temp = lesion_label * 0;

for i = 1:number

    lesion_i = lesion_label==i;
    volume(i) = sum(lesion_i(:));

    if volume(i) > 6

        vol = [vol volume(i)];
        j = j + 1;
        lesion_label_temp = lesion_label_temp + lesion_i * j;

    end

end

% - Parameters of Interest -
lesion_label = lesion_label_temp;
number = j;
volume = vol;

lesion_count = lesion_count + number;
total_lesion_count = total_lesion_count + lesion_count;

CNR_flair = [];
CNR_mprage = [];
CNR_t1w = [];
CNR_t2w = [];

% -- Contrast-to-Noise Calculation --
for i = 1:number

    lesion_i = lesion_label==i;

    % - Defining structural elements of radius 1 and 2 -
    lesion_i = double(lesion_i);
    structure1 = strel('sphere',1);
    dilatedlesion_1 = imdilate(lesion_i,structure1);
```

```
    structure2 = strel('sphere',2);
    dilatedlesion_2 = imdilate(lesion_i,structure2);
    dilatedring_i = dilatedlesion_2 - dilatedlesion_1;

    files = {flair mprage t1w t2w};
    CNR = [];

    for j=1:length(files)

        seq = cell2mat(files(j));
        seq_gm = seq(:,:,:).*gm(:,:,:);

        % - Contrast -
        S_L = mean(seq(lesion_i(:)==1),'omitnan');
        S_N = mean(seq_gm(dilatedring_i(:)==1),'omitnan');
        C = abs(S_L-S_N);

        % - Noise -
        N = std(seq_gm(dilatedring_i(:)==1),'omitnan');

        % - Contrast to Noise Ratio -
        cnr = C/N;
        CNR = [CNR cnr];

    end

    CNR_flair = [CNR_flair CNR(1)];
    CNR_mprage = [CNR_mprage CNR(2)];
    CNR_t1w = [CNR_t1w CNR(3)];
    CNR_t2w = [CNR_t2w CNR(4)];

end
```

Appendix F

This section contains the histograms showing the voxel intensity distribution of WM, GM and CSF for the remaining eight patients and four healthy controls in the dataset for the original and bias corrected volumes using SPM's default and enhanced parameters.

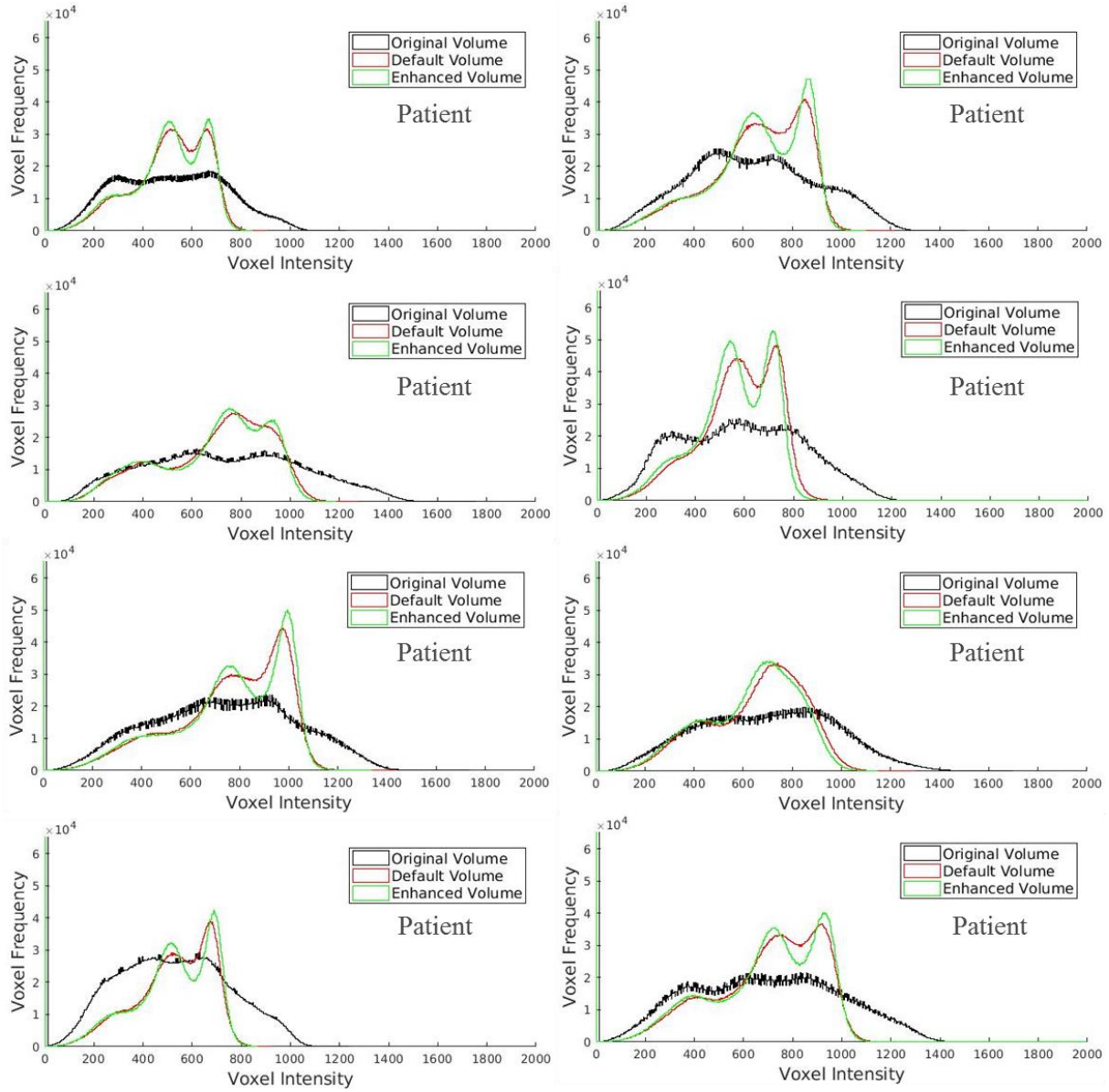

Figure A.4: Histograms showing the voxel intensity distribution of WM, GM and CSF for eight patients in the dataset.

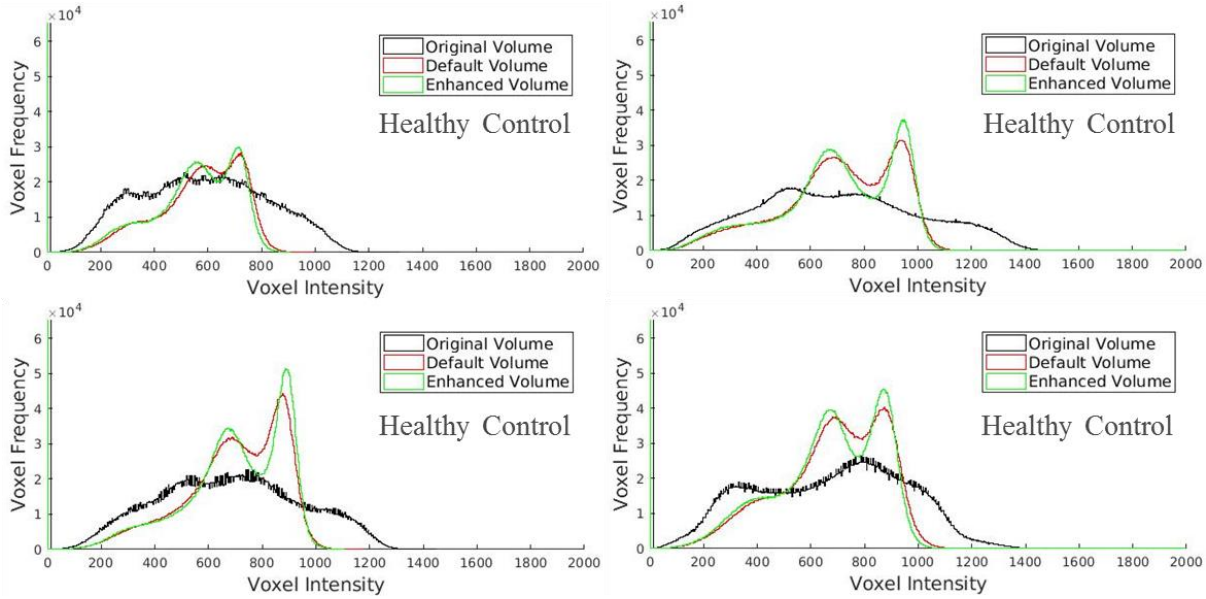

Figure A.5: Histograms showing the voxel intensity distribution of WM, GM and CSF for four healthy controls in the dataset.

Appendix G

In this section, axial cuts of the WM probability maps acquired from the three tested segmentation approaches are shown. The predominance of voxels with low tissue probability in GM in the SPM image suggests a poorer segmentation performance using this approach.

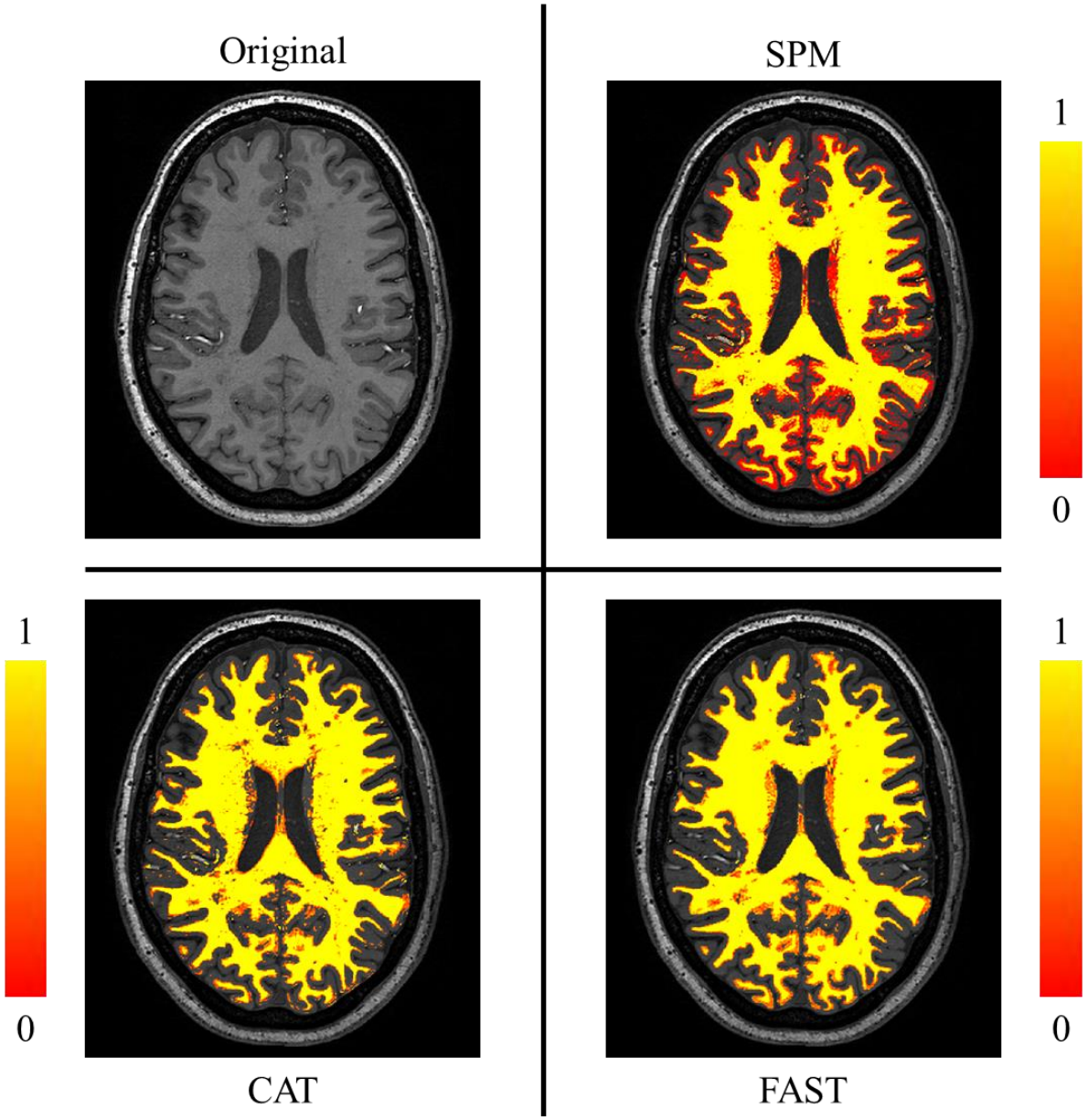

Figure A.6: Axial cuts of the WM probability maps acquired from the three tested segmentation approaches.

Appendix H

In this section, the inflated brain surfaces acquired in FreeSurfer for the twelve dataset patients with the respective manually segmented cortical lesions overlaid are displayed.

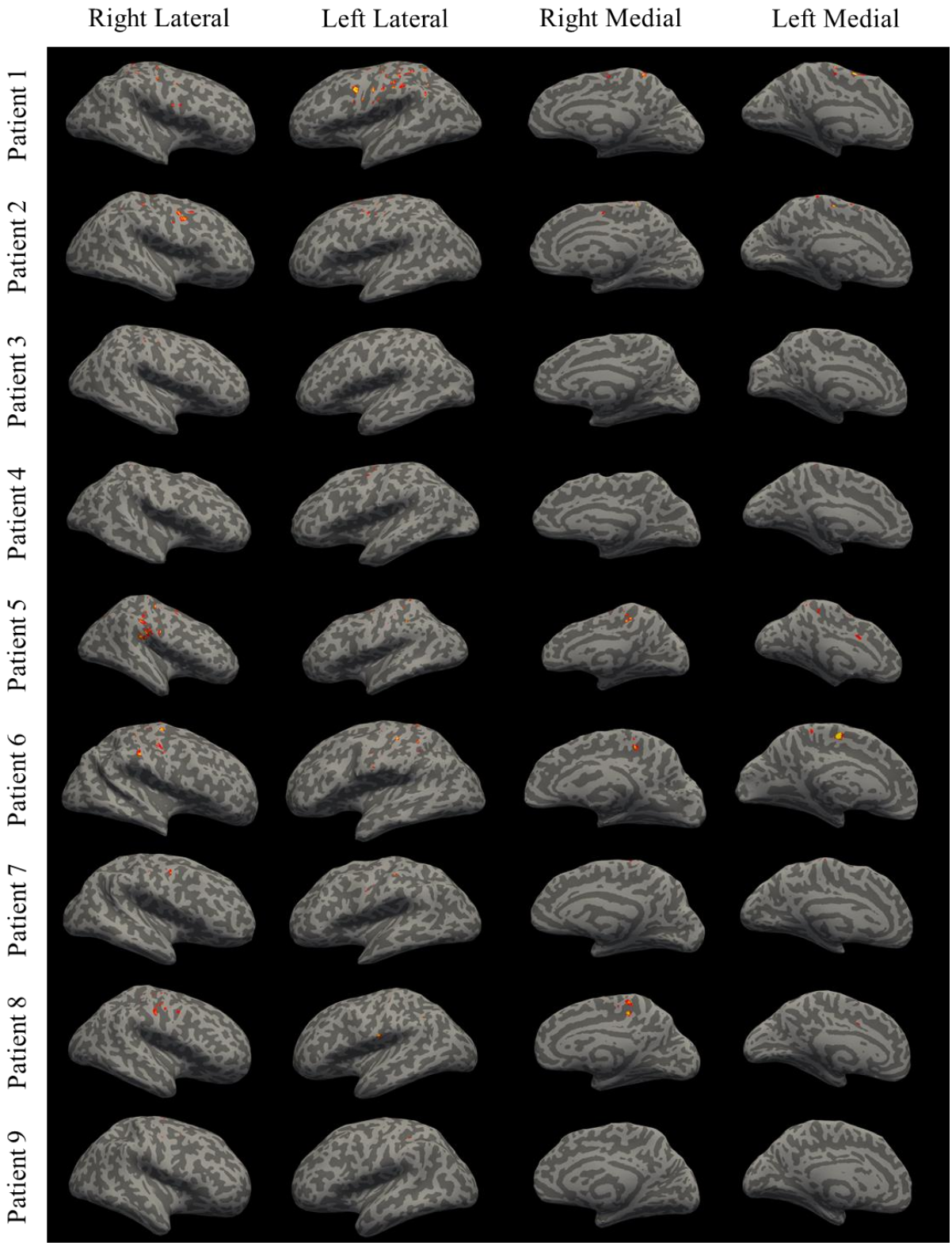

Figure A.7: Inflated brain surfaces for nine patients with their respective segmented cortical lesions overlaid.

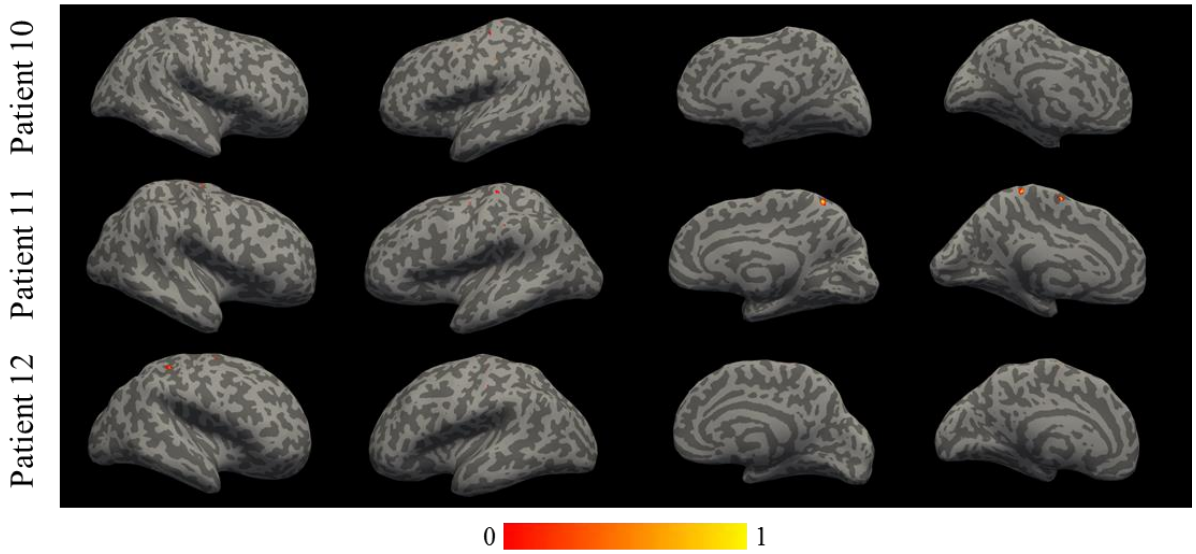

Figure A.8: Inflated brain surfaces for three patients with their respective segmented cortical lesions overlaid.

Appendix I

The work carried out during this dissertation contributed to the development of two abstracts. The details of the outcomes of this project are described below.

1. **Annual Meeting for the Danish Multiple Sclerosis Society, 2019, Copenhagen, Denmark**
   Title: 'Hvad er betydningen af en kortikal laesion for patienter med multipel sklerose? – et 7T studie'
   Authors: Madsen, M. A. J.[1], **Marques, M. F. M.[2]**, Lundell, H.[1], Sellebjerg, F.[3], Leffers, AM.[1], Madsen, C. G., [1]Andersen, K. W.[1], Karabanov, A. N.[1], Blinkenberg, M., Siebner, H. R.[1,4]
   [1]Danish Research Centre for Magnetic Resonance, Copenhagen University Hospital Hvidovre, Copenhagen, Denmark; [2]Faculty of Sciences, University of Lisbon, Lisbon, Portugal; [3]Danish Multiple Sclerosis Center, Rigshospitalet, University of Copenhagen, Copenhagen, Denmark; [4]Department of Neurology, Copenhagen University Hospital Bispebjerg, Copenhagen, Denmark;
   Presentation: Presented by PhD Student Mads Madsen in March 2019.

2. **35th Congress of the European Committee for Treatment and Research in Multiple Sclerosis, 2019, Stockholm, Sweden**
   Title: 'Effects of a single cortical lesion on functional activation in the primary somatosensory cortex – a case study'
   Authors: Madsen, M. A. J.[1], **Marques, M. F. M.[2],** Andersen, K. W.[1], Lundell, H.[1], Sellebjerg, F.[3], Blinkenberg, M.[3], Romme Christensen, J.[3], Siebner, H. R.[1,4,5]
   [1]Danish Research Centre for Magnetic Resonance, Copenhagen University Hospital Hvidovre, Copenhagen, Denmark; [2]Faculty of Sciences, University of Lisbon, Lisbon, Portugal; [3]Danish Multiple Sclerosis Center, Rigshospitalet, University of Copenhagen, Copenhagen, Denmark; [4]Department of Neurology, Copenhagen University Hospital Bispebjerg, Copenhagen, Denmark; [5]Institute for Clinical Medicine, Faculty of Medical and Health Sciences, University of Copenhagen, Copenhagen, Denmark.
   Presentation: Accepted for a digital-poster presentation to be presented by PhD Student Mads Madsen in September 2019.